

ATOMISTIC SIMULATIONS OF DEFECT STRUCTURES IN SOLID
OXIDE FUEL CELL ELECTROLYTES

BY

BU WANG

A THESIS

SUBMITTED TO THE FACULTY OF

ALFRED UNIVERSITY

IN PARTIAL FULFILLMENT OF THE REQUIREMENTS
FOR THE DEGREE OF

DOCTOR OF PHILOSOPHY

IN

CERAMICS

ALFRED, NEW YORK

FEBRUARY, 2012

Alfred University theses are copyright protected and may be used for education or personal research only. Reproduction or distribution in any format is prohibited without written permission from the author.

ATOMISTIC SIMULATIONS OF DEFECT STRUCTURES IN SOLID
OXIDE FUEL CELL ELECTROLYTES

BY
BU WANG
B.S. TIANJIN UNIVERSITY, CHINA (2004)
M.S. TIANJIN UNIVERSITY, CHINA (2007)

SIGNATURE OF AUTHOR _____ (Signature on File)

APPROVED BY _____ (Signature on File)
ALASTAIR N. CORMACK, ADVISOR

(Signature on File)
DOREEN D. EDWARDS, ADVISORY COMMITTEE

(Signature on File)
WALTER A. SCHULZE, ADVISORY COMMITTEE

(Signature on File)
OLIVIA A. GRAEVE, ADVISORY COMMITTEE

(Signature on File)
YIQUAN WU, ADVISORY COMMITTEE

(Signature on File)
CHAIR, ORAL THESIS DEFENSE

ACCEPTED BY _____ (Signature on File)
DOREEN D. EDWARDS, DEAN
KAZUO INAMORI SCHOOL OF ENGINEERING

ACCEPTED BY _____ (Signature on File)
NANCY J. EVANGELISTA, ASSOCIATE PROVOST
FOR GRADUATE AND PROFESSIONAL PROGRAMS
ALFRED UNIVERSITY

ACKNOWLEDGMENTS

I have heard, on various occasions, people complaining about how difficult the Ph.D. life is. I am grateful that I never felt that way. Head-banging against the keyboard is a necessary process in computer simulations, but I never had to do it just to get myself moving. This has to be attributed to my advisor, Dr. Alastair N. Cormack, for his encouraging style of coaching graduate students, and the small but tight community at Alfred.

In regard to the content of this thesis, I need to thank Dr. Cormack for his insightfulness and meticulousness. I would like to thank my thesis committee for their valuable suggestions and support; Raymond Lewis, Robert Koch, Dr. Jian Liu, Jiawanjun Shi for countless discussions; NYSTAR and CNNI at RPI for their supercomputing power which made possible the large scale calculations in this thesis.

I would like to express my gratitude to Dr. Edwards and Dr. Graeve for helping me schedule my defense. Good luck to Mark Naylor, who is going to defend two days after me. And best wishes to all those I have worked closely and shared this important period of my life with: Dr. William Carlson, Dr. Jinghong Fan, Dr. Laura Adkins, Sam Lamphier, Bo Jiang, Chi Qu, Ryan Musson, Dr. Tongan Jin ...

Finally, I thank my family for their support behind every step of my life. My dear wife -- I know you will be by my side no matter what. It is not enough just to say thank you; love you, always.

TABLE OF CONTENTS

	Page
Acknowledgments	iii
Table of Contents	iv
List of Tables	vi
List of Figures	vii
Abstract	ix
CHAPTER 1. INTRODUCTION	1
A. Electrolytes for intermediate temperature SOFC.....	2
B. Defect associations and nano-domains in GDC and SDZ	3
1. Defect association in GDC	4
2. Defect association in SDZ	5
C. Phase systems of gadolinia-ceria and scandia-zirconia	6
1. Gadolinia-ceria	6
2. Scandia-zirconia	7
D. Overview	11
References	11
CHAPTER 2. METHOD	17
A. Classical simulation techniques	17
1. Short-ranged potentials	18
2. Structure optimization	18
3. Molecular dynamics.....	20
B. Ab-initio simulation with density functional theory.....	21
1. Exchange-correlation functional.....	22
2. Pseudopotential.....	22
3. Basis set.....	23
References	23
CHAPTER 3. DEFECT STRUCTURES IN GDC	26
A. Basic defect association.....	26
B. Small clusters.....	28
C. Conclusions	30
References	31

CHAPTER 4. NANO-DOMAINS IN GDC.....	33
A. B-type rare earth structure	34
1. Method to simulate large B-type defect clusters.....	34
2. Relationship between the B-type and fluorite structures	37
3. Defect calculations.....	38
B. C-type rare earth structure and pyrochlore structure	40
C. Nano-domains and phase separation	43
D. Domain size	45
E. Conclusions	54
References	55
CHAPTER 5. STRAIN MODULATION OF DEFECT STRUCTURE IN GDC..	58
A. Strain effect on basic defect pairs.....	59
B. Strain modulation of the defect structure in GDC	62
C. Conclusions	68
References	69
CHAPTER 6. STRUCTURES IN SCANDIA-ZIRCONIA PHASE SYSTEM..	70
A. Structures of zirconia and scandia	71
B. δ phase $\text{Sc}_4\text{Zr}_3\text{O}_{12}$	72
C. γ phase ($\text{Sc}_2\text{Zr}_5\text{O}_{13}$).....	78
D. β phase $\text{Sc}_{12}\text{Zr}_{50}\text{O}_{118}$	84
E. Conclusions	87
References	88

LIST OF TABLES

	Page
Table I. Short-Range Potential Parameters for GDC	18
Table II. Shell Model Parameters for GDC	18
Table III. Percentage of $V_o^{\cdot\cdot}$ with No Gd^{3+} Neighbor and Lattice Parameters of the Samples at Different Stages of the Simulation	64
Table IV. Simulated Structures, as well as the Cohesive Energies, of Zirconia and Scandia, Compared with the Experimental Data	71
Table V. Short-Range Potential Parameters for SDZ	76
Table VI. Shell Model Parameters For SDZ	76

LIST OF FIGURES

	Page
Figure 1. (a) B-type Gd_2O_3 ; (b) C-type Gd_2O_3 ; (c) Fluorite CeO_2	7
Figure 2. Schematic scandia-zirconia phase diagram derived from reference 49, showing the composition range of the three rhombohedral phases.	8
Figure 3. Structures of (a) cubic zirconia, (b) tetragonal zirconia, (c) monoclinic zirconia, and (d) C-type scandia.	8
Figure 4. Structures of (a) β , (b) γ , and (c) δ phases.	10
Figure 5. (a) The structure of fluorite CeO_2 . Lattice distortions around an oxygen vacancy, showing (b) lattice contraction around the vacancy.	27
Figure 6. Stable charge neutral defect clusters containing increasing number of oxygen vacancies from 1 to 5 with binding energies shown below..	29
Figure 7. Flow chart of the simulation method.....	35
Figure 8. (a) B-type Gd_2O_3 viewed from [010]; (b) Fluorite CeO_2 viewed from [110]; (c) B-type Gd_2O_3 fragment which corresponds to the fluorite.....	36
Figure 9. Single plane of a 4 unit cell defect cluster after relaxation, viewed from [001] direction.....	40
Figure 10. (a) C-type Gd_2O_3 structure (b) C-type Gd_2O_3 structure viewed as a defect fluorite structure.....	41
Figure 11. (a) pyrochlore $Gd_2Ce_2O_7$ structure (b) pyrochlore $Gd_2Ce_2O_7$ viewed as a defect fluorite structure.	41
Figure 12. The most stable defect cluster among (a) one pyrochlore unit cell clusters (b) half C-type unit cell clusters.....	42
Figure 13. Illustration of the method of building supercells with a nano-domain structure.....	46

Figure 14.	Binding energy per oxygen vacancy versus domain size obtained from the simulations of defect supercells.....	47
Figure 15.	Illustration of the highly distorted regions in a relaxed defected supercell...	49
Figure 16.	Defect energies of NN, NNN, and 3NN type $Gd'_{Ce}-V_O^{\bullet\bullet}$ pairs, as well as isolated defects, versus lattice strains..	60
Figure 17.	Configurational energies during the initial NPT equilibration of sample 1. Other samples behaved in the same way..	63
Figure 18.	Arrhenius plot of the relaxation time constant versus inverse temperature. .	67
Figure 19.	The primitive cell of the δ phase. Cations are shown in green, oxygen in red and vacancies as beach balls.....	72
Figure 20.	The most stable cation ordering in the δ phase primitive cell, calculated with the SIESTA code..	74
Figure 21.	Energies of the 7 δ phase configurations calculated with the classical approach compared with the DFT approach.....	77
Figure 22.	The primitive cell of the γ phase. Cations are shown in green, oxygen in red and vacancies as beach balls.....	79
Figure 23.	The most stable cation ordering in the γ phase primitive cell, calculated with the SIESTA code..	81
Figure 24.	Energies of the 41 γ phase configurations calculated with the classical approach compared with the DFT approach.....	83
Figure 25.	The primitive cell of the β phase is shown in (a), and the characteristic vacancy arrangement is shown in (b).....	84
Figure 26.	Energies of the 45 β phase configurations calculated with the classical approach compared with the DFT approach.....	85
Figure 27.	Characteristic dopant-vacancy pattern of the most stable configurations.	86

ABSTRACT

The defect structures in two promising intermediate temperature solid oxide fuel cell electrolytes, gadolinia-doped ceria (GDC) and scandia-doped zirconia (SDZ), were studied by atomistic computer simulations.

In GDC, it was found that sub nano-scale defect clusters preferred a next-nearest-neighbor, pyrochlore-type structure, and that they had a tendency to grow into larger clusters. For nano-scaled domains, however, the C-type rare earth structure, in which the dopants and vacancies are at nearest-neighbor sites, became more stable. It was suggested that nano-domains served as the precursor of phase separation and they could be easily formed during synthesis. Doping concentration limited the size of the nano-domains, and caused GDC to favor small pyrochlore-type clusters at lower concentrations, but C-type nano-domains at higher concentrations. As such, GDC was expected to show initially an increase in conductivity and then a decrease with increasing doping concentration. The lattice parameter of GDC should show the same trend and could be used as an indicator of the predominant defect structure. The cation mobility was another important factor limiting the size of defect clusters, and could be used to control the domain formations and thereby improve the electrolyte performance. It was also found that the defect structure in GDC could be modulated by strain through oxygen diffusing into or out of the nearest neighbor sites of dopants with an activation energy estimated to be 0.82 eV. Based on such a mechanism, an explanation of the “chemical strain/stress” phenomenon observed in gadolinia-doped ceria, as well as the benefit of zero or moderate tensile strain for electrolyte applications, was proposed.

The phase system of SDZ, especially the cation ordering in the three rhombohedral phases, was studied with both classical empirical potentials and ab-initio methods utilizing the density functional theory. Characteristics of defect structures in SDZ at different concentrations were identified based on the structures in the phase system. The abilities of the two methods in simulating the structures and phase stability of the SDZ system were compared and evaluated.

CHAPTER 1. INTRODUCTION

Solid oxide fuel cell (SOFC) is a class of fuel cells that uses solid oxides as its main components. SOFC have distinct advantages over the conventional combustion power generation, and other types of fuel cells. It has exceptionally high electrical generation efficiencies ranging from 45~60%, which can reach as high as 85% when combined with exhaust heat utilization.¹ SOFC can be used with a large variety of conventional and renewable fuels.¹ They do not require expensive platinum catalysts nor do they suffer from carbon monoxide poisoning.¹ For these reasons, both the government and industry have spent substantial effort to accelerate the commercialization of SOFC. Solid-State Energy Conversion Alliance (SECA), an alliance of industry, scientific community and government, was formed with a goal to reduce the mass production cost to \$175/kW for the fuel cell module in 2010, a 8-fold improvement compared to the cost in 2000.² In 2009, SECA successfully exceeded Department of Energy's goals on SOFC's efficiency, cost, and durability. Prototypes have been developed and tested for applications such as stationary power generation and auxiliary power units in heavy-duty vehicles.² At the same time, commercial SOFC systems were also being manufactured and deployed. For instance, Bloom Energy has installed two hundred 100~500 kWh SOFC units since 2008 for major enterprises including Bank of America, Coca-Cola Company, eBay, FedEx Corp and Walmart.³

As the fuel cell technology is being developed and commercialized at an accelerating pace, the high working temperature of SOFC (typically between 700-1000°C) is becoming a major challenge for reducing costs and improving durability. At this temperature range, traditional stainless steel cannot be used as the interconnect material because of cathode poisoning by the volatile chromium in the steel.⁴ The high temperature causes a long start-up time and greatly complicates the design of supporting components such as heat exchangers and cell sealing.⁴ Lowering the working temperature below 700°C can avoid these problems, reduce the cost, and even more significantly, bring SOFC to mobile and personal uses.⁵

One major reason for the high working temperature of SOFC is for the electrolyte material to maintain required oxygen ion conductivity. Since all the SOFC electrolytes achieve high conductivities with the help of defects in the structure, e.g., dopants, oxygen vacancies, understanding the interaction between these defects becomes the key to improve conductivity, lower the SOFC operating temperature and enhance its durability. Moreover, understanding the defect structures in these materials also bears far-reaching significances in understanding the thermodynamics and kinetics of the electrolytes, which can be utilized in improving and designing similar materials.

The above facts prompted us to investigate the defect structures of two of the most promising candidates for the intermediate temperature SOFC (IT-SOFC) electrolyte, gadolinia doped ceria and scandia doped zirconia. Especially, the defect association and nano-scale defect domain formation in these two materials were studied with computer simulations. These simulations were expected to provide critical understandings of the materials that are otherwise difficult to obtain experimentally. Means of limiting defect clustering during electrolyte processing and operation were proposed based on the information obtained.

In the following sections, an overview of the IT-SOFC electrolytes, a literature review of the defect interactions in the two electrolytes, and the background of the gadolinia-ceria and scandia-zirconia phase systems are introduced.

A. Electrolytes for IT-SOFC

Most electrolyte candidates for IT-SOFC are oxygen conductors. Some proton conducting ceramics have also been brought to attentions, such as BaCeO_3 ,⁶ but are beyond the scope of this thesis. Oxygen conducting electrolytes typically have structures related to fluorite, such as stabilized zirconia, doped ceria, stabilized $\delta\text{-Bi}_2\text{O}_3$ and pyrochlores, or perovskite, such as LSGM (**L**anthanum **S**trontium **G**allate **M**agnesite), or both, such as Aurivillius phase BIMEVOX (**B**ismuth **M**etal **V**anadium **O**xide) which consist of alternating layers of fluorite-like $(\text{Bi}_2\text{O}_2)^{2+}$ and perovskite-like $(\text{VO}_{3.5})^{2-}$.⁷

Steele proposed that, for the thickness that allowed for economical mass-production (> 15 microns), an electrolyte of SOFC should achieve at least a conductivity of 10^{-2} S/cm.⁸ $\delta\text{-Bi}_2\text{O}_3$, LSGM, BIMEVOX all meet this requirement, but technical

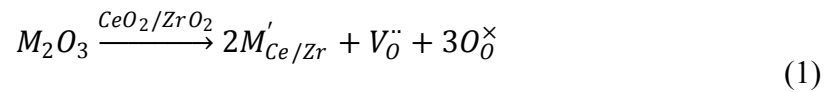
difficulties must be overcome before they can be implemented into the SOFC system. δ - Bi_2O_3 has exceptional ion conductivity, but it is only stable in a narrow temperature range between 730~804 °C.⁹ LSGM is expensive and incompatible with conventional NiO anode.^{10,11} For BIMEVOX, its high-chemical reactivity, low-mechanical strength, and high thermal expansion coefficient must be dealt with.⁷

For zirconia and ceria based electrolytes, high conductivities can be achieved by selecting proper dopants. Sc^{3+} and Gd^{3+} dopants have yielded the highest conductivity in the zirconia and ceria systems, respectively.¹² Scandia doped zirconia (SDZ) and gadolinia doped ceria (GDC) can all exceed 10^{-2} S/cm at temperatures as low as 500 °C.¹² The drawbacks, however, include the cost of scandium,¹⁰ the significant aging effect of SDZ,¹³ and the electronic conduction in the reducing environment of doped ceria.¹⁴

Currently, the most commercialized electrolyte is yttria-stabilized zirconia (YSZ), which offers chemical stability as well as low cost.^{12,15} However, in order to meet Steele's requirement, the operating temperature needs to be above 700 °C.¹² As the working temperature of SOFC is being pushed down to the intermediate range, YSZ is becoming less competitive. At the same time, systems with electrode-supported designs are being adopted to reduce the thickness of the electrolyte,¹⁶ which can mitigate the high cost of scandium. Also, it was found that, at the low end of the intermediate temperature range, the electronic leakage of GDC became less severe.¹⁴ Because of these reasons, SDZ and GDC have attracted extensive attentions as promising candidates for the IT-SOFC electrolyte, and therefore became the focus of this thesis.

B. Defect associations and nano-domains in GDC and SDZ

The exceptional conductivities of various ceramic electrolytes are essentially all achieved with the help of intrinsic or extrinsic oxygen vacancies. In the case of doped ceria and zirconia, the vacancies are created by the following mechanism:



Since an oxygen vacancy is created with the introduction of every two trivalent dopants, the oxygen ion conductivity is expected to increase monotonically with increased doping

prior to the precipitation of a secondary phase. However, experiments showed that the conductivity reached a maximum at a dopant concentration between 10~15 at. % for GDC^{17,18} and 7~9 at. % for SDZ^{19,20}, and then began to decrease. This was much lower than the solubility limit of gadolinia in ceria²¹ and the scandium concentration in the rhombohedral β , γ , δ phase in SDZ¹⁹, respectively. Additionally, the aging effect, where the conductivity degrades significantly during annealing at high temperature, has been reported, especially in SDZ.¹³ It is believed that the dopant-vacancy association is the cause of these phenomena.

1. Defect associations in GDC

Previous simulations, as well as experimental studies using X-ray Absorption Fine Structure (XAFS), have suggested associations between Gd^{3+} and $V_O^{\cdot\cdot}$ in GDC.^{17,22-25} The simulation of $Gd^{3+}-V_O^{\cdot\cdot}-Gd^{3+}$ trimer suggested that it was more energetically favorable than isolated defects, and that its formation would increase the activation energy of the $V_O^{\cdot\cdot}$ charge carriers, thus lower the electrolyte conductivity.²² The associations were suggested to have a next-nearest-neighbor (NNN) configuration.²² However, the experimental study using XAFS spectrometry to determine the dopant-oxygen inter-ion distance suggested that nearest-neighbor (NN) configurations were dominant at high doping concentrations.²⁴ This could indicate a change in the association behavior at high concentrations. There have also been experiments showing an initial increase followed by a decrease in the lattice parameter for GDC with increased doping.^{21,26,27} It is believed this observation is also closely related to the defect association behavior.

High Resolution Transmission Electron Microscopy (HRTEM) detected the formation of nano-domains,²⁸⁻³⁰ and thus provided direct evidence of large scale defect association at high doping concentrations. These nano-domains were found to have a high concentration of Gd^{3+} dopant, which would be necessarily accompanied by a high concentration of oxygen vacancies in order to maintain local charge neutrality. At a nano-scaled size, the domains should have well-developed structures. Recent Selected Area Electron Diffraction (SAED) studies determined the nano-domains to be pyrochlore or C-type structures.^{29,30} However, it was difficult to draw conclusions from such experimental studies owing to the small size of the domains. Moreover, the cause of the observed

formations has not been thoroughly studied. A detailed study of the structure and thermodynamics of nano-domains would be beneficial towards understanding the defect clustering and related experimental observations in GDC. It is expected that it will also promote an understanding of other phenomena in GDC such as the large variation of lattice parameters reported in the literature.^{21,26,31} Furthermore, stable defect clusters, especially nano-domains, would seriously impact the electrolyte conductivity because they trap the oxygen vacancy charge carriers, and therefore study of their formation and structures could substantially aid in improving electrolyte performance.

2. Defect associations in SDZ

Defect associations in SDZ have also been extensively studied. Nuclear magnetic resonance studies of SDZ indicated that a majority of oxygen vacancies were associated with Sc^{3+} dopants in nearest neighbor configurations.^{32,33} Simulation works also supported the nearest neighbor configuration, although it was found that the energy differences between the nearest neighbor, the next nearest neighbor, and the third nearest neighbor configurations were small.³⁴ Molecular dynamics simulations using the same set of interatomic potentials found that the conductivity peaked at 6% doping concentration for SDZ.³⁵ This was explained by the combined effect of the simultaneous increases in the charge carrier population and the activation energy as the doping concentration increases.³⁵

Above studies provided important information about SDZ, but they have not yet delivered a complete understanding of the defect associations in the material. Especially, the ageing effect, a major obstacle for the electrolyte applications, has not been addressed. The effect is characterized by the conductivity degradation at the operation temperature of the electrolyte.³⁶⁻³⁸ Haering et al. proposed that the degradation was caused by the formation of tripoles ($\text{Sc}^{3+}-\text{V}_{\text{O}}^{\cdot\cdot}-\text{Sc}^{3+}$). More complex but popular mechanisms involve phase transformation and participation. Earlier studies suggested that the formation of β phase during annealing was the cause of the aging.³⁹ Badwal and Drennan, however, attributed the degradation to the participation of the tetragonal phase and the formation of domains with rhombohedral γ and δ structures.²⁰ Araki et al. proposed another mechanism blaming the formation of metastable tetragonal phases.⁴⁰ But at the same time, their experiments showed that the annealing effect was much more

evident in the SDZ samples initially containing the tetragonal phases than that containing the rhombohedral phases, indicating a higher stability of the rhombohedral structures in SDZ. These discrepancies show a lack of comprehensive understanding of the defect associations in SDZ and the difficulties in obtaining it experimentally. Considering such, a systematic simulation study on the subject is needed.

However, there has been a lack of computer simulations of large scale defect associations in SDZ. Two difficulties have hindered such studies. First, due to the complexity of the scandia-zirconia phase system, no classical empirical potential model has been able to reproduce all the phases in the system. This leads to some doubts in the validity of using classical simulation techniques for SDZ. Studies have been done with ab-initio methods, but were limited to small defect clusters due to the demand for substantial computational resources.^{41,42} Second, the structures of the three rhombohedral phases, especially their cation ordering, are still not clear. Thus, this thesis focused on these two problems in the chapter of SDZ.

C. Phase systems of gadolinia-ceria and scandia-zirconia

As discussed later with the simulation results, the defect structures and nano-domains were found to be closely related to the structures in the phase system. Additionally, in order to simulate and compare different defect structures, the energetic ordering of these phases must be reproduced first by the simulation models. As such, it is necessary to introduce the phase systems of gadolinia-ceria and scandia-zirconia.

1. Gadolinia-ceria

The $\text{Gd}_2\text{O}_3\text{-CeO}_2$ phase system includes B-type and C-type gadolinia, fluorite ceria, and possibly pyrochlore $\text{Gd}_2\text{Ce}_2\text{O}_7$.^{27,43}

Gadolinia can have monoclinic (B-type) or cubic (C-type) rare earth structure,⁴⁴⁻⁴⁶ as illustrated in Figure 1 (a) and (b). The two structures are all related to fluorite (Figure 1 (c)), and the relationships are discussed later in this thesis.

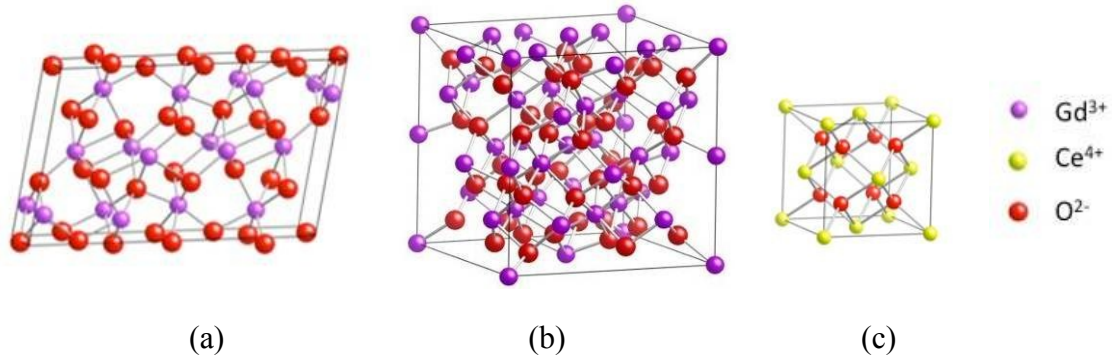


Figure 1. (a) B-type Gd_2O_3 ; (b) C-type Gd_2O_3 ; (c) Fluorite CeO_2 .

Pyrochlore structure is cubic and also closely related to fluorite. Grimes calculated the formation energy of $Gd_2Ce_2O_7$ to be small, yet negative, indicating that it exists in the gadolinia-ceria phase system.²² However, $Gd_2Ce_2O_7$ was absent in the experimental studies of the phase system.^{45,47} The phase stability of the pyrochlore $Gd_2Ce_2O_7$ were re-examined in this thesis.

2. Scandia-zirconia

As indicated in the phase diagram in Figure 2, the Sc_2O_3 - ZrO_2 phase system includes cubic, tetragonal, monoclinic zirconia, C-type scandia (as shown in Figure 3) and three phases in between, namely, β ($Sc_{12}Zr_{50}O_{118}$), γ ($Sc_2Zr_5O_{13}$), δ ($Sc_4Zr_3O_{12}$) phases (as shown in Figure 2).¹⁹ Scandia also exists in hexagonal A-type and monoclinic B-type phases but only under high pressure,⁴⁸ therefore only the cubic C-type phase was studied in this work.

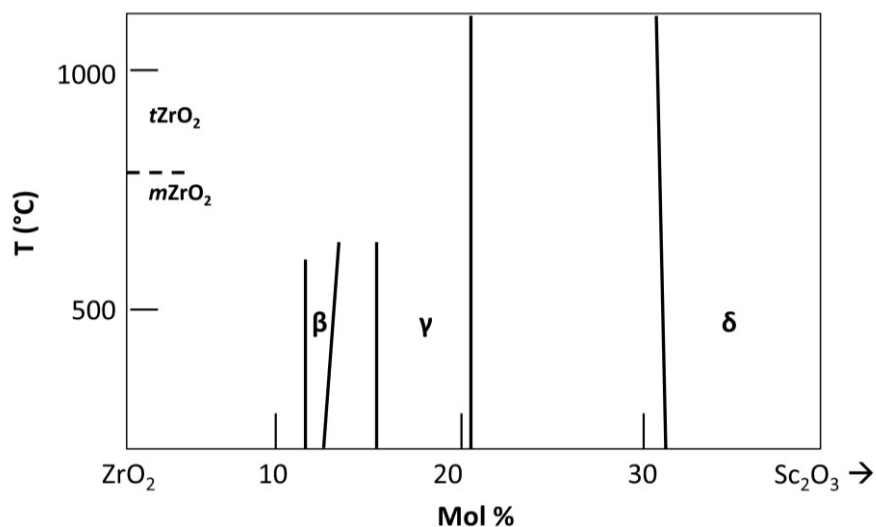


Figure 2. Schematic scandia-zirconia phase diagram derived from reference 49, showing the composition range of the three rhombohedral phases.

The three phases of zirconia have been extensively investigated. For pure zirconia, the monoclinic (space group $P2_1/c$) to tetragonal ($P4_2/nmc$) phase transformation happens around 1400K,⁵⁰ and the tetragonal to cubic ($Fm3m$) around 2600K.⁵¹ Dopants with lower valences, such as Yb^{3+} and Sc^{3+} , can stabilize the high temperature cubic phase at low temperature. For instance, 9~14% Sc^{3+} doping can stabilize the cubic phase down to 601~606 °C.¹⁹

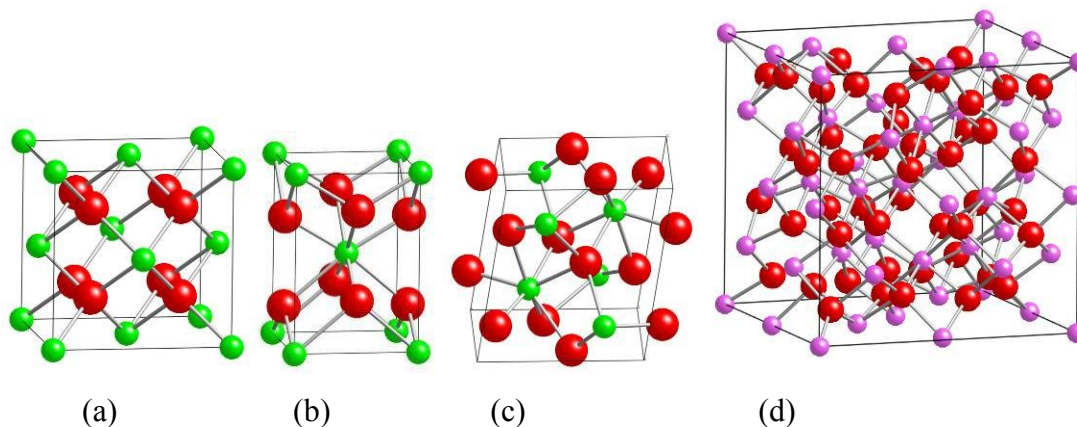
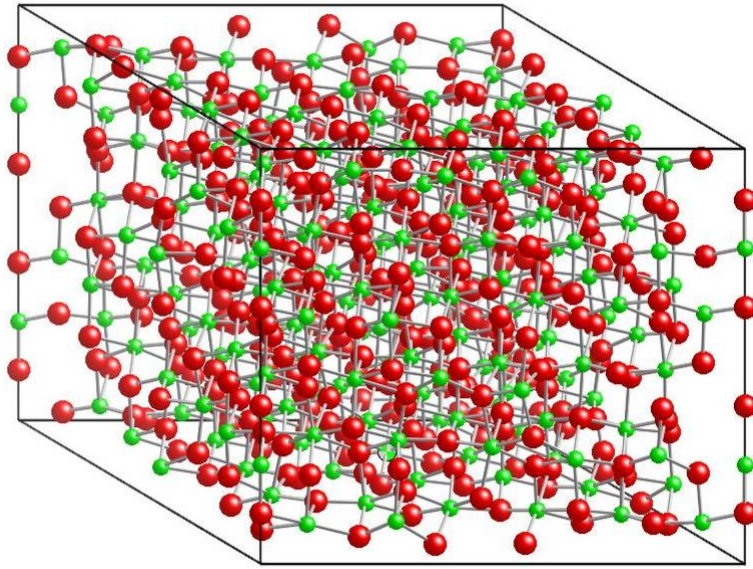


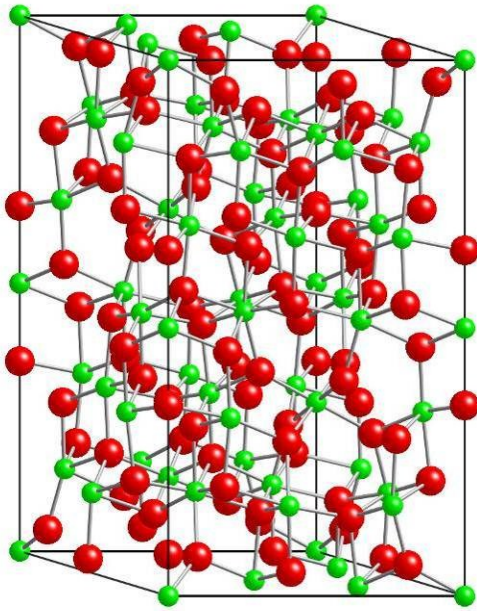
Figure 3. Structures of (a) cubic zirconia, (b) tetragonal zirconia, (c) monoclinic zirconia, and (d) C-type scandia.

The β ($Sc_{12}Zr_{50}O_{118}$), γ ($Sc_2Zr_5O_{13}$), δ ($Sc_4Zr_3O_{12}$) phases exist within the range of Sc^{3+} concentrations of 11.7~13%, 17~21.2%, 25~48%, respectively.¹⁹ They all have

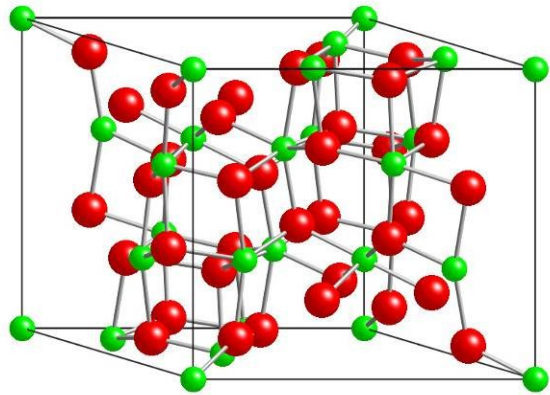
rhombohedral structure with the space group $R\bar{3}$, and can be viewed as distorted fluorite structures (Figure 4). Oxygen ion positions in the unit cell have been determined with neutron or X-ray diffractions for all three structures, but the cation arrangements are still unclear.⁵²⁻⁵⁴ Most studies did not report any cation ordering in these three phases.^{52,53,55,56} However, the neutron diffraction and ab-initio simulation of γ phase by Meyer et al. suggested a slight preference for Zr^{4+} to occupy the 3a Wyckoff position. The site occupation factors determined from the neutron study of β phase also showed some potential preferential occupations.⁵² For example, Zr:Sc ratio for one cation site (Zr(9), as named in the study) was determined to be 0.9293:0.0707.⁵² Bogicevic and Wolverton studied both γ and δ structures and identified their ground state cation arrangements with ab-initio simulations, although only some high symmetry configurations were investigated.^{57,58} Stanek further systematically simulated the δ phase, showing a preferential arrangement of Sc^{3+} on the cation positions, although the preference was suggested to be small.⁵⁹ The cation ordering relative to the oxygen vacancies positions in these phases are critical in understanding the defect structures in SDZ, because they could reveal the energetically stable structural arrangements of Sc^{3+} dopants and vacancies. Therefore, they were investigated and discussed in details later in this thesis.



(a)



(b)



(c)

Figure 4. Structures of (a) β , (b) γ , and (c) δ phases.

D. Overview

In this thesis, defect structures in GDC and SDZ were studied with computer simulations. The details of simulation techniques are introduced in Chapter 2. Chapter 3~5 study the defect structure and nano-domains in GDC. Chapter 6 focuses on the phase system of SDZ.

The basic defect associations and small defect clusters in GDC were modeled in Chapter 3, followed by simulations of large defect clusters and nano-domain structures in Chapter 4. The relationship between the defect structures and the phase system of GDC was studied. The effect of defect segregation in GDC, as well as means to prevent it, was also discussed in details. In Chapter 5, dynamic simulations were conducted to study the modulation of defect structures by mechanical strains, which could explain the non-linear mechanical properties of GDC and may serve as a possible method to limit the defect segregation. In these three chapters, simulations were carried out with classical empirical potentials.

Based on the understandings obtained with GDC, Chapter 6 focused on the cation ordering in the three rhombohedral phases in the SDZ system. Defect structures in SDZ were discussed based on the energetically preferred cation ordering in these three phases. Both classical and DFT ab-initio simulations were conducted in this chapter. Their results were compared to provide a critical assessment of these two methods for the simulation of the SDZ system.

References

1. S. C. Singhal, "Science and Technology of Solid-Oxide Fuel Cells," *MRS Bull.*, **25** [3] 16-21 (2000).
2. SECA, "Solid State Energy Conversion Alliance (SECA)" (2011) Accessed on: January, 2012. Available at <http://www.netl.doe.gov/technologies/coalpower/fuelcells/seca>
3. Bloom Energy, "Industry Leading Companies Choose Bloom Electrons for Immediate Cost Savings and Carbon Reduction Benefits" (2011) Accessed on: December, 2011. Available at http://www.bd.com/press/pdfs/Bloom_Electrons_Customer_Press_Release.pdf

4. B. C. H. Steele and A. Heinzl, "Materials for Fuel-Cell Technologies," *Nature*, **414** [6861] 345-52 (2001).
5. S. C. Singhal, "Solid Oxide Fuel Cells for Stationary, Mobile, and Military Applications," *Solid State Ionics*, **152-153** [0] 405-10 (2002).
6. H. Uchida, N. Maeda, and H. Iwahara, "Relation between Proton and Hole Conduction in SrCeO₃-Based Solid Electrolytes under Water-Containing Atmospheres at High Temperatures," *Solid State Ionics*, **11** [2] 117-24 (1983).
7. J. B. Goodenough, "Oxide-Ion Electrolytes," *Annu. Rev. Mater. Res.*, **33** [1] 91-128 (2003).
8. N. P. Brandon, S. Skinner, and B. C. H. Steele, "Recent Advances in Materials for Fuel Cells," *Annu. Rev. Mater. Res.*, **33** [1] 183-213 (2003).
9. H. A. Harwig and J. W. Weenk, "Phase Relations in Bismuth Sesquioxide," *Z. Anorg. Allg. Chem.*, **444** [1] 167-77 (1978).
10. E. Ivers-Tiffée, A. Weber, and D. Herbstritt, "Materials and Technologies for Sofc-Components," *J. Eur. Ceram. Soc.*, **21** [10-11] 1805-11 (2001).
11. K. Huang, M. Feng, J. B. Goodenough, and C. Milliken, "Electrode Performance Test on Single Ceramic Fuel Cells Using as Electrolyte Sr- and Mg-Doped LaGaO₃," *J. Electrochem. Soc.*, **144** [10] 3620-4 (1997).
12. D. J. L. Brett, A. Atkinson, N. P. Brandon, and S. J. Skinner, "Intermediate Temperature Solid Oxide Fuel Cells," *Chem. Soc. Rev.*, **37** [8] 1568-78 (2008).
13. O. Yamamoto, Y. Arati, Y. Takeda, N. Imanishi, Y. Mizutani, M. Kawai, and Y. Nakamura, "Electrical Conductivity of Stabilized Zirconia with Ytterbia and Scandia," *Solid State Ionics*, **79**, 137-42 (1995).
14. B. C. H. Steele, "Appraisal of Ce_{1-y}Gd_yO_{2-y/2} Electrolytes for IT-SOFC Operation at 500 °C," *Solid State Ionics*, **129** [1-4] 95-110 (2000).
15. N. Sammes and Y. Du, "Intermediate-Temperature SOFC Electrolytes"; pp. 19-34 in NATO Science Series, Vol. 202, *Fuel Cell Technologies: State and Perspectives*. Edited by N. Sammes, A. Smirnova, and O. Vasylyev. Springer Netherlands, 2005.
16. B. C. H. Steele, "Materials for IT-SOFC Stacks: 35 Years R&D: The Inevitability of Gradualness?," *Solid State Ionics*, **134** [1-2] 3-20 (2000).
17. H. Inaba and H. Tagawa, "Ceria-Based Solid Electrolytes," *Solid State Ionics*, **83** [1-2] 1-16 (1996).

18. D. Y. Wang, D. S. Park, J. Griffith, and A. S. Nowick, "Oxygen-Ion Conductivity and Defect Interactions in Yttria-Doped Ceria," *Solid State Ionics*, **2** [2] 95-105 (1981).
19. F. M. Spiridonov, L. N. Popova, and R. Y. Popil'skii, "On the Phase Relations and the Electrical Conductivity in the System ZrO_2 - Sc_2O_3 ," *J. Solid State Chem.*, **2** [3] 430-8 (1970).
20. S. P. S. Badwal and J. Drennan, "Microstructure/Conductivity Relationship in the Scandia-Zirconia System," *Solid State Ionics*, **53-56, Part 2** [0] 769-76 (1992).
21. D. J. M. Bevan and E. Summerville, "Mixed rare earth oxides"; pp. 401-524 in *Handbook of the Physics and Chemistry of Rare Earths*, Vol. 4. Edited by K. A. Gschneider and L. Eyring. Elsevier Science Publishers, North-Holland, Amsterdam, 1979.
22. L. Minervini, M. O. Zacate, and R. W. Grimes, "Defect Cluster Formation in M_2O_3 -Doped CeO_2 ," *Solid State Ionics*, **116** [3-4] 339-49 (1999).
23. P. Li, I. W. Chen, J. E. Penner-Hahn, and T. Y. Tien, "X-Ray Absorption Studies of Ceria with Trivalent Dopants," *J. Am. Ceram. Soc.*, **74** [5] 958-67 (1991).
24. S. Yamazaki, T. Matsui, T. Ohashi, and Y. Arita, "Defect Structures in Doped CeO_2 Studied by Using XAFS Spectrometry," *Solid State Ionics*, **136-137**, 913-20 (2000).
25. H. Deguchi, H. Yoshida, T. Inagaki, and M. Horiuchi, "EXAFS Study of Doped Ceria Using Multiple Data Set Fit," *Solid State Ionics*, **176** [23-24] 1817-25 (2005).
26. S. J. Hong and A. V. Virkar, "Lattice Parameters and Densities of Rare-Earth Oxide Doped Ceria Electrolytes," *J. Am. Ceram. Soc.*, **78** [2] 433-9 (1995).
27. W. Chen and A. Navrotsky, "Thermochemical Study of Trivalent-Doped Ceria Systems: CeO_2 - $MO_{1.5}$ (M = La, Gd, and Y)," *J. Mater. Res.*, **21** [12] 3242-51 (2006).
28. T. Mori, "Influence of Nano-Structural Feature on Electrolytic Properties of Gd Doped CeO_2 Solid Electrolytes," *J. Ceram. Soc. Jpn.*, **112** [1305] 642 (2004).
29. T. Mori and J. Drennan, "Influence of Microstructure on Oxide Ionic Conductivity in Doped CeO_2 Electrolytes," *J. Electroceram.*, **17** [2] 749-57 (2006).

30. F. Ye, T. Mori, D. R. Ou, J. Zou, G. Auchterlonie, and J. Drennan, "Compositional and Structural Characteristics of Nano-Sized Domains in Gadolinium-Doped Ceria," *Solid State Ionics*, **179** [21-26] 827-31 (2008).
31. R. Gerhardt-Anderson and A. S. Nowick, "Ionic Conductivity of CeO₂ with Trivalent Dopants of Different Ionic Radii," *Solid State Ionics*, **5**, 547-50 (1981).
32. N. Kim, C.-H. Hsieh, and J. F. Stebbins, "Scandium Coordination in Solid Oxides and Stabilized Zirconia: ⁴⁵Sc NMR," *Chem. Mater.*, **18** [16] 3855-9 (2006).
33. P. Jain, H. J. Avila-Paredes, C. Gapuz, S. Sen, and S. Kim, "High-Resolution ⁸⁹Y and ⁴⁵Sc NMR Spectroscopic Study of Short-Range Structural Order in Nanocrystalline Y- and Sc-Doped CeO₂ and ZrO₂," *J. Phys. Chem. C*, **113** [16] 6553-60 (2009).
34. M. O. Zacate, L. Minervini, D. J. Bradfield, R. W. Grimes, and K. E. Sickafus, "Defect Cluster Formation in M₂O₃-Doped Cubic ZrO₂," *Solid State Ionics*, **128** [1-4] 243-54 (2000).
35. R. Devanathan, S. Thevuthasan, and J. D. Gale, "Defect Interactions and Ionic Transport in Scandia Stabilized Zirconia," *Phys. Chem. Chem. Phys.*, **11** [26] 5506-11 (2009).
36. S. P. S. Badwal, F. T. Ciacchi, and D. Milosevic, "Scandia–Zirconia Electrolytes for Intermediate Temperature Solid Oxide Fuel Cell Operation," *Solid State Ionics*, **136-137** [0] 91-9 (2000).
37. K. Nomura, Y. Mizutani, M. Kawai, Y. Nakamura, and O. Yamamoto, "Aging and Raman Scattering Study of Scandia and Yttria Doped Zirconia," *Solid State Ionics*, **132** [3-4] 235-9 (2000).
38. C. Haering, A. Roosen, H. Schichl, and M. Schnöller, "Degradation of the Electrical Conductivity in Stabilised Zirconia System: Part II: Scandia-Stabilised Zirconia," *Solid State Ionics*, **176** [3-4] 261-8 (2005).
39. F. K. Moghadam, T. O. M. Yamashita, R. Sinclair, and D. A. Stevenson, "Transmission Electron Microscopy of Annealed ZrO₂ + 8 mol% Sc₂O₃," *J. Am. Ceram. Soc.*, **66** [3] 213-6 (1983).
40. W. Araki, T. Koshikawa, A. Yamaji, and T. Adachi, "Degradation Mechanism of Scandia-Stabilised Zirconia Electrolytes: Discussion Based on Annealing Effects on Mechanical Strength, Ionic Conductivity, and Raman Spectrum," *Solid State Ionics*, **180** [28-31] 1484-9 (2009).

41. F. Pietrucci, M. Bernasconi, A. Laio, and M. Parrinello, "Vacancy-Vacancy Interaction and Oxygen Diffusion in Stabilized Cubic ZrO₂ from First Principles," *Phys. Rev. B: Condens. Matter*, **78** [9] 094301 (2008).
42. R. Pornprasertsuk, P. Ramanarayanan, C. B. Musgrave, and F. B. Prinz, "Predicting Ionic Conductivity of Solid Oxide Fuel Cell Electrolyte from First Principles," *J. Appl. Phys.*, **98** [10] 103513-8 (2005).
43. G.-y. Adachi and N. Imanaka, "The Binary Rare Earth Oxides," *Chem. Rev.*, **98** [4] 1479 (1998).
44. H. R. Hoekstra, "Phase Relationships in the Rare Earth Sesquioxides at High Pressure," *Inorg. Chem.*, **5** [5] 754-7 (1966).
45. V. Grover and A. K. Tyagi, "Phase Relations, Lattice Thermal Expansion in CeO₂-Gd₂O₃ System, and Stabilization of Cubic Gadolinia," *Mater. Res. Bull.*, **39** [6] 859-66 (2004).
46. M. Zinkevich, "Thermodynamics of Rare Earth Sesquioxides," *Prog. Mater. Sci.*, **52** [4] 597-647 (2007).
47. K. E. Sickafus, L. Minervini, R. W. Grimes, J. A. Valdez, M. Ishimaru, F. Li, K. J. McClellan, and T. Hartmann, "Radiation Tolerance of Complex Oxides," *Science*, **289** [5480] 748-51 (2000).
48. D. Liu, W. Lei, Y. Li, Y. Ma, J. Hao, X. Chen, Y. Jin, D. Liu, S. Yu, Q. Cui, and G. Zou, "High-Pressure Structural Transitions of Sc₂O₃ by X-Ray Diffraction, Raman Spectra, and Ab Initio Calculations," *Inorg. Chem.*, **48** [17] 8251-6 (2009).
49. M. A. Clevinger, K. M. Hill, T. R. Green, C. C. Cedeno, E. Hayward, and N. Swanson, Phase Equilibrium Diagrams, Version 2.1, [CD-ROM] American Ceramic Society, Westerville, OH, 1993.
50. G. Teufer, "The Crystal Structure of Tetragonal ZrO₂," *Acta Crystallogr.*, **15** [11] 1187 (1962).
51. D. K. Smith and C. F. Cline, "Verification of Existence of Cubic Zirconia at High Temperature," *J. Am. Ceram. Soc.*, **45** [5] 249-50 (1962).
52. K. Wurst, E. Schweda, D. J. M. Bevan, J. Mohyla, K. S. Wallwork, and M. Hofmann, "Single-Crystal Structure Determination of Zr₅₀Sc₁₂O₁₁₈," *Solid State Sciences*, **5** [11-12] 1491-7 (2003).

53. M. R. Thornber, D. J. M. Bevan, and J. Graham, "Mixed Oxides of the Type $\text{MO}_2(\text{Fluorite})\text{-M}_2\text{O}_3$. III. Crystal Structures of the Intermediate Phases $\text{Zr}_5\text{Sc}_2\text{O}_{13}$ and $\text{Zr}_3\text{Sc}_4\text{O}_{12}$," *Acta Crystallogr. Sect. B: Struct. Sci.*, **24** [9] 1183-90 (1968).
54. S. Meyer, E. Schweda, N. J. Martinez Meta, H. Boysen, M. Hoelzel, and T. Bredow, "Neutron Powder Diffraction Study and DFT Calculations on the Structure of $\text{Zr}_{10}\text{Sc}_4\text{O}_{26}$," *Zeitschrift für Kristallographie*, **224** [11] 539-43 (2009).
55. H. Fujimori, M. Yashima, M. Kakihana, and M. Yoshimura, "Structural Changes of Scandia-Doped Zirconia Solid Solutions: Rietveld Analysis and Raman Scattering," *J. Am. Ceram. Soc.*, **81** [11] 2885-93 (1998).
56. D. J. M. Bevan, J. Mohyla, K. S. Wallwork, H. J. Rossell, and E. Schweda, "Structural Principles for Anion-Deficient, Fluorite-Related Superstructures in the Zirconia-Scandia System," *Z. Anorg. Allg. Chem.*, **628** [5] 1180-6 (2002).
57. A. Bogicevic and C. Wolverton, "Nature and Strength of Defect Interactions in Cubic Stabilized Zirconia," *Phys. Rev. B: Condens. Matter*, **67** [2] 024106 (2003).
58. A. Bogicevic, C. Wolverton, G. M. Crosbie, and E. B. Stechel, "Defect Ordering in Aliovalently Doped Cubic Zirconia from First Principles," *Phys. Rev. B: Condens. Matter*, **64** [1] 014106 (2001).
59. C. R. Stanek, C. Jiang, B. P. Uberuaga, K. E. Sickafus, A. R. Cleave, and R. W. Grimes, "Predicted Structure and Stability of $\text{A}_4\text{B}_3\text{O}_{12}$ Δ -Phase Compositions," *Phys. Rev. B: Condens. Matter*, **80** [17] 174101 (2009).

CHAPTER 2. METHOD

Various computer simulation techniques were involved in this thesis. They were chosen based on the nature of the problem. Classical approaches with empirical potential models were adopted to study the defect structures in GDC, wherein static lattice optimizations were used to simulate perfect lattices and defect structures, and molecular dynamics was utilized to simulate the dynamic modulation of the defect structure by strain. Classical simulations are much less computationally demanding compared to ab-initio methods, allowing for simulations of larger systems and with longer time scales. And because the potentials are fitted from experimental data, high fidelity can be achieved when the approximations made in the method are reasonable under the simulated physical conditions. However, classical techniques become less versatile when dealing with complex structures and phase systems. For instance, no classical potential model has been able to reproduce all the common polymorphs of zirconia. As a result, for the simulations of SDZ system, ab-initio method based on the density functional theory (DFT) was chosen for predicting the phase structures and examining the classical empirical potentials in the literature.

A. Classical simulation techniques

In the frame of classical simulation techniques, the lattice energy is the binding energy or cohesive energy of the crystal structure and is calculated in the Born Model of the solid through the summation of long range (Coulomb) and short-range potentials acting between atoms.¹ The short-ranged potentials are usually obtained by fitting the material properties measured experimentally or calculated from ab-initio methods.

In this thesis, two types of classical simulation techniques were exploited: structure optimization and molecular dynamics. The GULP package² was used for structure optimizations and the DL_POLY package³ for molecular dynamics simulations.

1. Short-ranged potentials

This work used a Buckingham potential for the simulations of GDC. Cutoffs of 20 Å and 15 Å for short-range interactions were used for structure optimizations and molecular dynamics, respectively, according to the size of the simulation. The polarizability of Ce^{4+} and O^{2-} was included in this study by using the shell model. A set of potential parameters developed by Minervini et al. (Table I and Table II) was chosen, which has been successfully applied in studies of defect structure in ceria based electrolyte,^{4,6} rare earth – fluorite oxides phase relations and defect structures in pyrochlore-type compounds.^{7,8} These parameters have been proven to reproduce ceria and gadolinia structures and properties, as well as gadolinia phases and their energy ordering.^{4,6}

Table I. Short-Range Potential Parameters for GDC

Interaction	A (eV)	ρ (Å)	C (eVÅ ⁶)	Reference
$\text{Ce}^{4+}\text{-O}^{2-}$	1809.68	0.3547	20.40	[9]
$\text{Gd}^{3+}\text{-O}^{2-}$	1885.75	0.3399	20.34	[4]
$\text{O}^{2-}\text{-O}^{2-}$	9547.96	0.2192	32.0	[10]

Table II. Shell Model Parameters for GDC

Interaction	Shell charge (e)	K (eVÅ ⁻²)	Reference
Ce^{4+}	-0.20	177.84	[9]
O^{2-}	-2.04	6.3	[10]

2. Structure optimization

Structure optimization is to minimize the lattice energy of a perfect or defect lattice by static lattice relaxation. Minimized energies of different structural configurations can be used to discriminate between configurations that are more

energetically stable and those less stable. The static lattice relaxation is performed by moving the core-shell coordinates in an effort to minimize the forces acting upon them.¹¹

It is worth a more detailed introduction of the structure optimization of lattices with defects. The optimization of a defect structure in this thesis was done by minimizing the defect energy, which was the energy difference between the defect structure and the perfect (defect-free) lattice. The defect energy was calculated by a Mott-Littleton two-region approach,¹² which was coded in the GULP program.² A spherical region I centered at the defects, where the atomic structure was strongly perturbed by the defects, was treated atomistically. The rest of the crystal, region II, was treated as a continuum where the displacements were only due to the defect charge at the defect center. An interfacial region IIA was introduced between regions I and II to ensure consistency of the two different means of evaluation. To make sure that the region I size chosen was adequate to accommodate the large defect clusters in this study, an initial test of the region size on the largest defect cluster to be used was performed. The test indicated that increasing the radius beyond 25 Å resulted in a negligible change in the defect energy calculated. Therefore, the region I radius was set to 25 Å (including around 10,000 atom cores and shells in our simulations) and that of region IIA to 46 Å (which includes around 50,000 atom cores and shells in our simulations). Unit Hessian optimization was adopted to reduce the memory requirement of the calculations.

The defect energy was compared with the sum of the individual defects, and the binding energies could be calculated as:

$$E_{binding} = \sum E_{isolated\ defect} - E_{defect\ cluster} \quad (2)$$

The total binding energy was divided by the number of oxygen vacancies in the defect cluster, in order to compare clusters of different size. A positive binding energy indicated that clustering was energetically favorable, and higher binding energies corresponded to the more stable structures.

Because of the “static” nature of structure optimization, the temperature effect, which was manifested through entropy contributions to the total energy, was ignored. For questions of interest in the simulation of GDC defect structures, two types of entropies,

vibrational and configurational entropies, might be of concern. The former, the vibrational entropy, could be approximated using free energy minimization methods, and, according to previous simulation experience, was minimal at least below 1500K for defect structures investigated in this study. The later, configurational entropy, became non-negligible when the temperature was high enough for atomic diffusion to occur. However, there would still be no substantial difference in configurational entropy when comparing highly ordered structures containing similar number of atoms. The configurational entropy difference between ordered and randomized structures is discussed qualitatively in this thesis.

3. Molecular dynamics

Molecular dynamics (MD) is a technique to simulate the dynamics of atomic systems by calculating the velocity and position of atoms with classical Newtonian physics.¹ The forces were determined from empirical interatomic potentials in the MD simulations carried out in this thesis. It should be noted that MD could also be combined with the quantum mechanics method to determine the forces in an ab-initio manner.

In the MD simulations of GDC, a simulation box containing a supercell of $6 \times 6 \times 6$ ceria unit cells was set up with three-dimensional periodic boundary conditions. At the beginning of simulation, interatomic forces were calculated with the initial positions of the atoms in the simulation box. The atoms were then allowed to move according to Newton's laws of motion for a small period of time (0.5~1 fs in this work, depending on the temperature and the stage of the simulation). The forces were then updated with the new positions of the atoms. In this way, the simulation continued iteratively until desired simulation time was obtained. As the time step was sufficiently small compared with the thermal vibration frequency of the atoms (usually considered being at the level of 10^{-12} second), the temperature effect could be properly probed in the simulations. As a result, time-dependent and temperature-dependent material properties could be extracted from the simulations.

The polarizability of Ce^{4+} and O^{2-} was incorporated in the MD simulations with shell models through the relaxed shell method. In the relaxed shell method, the positions of massless shells are relaxed at each time step in response to the core coordinates.¹³ It was found that the relaxed shell method allowed for larger time steps for the MD

simulations in this thesis, compared to the alternative adiabatic shell method, where a small fraction of the atomic mass was assigned to the shells to allow them being incorporated into the dynamic simulation.¹⁴ Different time steps were used for different temperatures and stages in this study to ensure convergence could be reached efficiently throughout the simulation.

B. Ab-initio simulation with density functional theory

Different from classical techniques, simulations utilizing quantum physics determine the interaction between atoms from the electronic behavior. Since no empirical data are required, the simulations can be performed in an “ab-initio” manner. In this thesis, ab-initio method based on density functional theory (DFT) was used to simulate the SDZ phase system.

In the density functional theory, the electronic system is described by the electron density, instead of the many-body electron wave function.¹⁵ Modern DFT adopts the Kohn-Sham method to deal accurately with interacting many-electron systems by solving the Kohn-Sham equation of non-interacting electrons under an effective potential.¹⁶ This allows for efficient ab-initio simulations with sufficient accuracy. In this thesis, the SIESTA (Spanish Initiative for Electronic Simulations with Thousands of Atoms) package¹⁷ was used for the simulations of the SDZ phase system. Both the force evaluation with DFT method and the subsequent structure optimizations of SDZ structures were performed with SIESTA. The results were used to predict the cation ordering in these structures and to evaluate the classical potential models in the literature.

For DFT calculations, some user choices of simulation parameters may have significant impact on the accuracy of the final results. For example, in SIESTA, the mesh cutoff parameter determines the fineness of the three dimension grid used for integrations and representations of charge density and potentials.¹⁷ The simulations in this thesis used a 250 Ry as the mesh cutoff, which means a function can be Fourier transformed back and forth without any approximation if it can be expanded to periodic plane waves with kinetic energy lower than 250 Ry. Another important parameter regarding sampling precision is the k-grid cutoff, which determines the fineness of the grid in the reciprocal space.¹⁷ The k-grid cutoffs in the simulations were chosen based on the size of unit cell.

1×1×1 k-grids were used for structures with large unit cells, such as C-type scandia and the β phase. 2×2×2 k-grids were used for the δ and γ phases, and 4×4×4 k-grids for zirconia. Besides these two parameters, other parameters critical to the final accuracy in the simulations are mainly related to three aspects of the DFT simulation technique: the exchange-correlation functional, pseudopotentials and basis set. They are introduced in details in the following sections.

1. Exchange-correlation functional

The Kohn-Sham method separates out the contribution of electron exchange and correlation from the total energy, but the exact functional of this term is unknown except for the free electron gas.¹⁶ Therefore, approximation must be made for the exchange-correlation energy. The simplest method is the local density approximation (LDA), where the exchange-correlation energy is approximated to depend only on the electron density.¹⁶ LDA usually can predict the material structure sufficiently well, but overestimates the bonding energy.¹⁸⁻²⁰ Also, uncertainties have been observed in calculating the relative phase stability of bulk crystals with LDA.^{18,21} Generalized gradient approximation (GGA) improved on LDA by making the exchange-correlation energy also depend on the electron density gradient.²²⁻²⁴ A previous study showed that GGA was necessary to accurately describe the energy difference between the zirconia polymorphs.²⁵ Therefore, PBEsol, a GGA functional developed and tuned for densely-packed solids by Perdew, et al.,²⁴ was chosen for the simulations of the SDZ phase system.

2. Pseudopotentials

DFT calculations are usually computationally demanding. It becomes exceedingly difficult when a material containing heavy elements is simulated and all the electrons are considered. One method to mitigate such situation is the pseudopotential approximation.^{26,27} The pseudopotential approximation is based on the fact that most properties of solids depend much more on the valence electrons than on the core electrons. It replaces the core electrons with an effective pseudopotential, which reduces the number of electrons that needs to be considered and also avoids the calculation of rapid oscillating wave functions in the core region caused by the strong Coulomb potentials.

In this thesis, norm conserving pseudopotentials were generated with the Troullier-Martins scheme²⁸ using the SIESTA ATOM generator¹⁷. The valence electron configurations were $5s^24d^2$ for Zr, $3d^14s^2$ for Sc and $2s^22p^4$ for O. Matching radii were based on the values from the Fritz-Haber-Institute pseudopotential database:²⁹ 2.96 bohrs for Zr 5s, 2.61 bohrs for Zr 4d, 2.47 bohrs for Sc 3d, 2.77 bohrs for Sc 4s, 1.41 bohrs for O 2s and 2p. Non-linear core correction was included to account for the overlap between core and valence wave functions³⁰, with matching radii of 5.1 bohrs for Zr, 2.85 bohrs for Sc and 1.0 bohrs for O.

3. Basis set

In DFT simulations, the Kohn-Sham wave functions are expanded onto linear combination of basis functions. The SIESTA package used in this thesis adopts numerical atomic orbital-like basis.¹⁷ The quality of the basis set can be judged from three aspects: size (number of orbitals per atom), range (cutoff radii of orbitals) and radial shape (mainly concerning how the orbitals are confined). For the simulations in this thesis, the related parameters were set as following: double ζ polarized (DZP) basis set, which contained two radial functions for every angular momentum channel plus a polarization orbital, was chosen for the size of basis set; the cutoff was set in a way that a 0.001 Ry energy increase was caused by the confinement of orbitals; and the built-in soft-confinement scheme in SIESTA was used.¹⁷

References

1. C. R. A. Catlow and E. A. Kotomin, "Computational Materials Science"; p. 1-29 in NATO Science Series, Vol. 187. IOS Press, Ohmsha, 2003.
2. J. D. Gale and A. L. Rohl, "The General Utility Lattice Program (GULP)," *Mol. Simul.*, **29** [5] 291-341 (2003).
3. W. Smith, "Guest Editorial: DL_POLY–Applications to Molecular Simulation II," *Mol. Simul.*, **32** [12-13] 933- (2006).
4. L. Minervini, M. O. Zacate, and R. W. Grimes, "Defect Cluster Formation in M_2O_3 -Doped CeO_2 ," *Solid State Ionics*, **116** [3-4] 339-49 (1999).

5. F. Ye, T. Mori, D. R. Ou, J. Zou, and J. Drennan, "A Structure Model of Nano-Sized Domain in Gd-Doped Ceria," *Solid State Ionics*, **180** [26-27] 1414-20 (2009).
6. B. Wang, R. J. Lewis, and A. N. Cormack, "Atomistic Simulation of B-Type-Fluorite Structural Relationship and B-Type Large Defect Clusters in Gadolinia-Doped Ceria," *Solid State Ionics*, **182** [1] 8-12 (2011).
7. M. Licia, W. G. Robin, and E. S. Kurt, "Disorder in Pyrochlore Oxides," *J. Am. Ceram. Soc.*, **83** [8] 1873-8 (2000).
8. K. E. Sickafus, L. Minervini, R. W. Grimes, J. A. Valdez, M. Ishimaru, F. Li, K. J. McClellan, and T. Hartmann, "Radiation Tolerance of Complex Oxides," *Science*, **289** [5480] 748-51 (2000).
9. G. Busker, A. Chroneos, R. W. Grimes, and I.-W. Chen, "Solution Mechanisms for Dopant Oxides in Yttria," *J. Am. Ceram. Soc.*, **82** [6] 1553-9 (1999).
10. R. W. Grimes, D. J. Binks, and A. B. Lidiard, "The Extent of Zinc Oxide Solution in Zinc Chromate Spinel," *Philos. Mag. A*, **72** [3] 651 - 68 (1995).
11. C. R. A. Catlow, A. N. Cormack, and F. Theobald, "Structure Prediction of Transition-Metal Oxides Using Energy-Minimization Techniques," *Acta Crystallogr. Sect. B: Struct. Sci.*, **40** [3] 195-200 (1984).
12. A. Dwivedi and A. N. Cormack, "Computer Simulation Study of the Defect Structure of Calcia-Stabilized Zirconia," *Philos. Mag. A*, **61** [1] 1-22 (1990).
13. P. J. D. Lindan and M. J. Gillan, "Shell-Model Molecular Dynamics Simulation of Superionic Conduction in CaF₂," *J. Phys.: Condens. Matter*, **5** [8] 1019 (1993).
14. P. J. Mitchell and D. Fincham, "Shell Model Simulations by Adiabatic Dynamics," *J. Phys.: Condens. Matter*, **5** [8] 1031 (1993).
15. P. Hohenberg and W. Kohn, "Inhomogeneous Electron Gas," *Phys. Rev.*, **136** [3B] B864-B71 (1964).
16. W. Kohn and L. J. Sham, "Self-Consistent Equations Including Exchange and Correlation Effects," *Phys. Rev.*, **140** [4A] A1133-A8 (1965).
17. M. S. José, A. Emilio, D. G. Julian, G. Alberto, J. Javier, O. Pablo, and S.-P. Daniel, "The Siesta Method for Ab Initio Order- N Materials Simulation," *J. Phys.: Condens. Matter*, **14** [11] 2745 (2002).
18. J. M. Seminario, *Recent Developments and Applications of Modern Density Functional Theory*; p. 239-94. Elsevier, Amsterdam; New York, 1996.

19. D. R. Hamann, "H₂O Hydrogen Bonding in Density-Functional Theory," *Phys. Rev. B: Condens. Matter*, **55** [16] R10157-R60 (1997).
20. F. Tran, R. Laskowski, P. Blaha, and K. Schwarz, "Performance on Molecules, Surfaces, and Solids of the Wu-Cohen GGA Exchange-Correlation Energy Functional," *Phys. Rev. B: Condens. Matter*, **75** [11] 115131 (2007).
21. C. S. Wang, B. M. Klein, and H. Krakauer, "Theory of Magnetic and Structural Ordering in Iron," *Phys. Rev. Lett.*, **54** [16] 1852-5 (1985).
22. D. C. Langreth and M. J. Mehl, "Beyond the Local-Density Approximation in Calculations of Ground-State Electronic Properties," *Phys. Rev. B: Condens. Matter*, **28** [4] 1809-34 (1983).
23. J. P. Perdew, K. Burke, and M. Ernzerhof, "Generalized Gradient Approximation Made Simple," *Phys. Rev. Lett.*, **77** [18] 3865-8 (1996).
24. J. P. Perdew, A. Ruzsinszky, G. I. Csonka, O. A. Vydrov, G. E. Scuseria, L. A. Constantin, X. Zhou, and K. Burke, "Restoring the Density-Gradient Expansion for Exchange in Solids and Surfaces," *Phys. Rev. Lett.*, **100** [13] 136406 (2008).
25. G. Jomard, T. Petit, A. Pasturel, L. Magaud, G. Kresse, and J. Hafner, "First-Principles Calculations to Describe Zirconia Pseudopolymorphs," *Phys. Rev. B: Condens. Matter*, **59** [6] 4044 (1999).
26. B. J. Austin, V. Heine, and L. J. Sham, "General Theory of Pseudopotentials," *Phys. Rev.*, **127** [1] 276-82 (1962).
27. D. R. Hamann, M. Schlüter, and C. Chiang, "Norm-Conserving Pseudopotentials," *Phys. Rev. Lett.*, **43** [20] 1494-7 (1979).
28. N. Troullier and J. L. Martins, "Efficient Pseudopotentials for Plane-Wave Calculations," *Phys. Rev. B: Condens. Matter*, **43** [3] 1993-2006 (1991).
29. M. Fuchs and M. Scheffler, "Ab Initio Pseudopotentials for Electronic Structure Calculations of Poly-Atomic Systems Using Density-Functional Theory," *Comput. Phys. Commun.*, **119** [1] 67-98 (1999).
30. S. G. Louie, S. Froyen, and M. L. Cohen, "Nonlinear Ionic Pseudopotentials in Spin-Density-Functional Calculations," *Phys. Rev. B: Condens. Matter*, **26** [4] 1738-42 (1982).

CHAPTER 3. DEFECT STRUCTURES IN GDC

A. Basic defect association

In the ceria based electrolytes, trivalent dopants are commonly used. Dopant addition creates oxygen vacancies, and, at the same time, also forms associations with these vacancies. The binding energy of the association increases the activation energy for anion conduction. Regarding the selection of dopants, there is an empirical guideline which indicates that the best dopant would be the one which has an ion radius closest to that of the host cation in order to cause as little lattice distortion as possible.¹⁻³ Using the interatomic distances obtained from the defect simulations and the radius for the oxygen ion of 1.26 Å, suggested by R. D. Shannon,⁴ the dopant radius in ceria for Y^{3+} and In^{3+} could be derived as 1.15 Å and 1.11 Å. Either of these could have been better candidates for ceria-based electrolytes (simulated radius of $Ce^{4+}=1.08$ Å) than Gd^{3+} (simulated radius=1.17 Å). However in practice, gadolinia-doped ceria (GDC) has shown the highest oxygen ion conductivity amongst single-dopant, ceria based electrolytes.^{1,5,6}

An optimum dopant provides for high oxygen mobility that should result from a weak binding between the dopant and vacancy. However, the small lattice distortions created by the dopant cannot guarantee weak binding. It has been proven, in various cases, the Coulomb interaction together with the elastic lattice relaxation determines the interactions between defects.⁷⁻⁹ In this case, since dopants and oxygen vacancies have opposite effective charges, the Coulomb interaction tends to force them to reside as close together as possible. However, previous studies,⁹ in addition to the simulations conducted in this thesis, have shown that whilst small dopants prefer to associate in the nearest neighbor (NN) configuration, larger dopants prefer next nearest neighbor (NNN) configurations. This can be explained by the elastic lattice relaxation which depends on the size of the dopant. Figure 5 illustrates the lattice distortion around a single oxygen vacancy, as well as both nearest neighbor (NN) and next nearest neighbor (NNN) pairs. It can be seen that the NNN configuration is more accommodating to a larger dopant because of the lattice contraction around the vacancy. Therefore a larger dopant would

have a strong binding with the oxygen vacancy at its NNN site due to the more dominant elastic lattice relaxation, while a small dopant binds with the vacancy at its NN site because of the stronger Coulomb attraction. If the actual dopant size were a perfect match with Ce^{4+} , there would still be a preference for the vacancy to occupy the NN site, which means the NN configuration would have a higher binding energy. As the dopant increases in size, the binding energy of the NN configuration decreases, but that of NNN configuration increases. The binding energy reaches the minimum when NN and NNN configurations are equally stable. Therefore, the best dopant would be a larger dopant with the size that results in a balance between the Coulomb interaction and elastic lattice relaxation, so that it has no particular preference between the NN and NNN configurations. In the case of Gd^{3+} , its size is larger than that of Ce^{4+} and the oxygen vacancy has only a slight preference for NNN (binding energy = 0.36 eV) over NN (0.32 eV) which makes it almost the ideal dopant.

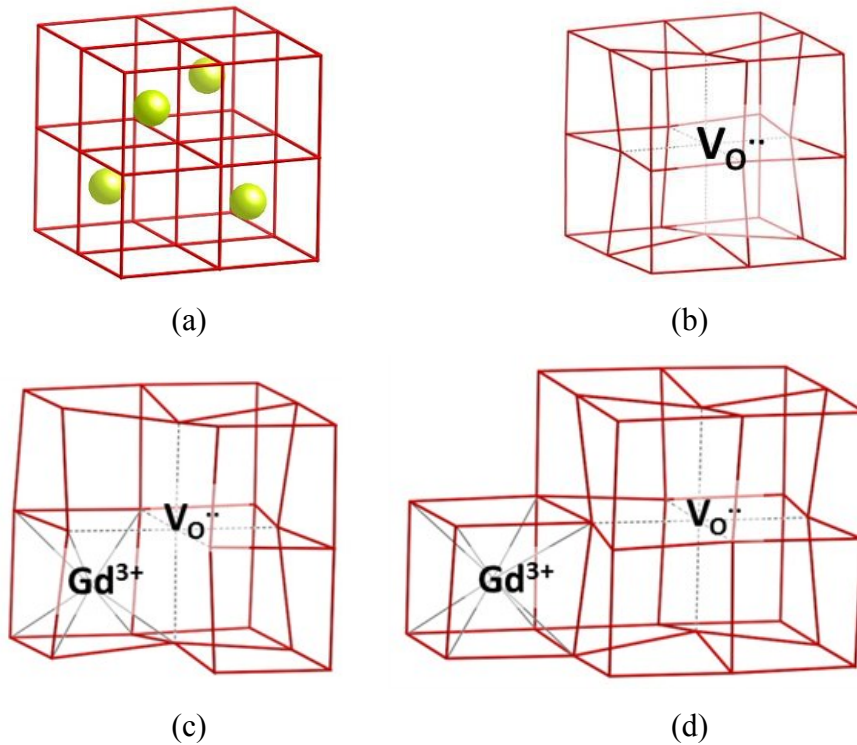


Figure 5. (a) The structure of fluorite CeO_2 . Lattice distortions around an oxygen vacancy, showing (b) lattice contraction around the vacancy, (c) a Gd^{3+} - $\text{V}_\text{O}^{\bullet\bullet}$ pair in NN configuration and (d) a Gd^{3+} - $\text{V}_\text{O}^{\bullet\bullet}$ pair in NNN configuration. The oxygen sublattice is illustrated by the red lines, Ce^{4+} cations are shown as the golden spheres only in (a), the perfect CeO_2 structure.

One should keep in mind that the resulting association pattern is dependent on the interaction between all of the dopants, vacancies and the host lattice. Therefore the association pattern is subject to change if the local host lattice is heavily distorted, as in, for instance, when the local dopant concentration is high. Conditions of high dopant concentration are discussed later in this thesis.

B. Small clusters

Association of defects is the primary factor that affects relationships between doping concentration and material properties. In previous studies, basic dopant-vacancy-dopant trimers, which are electrostatically neutral, have been studied to explain these relationships.^{9,10} However, the nonlinearity observed in these relations, such as the variation of lattice parameters¹¹⁻¹³ and conductivity^{14,15} with doping concentration, suggests that there is nonlinearity in the defect association. The increase in doping concentration not only would create more basic trimers, but also would allow small association complexes to grow into larger, more stable defect clusters. In order to examine these complexes, aggregates containing different numbers of defects were modeled and their binding energies per oxygen vacancy were compared. Charge neutrality was ensured in these simulations according to Equation (1).

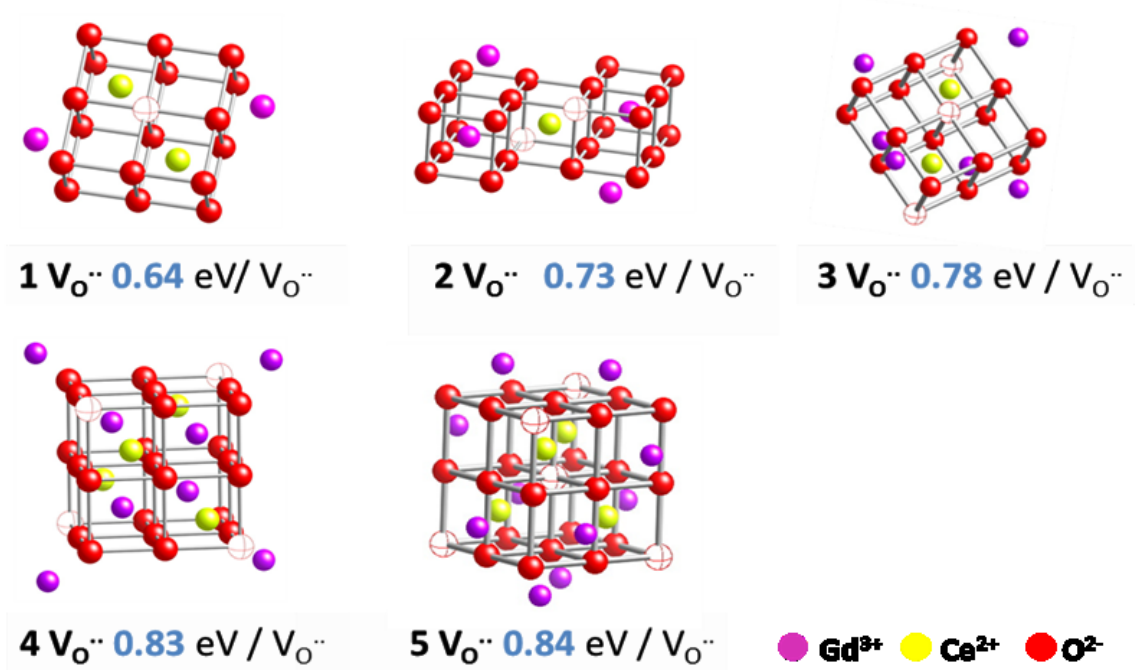


Figure 6. Stable charge neutral defect clusters containing increasing number of oxygen vacancies from 1 to 5 with binding energies shown below each cluster. Beach balls indicate the position of oxygen vacancies.

The most stable, or highest binding energy, clusters, of over 50 clusters considered in the present study, containing from one to five vacancies each, are shown in Figure 6. The binding energy per oxygen vacancy for each cluster is indicated within the figure. Because of the enormous number of possible configurations (e.g., several hundred for clusters containing 4 vacancies; each calculation could take more than one day to finish), it was not possible to test all possible configurations when the number of oxygen vacancies in the cluster exceeds three. However, it was found that clusters generally had higher binding energy per oxygen vacancy when they contain more defects. As shown in Figure 6, the binding energy per oxygen vacancy gradually increased with the number of defects. This suggested that the clusters became increasingly stable, which confirmed the tendency of defects to grow into larger clusters. It was also found that, for clusters at these sizes, it was generally much easier to find high binding energies when the vacancies were at dopant NNN site than at NN site. Actually, in all of these high binding energy clusters discovered in this study, the vacancies were all located at the dopant NNN sites. It is of some interest that all of the clusters illustrated are, in fact, fragments of pyrochlore

structure (“Gd₂Ce₂O₇”). It has been reported that defect clusters of C-type-like strings containing as many as 4 oxygen vacancies have a substantial binding energy.¹⁶ However a relatively small region I size was used in the earlier study. Similar C-type defect clusters were tested in this study with much larger region I size of 25 Å and none of them showed a larger binding energy than the pyrochlore-type clusters containing the same number of defects found in this thesis.

The pyrochlore structure, Gd₂Ce₂O₇, can be viewed as being derived from a fluorite ceria supercell which contains 8 ceria unit cells. It can be obtained by substituting half of the Ce⁴⁺ in the fluorite CeO₂ supercell with Gd³⁺ while creating oxygen vacancies at the NNN sites of Gd³⁺. Actually, if the structure is compact and formed strictly of the NNN configuration, then the structure should be pyrochlore. Any nonconformity with pyrochlore structure creates configurations in which some oxygen vacancies are at dopant NN sites, and according to the simulation results, usually decreases the binding energy.

C. Conclusions

In this chapter, the defect associations in GDC were studied with classic atomistic simulations. For the basic dopant oxygen - vacancy pair, the gadolinium dopant showed only a slight preference for the vacancy to be at a NNN rather than a NN site. As previously established, a small preference was beneficial towards minimizing the binding energy between the dopant and vacancy. Therefore, from the perspective of creating oxygen vacancies while minimizing the binding between dopant and vacancy, Gd³⁺ is nearly ideal for a single dopant within the ceria based electrolyte. However, this chapter showed that a trend exists whereby the defects tended to form large size clusters, and this trend must be taken into consideration since they would have a strong impact on the material properties.

Small clusters studied in this chapter showed binding energies that increased, from 0.64 eV to 0.84 eV per oxygen vacancy, with the number of oxygen vacancies increasing from 1 to 5. All these high binding energy clusters had a pyrochlore-type structure, where the oxygen vacancies were at the dopant NNN sites.

References

1. R. Gerhardt-Anderson and A. S. Nowick, "Ionic Conductivity of CeO₂ with Trivalent Dopants of Different Ionic Radii," *Solid State Ionics*, **5**, 547-50 (1981).
2. J. A. Kilner and R. J. Brook, "A Study of Oxygen Ion Conductivity in Doped Non-Stoichiometric Oxides," *Solid State Ionics*, **6** [3] 237-52 (1982).
3. C. R. A. Catlow, "Transport in Doped Fluorite Oxides," *Solid State Ionics*, **12**, 67-73 (1984).
4. R. Shannon, "Revised Effective Ionic Radii and Systematic Studies of Interatomic Distances in Halides and Chalcogenides," *Acta Crystallogr. Sect. A: Found. Crystallogr.*, **32** [5] 751-67 (1976).
5. J. Faber, C. Geoffroy, A. Roux, A. Sylvestre, and P. Abélard, "A Systematic Investigation of the DC Electrical Conductivity of Rare-Earth Doped Ceria," *Appl. Phys. A*, **49** [3] 225-32 (1989).
6. H. Yahiro, K. Eguchi, and H. Arai, "Electrical Properties and Reducibilities of Ceria-Rare Earth Oxide Systems and Their Application to Solid Oxide Fuel Cell," *Solid State Ionics*, **36** [1-2] 71-5 (1989).
7. A. N. Cormack, C. R. A. Catlow, and A. S. Nowick, "Theoretical Studies of Off-Centre Sc³⁺ Impurities in CeO₂," *J. Phys. Chem. Solids*, **50** [2] 177-81 (1989).
8. A. K. A. Pryde, S. Vyas, R. W. Grimes, J. A. Gardner, and R. Wang, "Cadmium and Indium Defects in Ceria and Their Interaction with Oxygen Vacancies and Small Polarons," *Phys. Rev. B: Condens. Matter*, **52** [18] 13214 (1995).
9. L. Minervini, M. O. Zacate, and R. W. Grimes, "Defect Cluster Formation in M₂O₃-Doped CeO₂," *Solid State Ionics*, **116** [3-4] 339-49 (1999).
10. H. Inaba, R. Sagawa, H. Hayashi, and K. Kawamura, "Molecular Dynamics Simulation of Gadolinia-Doped Ceria," *Solid State Ionics*, **122** [1-4] 95-103 (1999).
11. D. J. M. Bevan and E. Summerville, "Mixed rare earth oxides"; pp. 401-524 in *Handbook of the Physics and Chemistry of Rare Earths*, Vol. 4. Edited by K. A. Gschneider and L. Eyring. Elsevier Science Publishers, North-Holland, Amsterdam, 1979.
12. S. J. Hong and A. V. Virkar, "Lattice Parameters and Densities of Rare-Earth Oxide Doped Ceria Electrolytes," *J. Am. Ceram. Soc.*, **78** [2] 433-9 (1995).

13. W. Chen and A. Navrotsky, "Thermochemical Study of Trivalent-Doped Ceria Systems: $\text{CeO}_2\text{-MO}_{1.5}$ (M = La, Gd, and Y)," *J. Mater. Res.*, **21** [12] 3242-51 (2006).
14. D. Y. Wang, D. S. Park, J. Griffith, and A. S. Nowick, "Oxygen-Ion Conductivity and Defect Interactions in Ytria-Doped Ceria," *Solid State Ionics*, **2** [2] 95-105 (1981).
15. H. Inaba and H. Tagawa, "Ceria-Based Solid Electrolytes," *Solid State Ionics*, **83** [1-2] 1-16 (1996).
16. F. Ye, T. Mori, D. R. Ou, A. N. Cormack, R. J. Lewis, and J. Drennan, "Simulation of Ordering in Large Defect Clusters in Gadolinium-Doped Ceria," *Solid State Ionics*, **179** [35-36] 1962-7 (2008).

CHAPTER 4. NANO-DOMAINS IN GDC

Results from the previous chapter suggest that extended defect clusters were fragments of the pyrochlore structure (NNN configuration). However, the preference for the NNN configuration is the result of the effect of the ceria lattice environment on Gd^{3+} dopants as described in Chapter 3A. In other words, the ceria host lattice has a stabilizing effect on the pyrochlore-type structure, which is effective only in a relatively Ce^{4+} rich environment. In a region with high dopant concentration, there is a possibility that the effect of the ceria lattice will be “shaded” by the sparseness of the cerium cations and the NNN configuration will no longer be preferred. Therefore, while the structure of the small defect complexes appears to prefer the NNN configuration, larger defect clusters, such as defect nano-domains, may not. Thus, it is essential that nano-domain structure be studied as well.

Experiments have shown that defect clusters and, especially, nano-domains, grow in size with increasing doping concentration.^{1,2} Eventually, they would be distinguishable from the host structure at the macroscopic level and become a second phase. Therefore large defect clusters and nano-domains serve as the precursor of phase separation, and can be viewed as defect clusters large enough to have fully developed secondary phase structure.^{3,4} Thus, it is reasonable to assume that the nano-domain structure corresponds to those of phases in the gadolinia-ceria phase system. This phase system includes the B-type and C-type rare earth, fluorite, and possibly pyrochlore phases.^{3,4} Indeed, SAED results have indicated nano-domains may exist as either B-type, C-type or pyrochlore.^{1,2,5} Therefore, defect clusters large enough to represent a fully developed secondary phase structure need to be tested. A unit cell is really the smallest unit which possesses the intrinsic characteristics of the structure, and therefore became a suitable candidate for the test. Simulations of large defect clusters containing unit cells of these three structures were conducted and the results are discussed in this chapter.

A. B-type rare earth structure

Although recent experimental data pointed to the likelihood of a cubic structured nano-domain², they could not rule out the possibility of the (monoclinic) B-type. Indeed, early studies had suggested the B-type structure for the nano-domains.⁵ In addition, although previous studies have reported that C-type gadolinia transforms to B-type above 1200-1425 °C, the reversion from B-type to C-type was found to be much more difficult, and required weeks of annealing.⁶⁻⁸ Therefore it is possible that nano-domains form during the sintering of GDC with a B-type related structure which is retained on cooling. Additionally, unlike C-type and pyrochlore structures, which are cubic, the B-type is monoclinic and its compatibility with the cubic ceria host lattice (fluorite) is not straightforward (Figure 1). Thus, even if the nano-domain is best represented as a B-type structure, it is likely to be heavily distorted by the host structure. This may make it exceedingly difficult experimentally to evaluate the possibility of a B-type nano-domain. Therefore computer simulation studies of B-type defect clusters in GDC were conducted.

The incompatibility between B-type and fluorite structure posed some difficulties in the simulations. Defect clusters with monoclinic B-type symmetry must be inserted into the cubic fluorite ceria and lattice distortion must be simulated properly. A method was developed for these purposes and is introduced in detail in the next section.

1. Method to simulate large B-type defect clusters

Since there is a symmetry mismatch between the B-type (space group C2/m) and fluorite (Fm3m) structures, a B-type nano-domain would most likely be distorted from the perfect monoclinic, B-type structure. If viewing nano-domains as the result of defect clustering, the distortion would result from the following process: defects aggregate into a cluster of certain structural pattern; when the cluster grows large enough, it acquires B-type structural characteristics and distorts away from fluorite to monoclinic B-type; however, it can't fully transform to monoclinic because of the cubic fluorite environment, thus distortions of both nano-domains and host fluorite occur. Therefore, to adequately simulate distortions in the structure and further investigate energetically the possibility of B-type nano-domains, a reasonable approach is to distort the B-type structure, while maintaining its topology, to a cubic one, so that it could be inserted into the fluorite

structure. In this connection, a close structural relationship between the B-type and fluorite structures was discovered in this study. This relationship allowed us to properly distort the monoclinic B-type structure to a hypothetical “cubic B-type” structure. The structural coherence would then allow the modified, “cubic B-type” structure to relax back towards its original monoclinic structure following the insertion, as the host structure also relaxed to accommodate the nano-domain. This allowed us to adequately link clustered defects to the second phase, B-type structure.

The specific method used to create such a “cubic B-type” defect cluster is illustrated in Figure 7 and Figure 8. Firstly, a segment of the B-type structure (as shown in Figure 8[a]) was mapped to the fluorite structure of the perfect host lattice (CeO₂; as shown in Figure 8[b]). This resulted in gadolinia in the form of a modified fluorite structure. The ion coordinates were manually adjusted in an effort to match the B-type symmetry. The adjusted structure was then relaxed by means of a perfect lattice minimization. Ions were again adjusted according to the relaxation result and relaxed again. This process was repeated, iteratively, until a B-type structure was achieved (as shown in Figure 8[c]).

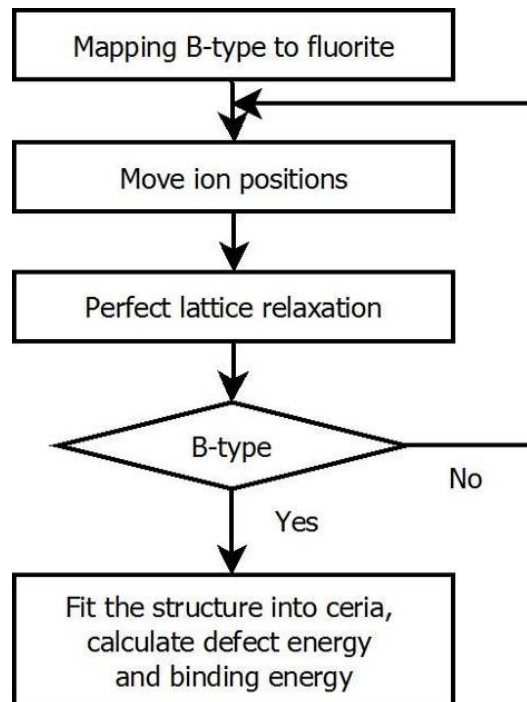


Figure 7. Flow chart of the simulation method.

The model “cubic B-type” structure, developed in this manner, bore all the structural and symmetrical characteristics of B-type and would relax back to B-type in an unimpeded environment. It could be directly fitted into the ceria lattice in an effort to examine the B-type nano-domain structure. As nano-domains serve as the precursor of phase separation, they can be viewed as large defect clusters with the structure of the second phase. Therefore to reflect the structural properties of the nano-domain, the minimum size of a defect cluster must contain at least a basic structural unit -- a unit cell. In this work, defect clusters of sizes from 1 to 4 unit cells were studied. The defect energy was compared with the sum of the individual defects, and the binding energies were calculated.

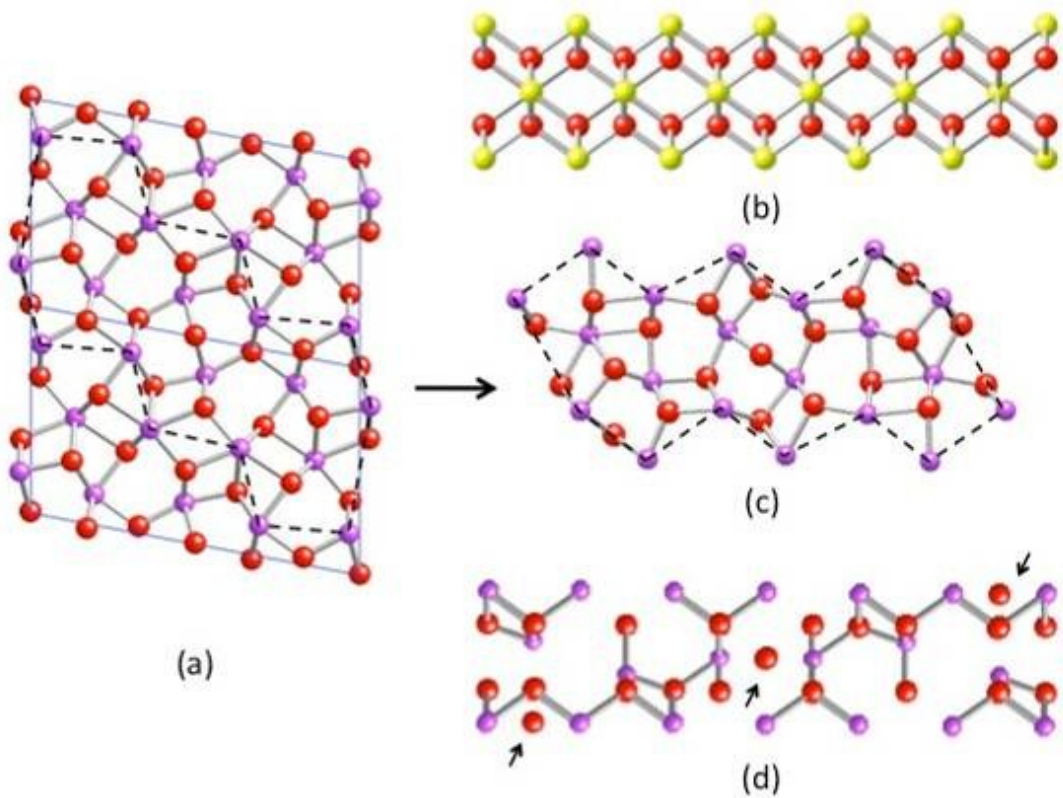


Figure 8. (a) B-type Gd_2O_3 viewed from $[010]$; (b) Fluorite CeO_2 viewed from $[110]$; (c) B-type Gd_2O_3 fragment which corresponds to the fluorite CeO_2 lattice unit in Figure 8[b]; (d) Model “cubic B-type” structure that can be fit into fluorite but will relax back back to the B-type lattice unit shown in Figure 8[c]. Arrows indicate interstitial oxygen ions.

2. Relationship between the B-type and fluorite structures

A one to one correspondence between the cations in B-type and fluorite was observed first, as shown in Figure 8[b & c]. The mirror plane of the C2/m, B-type structure corresponded to the fluorite (110) plane, and the two-fold axis was in the fluorite [110] direction. In other words, the B-type [010] direction corresponded well with the fluorite [110] direction except that the inter-plane distances were somewhat different (3.57 Å in the case of the B-type and 3.82 Å for the fluorite; see lattice parameters in Table 3). The main deviation of the B-type from fluorite occurred in the B-type (010) plane, relative to the corresponding (110) plane in fluorite. This can also be observed in Figure 8[b] and 3[c].

Unlike the cations, the correspondence between the oxygen ions in the structures was ambiguous. However, when building the model “cubic B-type” structure from fluorite structure, it was found that the oxygen ion positions, within the model “cubic B-type” structure, were critical to reacquiring a monoclinic B-type structure upon relaxation. As shown in Figure 8[d], relative to the fluorite anion positions illustrated in Figure 8[b], some of the oxygen ions within the model “cubic B-type” structure resided in interstitial positions (those marked within the figure). The model “cubic B-type” structure would not be able to relax into the monoclinic B-type unless oxygen ions were moved into those critical interstitial positions. On the other hand, for the cations, only slight perturbations from the equilibrium positions were necessary. The migration of oxygen ions to certain interstitial positions was clearly the dominant factor in insuring the transition of the model “cubic B-type” structure back to the monoclinic B-type. Accordingly, it seemed reasonable to suggest that oxygen ion diffusion might play a similar role in the phase transition between C-type (a cubic structure very close to fluorite) and B-type Gd_2O_3 . The transformation of the symmetry and structure from C-type to B-type could be accomplished through oxygen diffusion. However, considering the oxygen diffusion activation energy of 1.95 eV reported for C-type gadolinia,⁹ the energy barrier for oxygen ions to migrate into sites appropriate to the (lower temperature) B-type structure might be substantial. Indeed, the experimentally determined phase transition temperature was quite high (1200-1425 °C⁶⁻⁸). Equally significant here is that

the B-type structure could be easily preserved at low temperature because of the reduced oxygen mobility.^{7,10}

Relationships similar to that between the monoclinic B-type and cubic fluorite structure may exist in other material systems. A similar relationship was observed between cubic spinel MgAl_2O_4 and monoclinic θ -alumina.¹¹ Such a relationship could be critical in determining and stabilizing the structure of the technically important γ -alumina, which could be an intermediate meta-stable phase between MgAl_2O_4 and θ -alumina.

3. Defect calculations

The possibility of a B-type nano-domain structure could be examined by inserting some volume of the model “cubic B-type” structure developed in this thesis into the fluorite CeO_2 , as discussed in the method section. Note, when a unit cell is extracted from a structure, the translational symmetry is lost. Therefore nine single unit cell clusters with different atomic arrangements at the cell boundary were tested. Each single unit cell cluster contained 12 Gd'_{Ce} and 6 V_{O}'' , and was inserted into the ceria lattice. A maximum, i.e. least negative, binding energy of $-3.39\text{eV}/\text{V}_{\text{O}}''$ was found. The negative binding energy indicated that defect aggregation into such a structure was not energetically favorable.

Since larger defect clusters could preserve more structural characteristics, two adjacent unit cells (24 Gd'_{Ce} , 12 V_{O}'') as a single defect cluster were considered next. The most stable single unit cell cluster found in the earlier simulations was used to construct the larger clusters. The adjacent unit cells aligned along their [010] direction yielded a binding energy of $-3.37\text{eV}/\text{V}_{\text{O}}''$. This was almost the same as for a single unit cell cluster. Along this direction, there was not a significant difference between the B-type and fluorite structures (other than the inter-planar distance as mentioned previously), so this result was not surprising. However, when the two unit cells were aligned along the [001] direction, the binding energy decreased to $-4.68\text{eV}/\text{V}_{\text{O}}''$, which was even less favorable. As discussed earlier in association with Figure 8[a & b], the B-type structure, in its (010) plane, strongly deviated from the fluorite structure in its corresponding plane. When the unit cell was repeated about the (010) plane, its tendency to deform into the monoclinic structure became more pronounced. Therefore increasing cluster size along the [001]

direction gave a lower, less favorable, binding energy. This result indicated a high degree of incompatibility between the B-type and fluorite structures even though a close structural relationship existed between them. The resulting relaxed structures remained, in all cases, cubic. However, as indicated by the negative binding energies, no stable intermediate structure between the monoclinic, B-type and the cubic, fluorite structure was found.

We further tested the defect cluster binding energy to include four unit cells ($48 \text{ Gd}^{3+}_{\text{Ce}}, 24 \text{ V}_{\text{O}}^{\bullet\bullet}$) by extending a single unit cell along both the [010] and [001] directions. The result gave a binding energy of $+0.57 \text{ eV/V}_{\text{O}}^{\bullet\bullet}$. This suggested that larger B-type clusters could be stable as nano-domains. However, when inspecting the relaxed defect structure, it was found that it retained a cubic structure rather than reverting towards B-type. Figure 9 shows a single plane of the relaxed defect structure. The atomic positions making up the defect cluster did not deviate substantially from those of the fluorite host lattice. Thus this larger defect cluster of four B-type unit cells did not revert at all to the B-type structure. Interestingly enough, the arrangement of oxygen vacancies, shown in the left half of Figure 9, was the same as that of a cubic, C-type structure. It can be seen that, in the case of a nano-domain, an intrinsic cubic defect structure would cause less distortion when forming a coherent boundary with the host lattice. This is probably why, when the defect structure bore some characteristics of a C-type structure, a positive binding energy was observed. In fact, experiments have shown that 5 at. % cerium doping stabilizes gadolinia in a C-type structure instead of B-type up to $1600 \text{ }^{\circ}\text{C}$.⁷ This was much higher than the phase transition temperature for undoped gadolinia.⁶⁻⁸ C-type fragments were not observed in the smaller cluster calculations. This was probably owing to an insufficiency of defects to form such a structure and this resulted in a much lower binding energy.

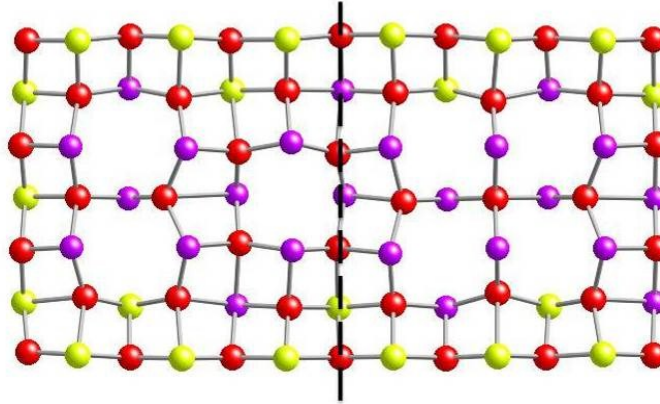


Figure 9. Single plane of a 4 unit cell defect cluster after relaxation, viewed from [001] direction. The arrangement of three oxygen vacancies on the left side bears characteristics of a C-type structure. Refer to the text for details of the structure on the right side.

There were still defect arrangements in the cluster, such as that shown in the right half of Figure 9, that were not C-type in character even though they had a cubic arrangement. A higher binding energy was certainly expected in the case of a completely C-type defect cluster. However, a complete transformation from a B-type defect cluster to C-type required oxygen mobility, as noted earlier. In this study, the static lattice simulations, using energy minimization, were employed; thus long range diffusion of the ions could not occur. As such, more conclusive statements will be possible only after C-type defect clusters are explicitly investigated. This is discussed later in this chapter. Nevertheless, these results suggested that a cubic structure, such as C-type, would be a more likely defect structure than a monoclinic B-type.

B. C-type rare earth structure and pyrochlore structure

C-type Gd_2O_3 and pyrochlore $\text{Gd}_2\text{Ce}_2\text{O}_7$ are cubic and both can be viewed as $2 \times 2 \times 2$ fluorite supercells (see Figure 10 and Figure 11). In C-type, all the cations in the supercell are Gd^{3+} , while in pyrochlore, half are Ce^{4+} . Corresponding numbers of oxygen vacancies arrange in the NNN positions of Gd^{3+} in pyrochlore. In C-type Gd_2O_3 , all the neighbors of vacancies are Gd^{3+} , apparently, because there is no Ce^{4+} . The simulations showed that the lattice parameters of both C-type and pyrochlore were close to that of ceria (simulated lattice parameters: C-type: 10.804 Å, pyrochlore: 10.967 Å, ceria supercell with same number of cations: 10.820 Å). Therefore, it was a straightforward

exercise to insert a single unit cell of the respective structures into the ceria host lattice as a defect cluster. Note that when separating one unit cell from an infinite lattice, the translational symmetry was lost, so there were a number of ways to build a “one unit cell” defect cluster. According to previous simulation experience, a defect cluster that preserves more structural symmetry usually yields a slightly higher binding energy. Among the “single pyrochlore unit cell” clusters tested in this study, the highest binding energy, $0.85 \text{ eV}/V_{\text{O}}^{\bullet}$, was found in the cluster shown in Figure 12 (a).

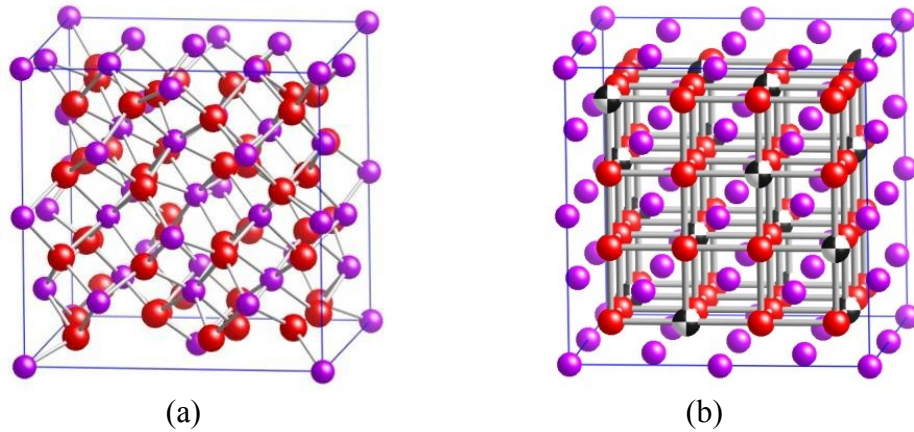


Figure 10. (a) C-type Gd_2O_3 structure (b) C-type Gd_2O_3 structure viewed as a defect fluorite structure. Beach balls indicate the position of oxygen vacancies.

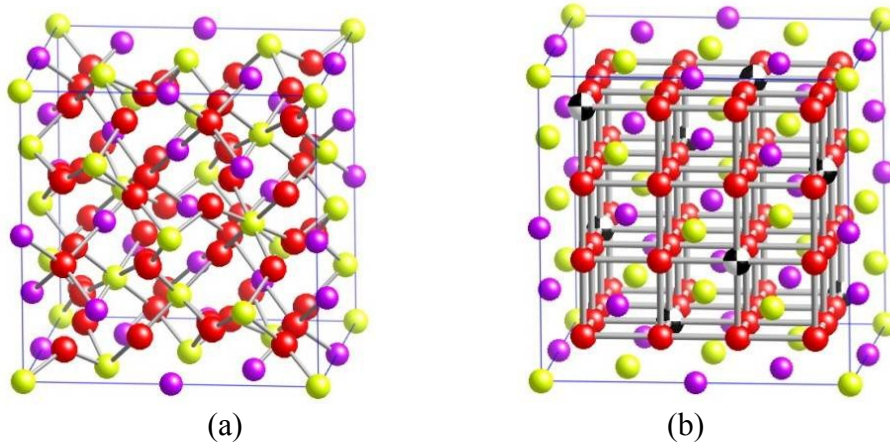


Figure 11. (a) pyrochlore $\text{Gd}_2\text{Ce}_2\text{O}_7$ structure (b) pyrochlore $\text{Gd}_2\text{Ce}_2\text{O}_7$ viewed as a defect fluorite structure. Beach balls indicate the position of oxygen vacancies.

One C-type unit cell, when viewed as derived from a fluorite structure, is comparable to the pyrochlore unit cell but contains twice the dopants and oxygen vacancies (Figure 10). When half of a C-type unit cell (Figure 12 (b)) was put into the ceria lattice, a binding energy of $0.84 \text{ eV}/V_{\text{o}}^{\bullet}$ was obtained. This was almost the same value as that obtained for a single pyrochlore unit cell. When an entire C-type unit cell was inserted into the ceria lattice, a substantial binding energy of $1.06 \text{ eV}/V_{\text{o}}^{\bullet}$ (Figure 12 (c)) was found. This binding energy was much higher than any of the defect clusters with the pyrochlore-type structure examined. This suggested that C-type was the preferred structure for a large, nano-sized defect cluster. The most recent study of nano-domain structures in GDC compared SAED patterns and patterns generated from simulations.¹² Results showed that SAED patterns agreed well with C-type related structures. Some discrepancies existed, which could be due to structural distortions caused by the host lattice that were not considered in the study, or intermediate defect structures between NNN, pyrochlore type structure and NN, C-type structure existing in small domains and boundary regions. The existence of such intermediate structures has yet to be studied because their sizes are too small to examine experimentally but too large to have all possible configurations simulated. Further investigations are required for this matter.

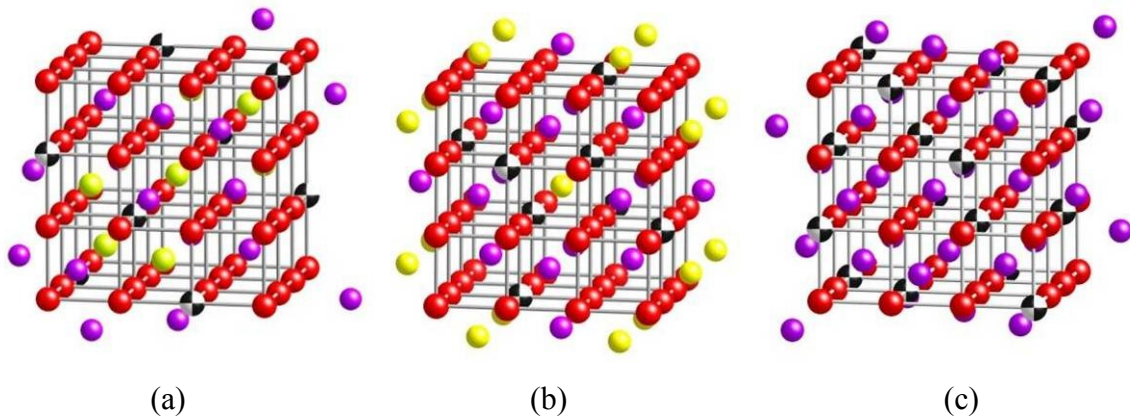


Figure 12. The most stable defect cluster among (a) one pyrochlore unit cell clusters (b) half C-type unit cell clusters (c) one C-type unit cell clusters studied in this work. Beach balls indicate the position of oxygen vacancies.

The less favorable binding energy for pyrochlore type defect structures, in addition to the absence of pyrochlore $\text{Gd}_2\text{Ce}_2\text{O}_7$ in experimental studies of the Gd_2O_3 -

CeO₂ system,^{7,13} led us to question its phase stability. For this reason, the formation energy of the pyrochlore structure was calculated so as to evaluate this stability. The formation energy was calculated according to the following formula:



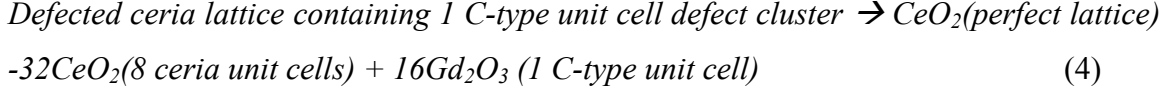
$$E_{formation} = E_{Gd_2Ce_2O_7} - E_{Gd_2O_3(C\text{-type})} - 2E_{CeO_2} \quad (3)$$

wherein the lattice energies were obtained from perfect static lattice calculations. The formation energy was therefore the difference between the lattice energy of the product relative to the lattice energy of the reactants. The formation energy per pyrochlore formula unit was determined to be +1.04 eV, indicating that pyrochlore Gd₂Ce₂O₇ was not as stable as a phase separation of C-type Gd₂O₃ and ceria. With the ability of GULP to perform free energy minimization,¹⁴ simulations of the pyrochlore, C-type, and ceria lattices at 300K and 1 atmosphere were also performed. The formation energy was still found to be positive (0.97 eV). This suggested that pyrochlore would not be stable even at room temperature. Evidently, when the defect cluster grew large enough to have a fully developed pyrochlore structure, the intrinsic instability of the structure would likely decrease the binding energy and make it less stable than clusters with a C-type structure.

In the defect clusters with the pyrochlore-like structure, the coordination number of dopants is 8; in a C-type cluster, it is 6 (in the center of the cluster) or 7 (at the boundary). When the clusters transform from pyrochlore-type to C-type, the average coordination number of the dopants would decrease to a value below that obtained from a random distribution. As C-type defect clusters have shown substantial binding energies, the oxygen vacancy mobility would be lowered. Both of these phenomena could be examined experimentally with material characterization techniques, which would allow for the estimation of the scale and predominant structure of defect clusters in GDC materials in practice.

C. Nano-domains and phase separation

It was natural to consider the relationship between nano-domains and phase separation, because they seemed to share the similar structure (C-type Gd_2O_3). To examine this question, a system composed of a single isolated nano-domain, represented by a C-type unit cell defect cluster, was compared to an idealized phase separated system composed of pure ceria and gadolinia in accordance with the following formula:



The systems on the left and right were composed of identical numbers of atoms. When the energies of the systems on both sides were the same (Equation 4), they became equally stable and the conditions indicated in Equation 5 were satisfied. This would represent an equilibrium between phases involved.

$$E_{\text{defect cluster}} + E_{\text{perfect lattice}} = E_{\text{perfect lattice}} - 8E_{\text{ceria unit cell}} + E_{\text{C-type unit cell}} \quad (5)$$

We used Equation 2 to calculate the binding energy of the defect cluster (left side) that satisfied the conditions given in Equation 5. Therefore, for the defect cluster to be equally stable with the phase separated system, its binding energy would need to be as high as:

$$E_{\text{binding}} = \sum E_{\text{isolated defects}} + 8E_{\text{ceria unit cell}} - E_{\text{C-type unit cell}} \quad (6)$$

The result was found to be 1.67 eV per oxygen vacancy. This meant that, unless the binding energy of the defect cluster was higher than this value, the idealized phase separated system was more energetically favorable. Considering the defect cluster data given in this chapter, it could be seen that even the highest binding energy obtained (1.06 eV for a “one C-type unit cell” defect cluster), was still considerably less stable than the ideal phase separated system. Note that the phase separated system considered in Equation 5 represents an idealized system and that the defect cluster separates into a

perfect host lattice and C-type unit cell with no distortion. In actual phase separation, however, interfaces are created. For a cluster of sub-10 nm scale, the interface energy is expected to be high due to the high interface-volume ratio; therefore, the coherent boundary of the nano-domain could very possibly prevent separation. But when the cluster becomes larger and the structural mismatch becomes substantial, it will be expected to lead to a phase separation of C-type Gd_2O_3 from the ceria host lattice. This result completes the picture of the defect association in GDC: defects form small clusters with NNN configuration; clusters grow larger and become nano-domains, wherein they acquire a complete secondary phase structure (C-type); the growth of nano-domains then leads to phase separation.

D. Domain size

From the previous discussion, it was clear that the size of the nano-domains had an effect on the structure and stability of the domains. However, the Mott-Littleton method required increasing the region I size of 25 Å with the size of the defect cluster considered, which led to a roughly cubic growth of the computational resources required. The sizes of single unit cell clusters studied earlier had all exceeded 1 nm, and a region I size which including around 10,000 atom cores and shells has been adopted to accommodate the clusters. Further increasing the cluster size using the Mott-Littleton method is then impractical: for example, region I size to simulate a cluster of 2 nm in diameter would preferably include 80,000 atom cores and shells. Therefore, to investigate larger size nano-domains, ceria supercells that contained defect clusters and used periodic boundary conditions were built to simulate nano-domains inside the host lattice. The method used to construct these supercells is illustrated in Figure 13.

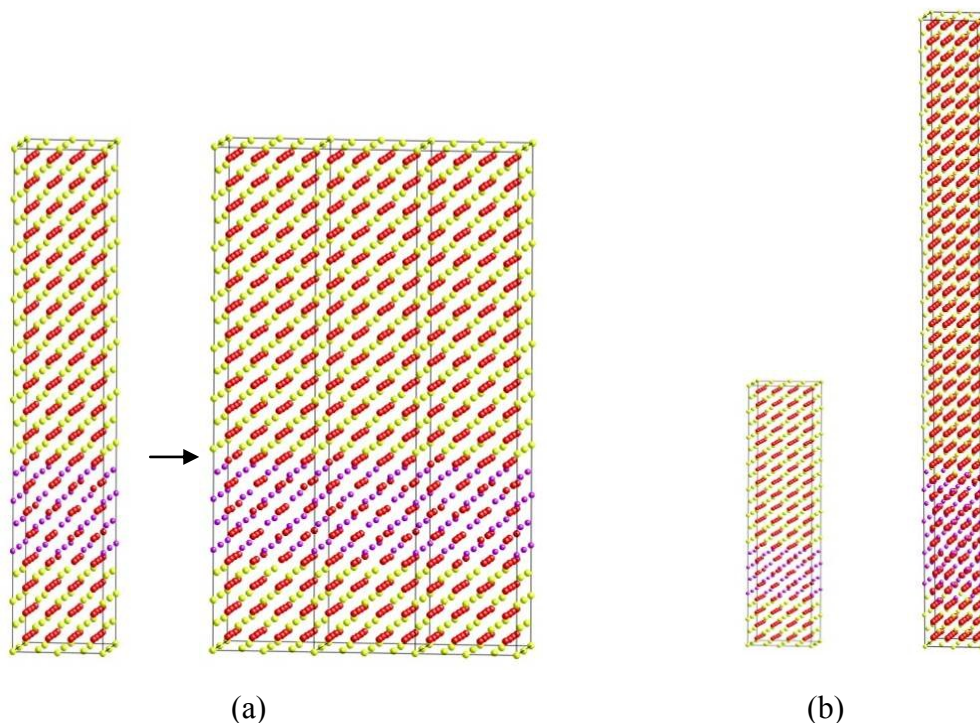


Figure 13. Illustration of the method of building supercells with a nano-domain structure. (a) a basic supercell containing one C-type unit cell as a defect cluster and the structure after the application of periodical boundary conditions. (b) an illustration of varying domain sizes while keeping the defect concentration constant.

Each supercell was a column of several ceria unit cells with one or more unit cells replaced by that of a secondary phase (C-type or pyrochlore). Under periodic boundary conditions, the defect cells became a layer of defect structure. This was a reasonable representation of a nano-domain structure along a single dimension, and helped to investigate the effects of the interface between the host lattice and the domain. The ratio of the dopants versus cerium cations was kept at 10% and 20% in this study. Supercells with varying defect layer thicknesses were constructed and input into GULP to perform a static lattice optimization. The binding energy was calculated by comparing the optimized supercell energy with the perfect ceria lattice. The results are shown in Figure 14.

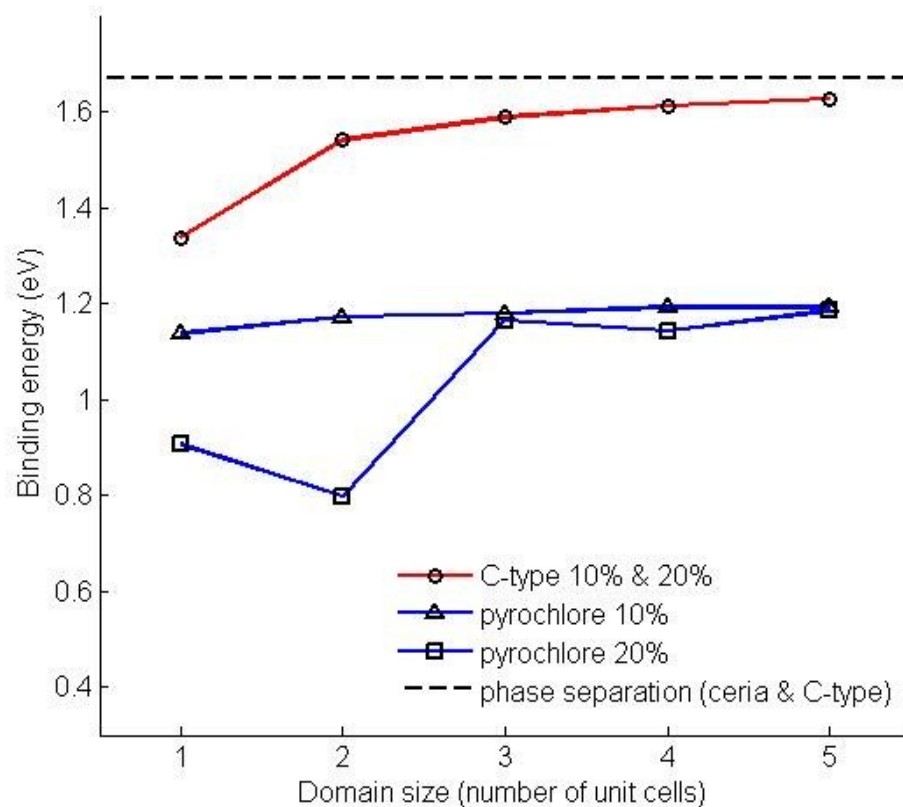


Figure 14. Binding energy per oxygen vacancy versus domain size obtained from the simulations of defect supercells. Using the size of the ceria lattice being replaced by the defect unit cells, one unit cell on the x-axis has a dimension of 1.082 nm. The actual size of the defect unit cells varied slightly after the relaxation.

It can be seen from the results:

When the domain size exceeded 2 unit cells (about 2nm), nano-domains with C-type structure had a significantly higher binding energy than those with pyrochlore structure (at around 1.6 eV, compared to the 1.2 eV binding energy of pyrochlore type nano-domains). Domains with C-type structure were thus more stable than those with pyrochlore structure, which agreed with the earlier observations that the C-type was more likely to be the nano-domain structure. The formation of tightly bonded C-type nano-domains would result in higher activation energy for the vacancy diffusion as the additional binding energy must be overcome, therefore decreased the oxygen mobility more seriously, relative to the formation of pyrochlore-type clusters.

The binding energy increased with the size of the domain, which confirmed the earlier result from small defect clusters, that the domains tended to grow larger. When looking at the optimized supercell structure, it was found that large distortions of the atomic positions from the perfect lattice occurred only within the first 1 nm from the interface (Figure 15). Therefore when the domain size was smaller than two unit cells, the distortion inside the domain caused by the host lattice became too high, and this significantly decreased the binding energy. Since the ceria host lattice had a stabilizing effect on the pyrochlore-type structure, the binding energy of the 10% pyrochlore type domain did not decrease as much. Therefore it could be extrapolated, hypothetically, to suggest that when the defect concentration was low and the cluster size was smaller than 1 unit cell, a pyrochlore-like structure would be more preferred. This also agreed with the earlier conclusion.

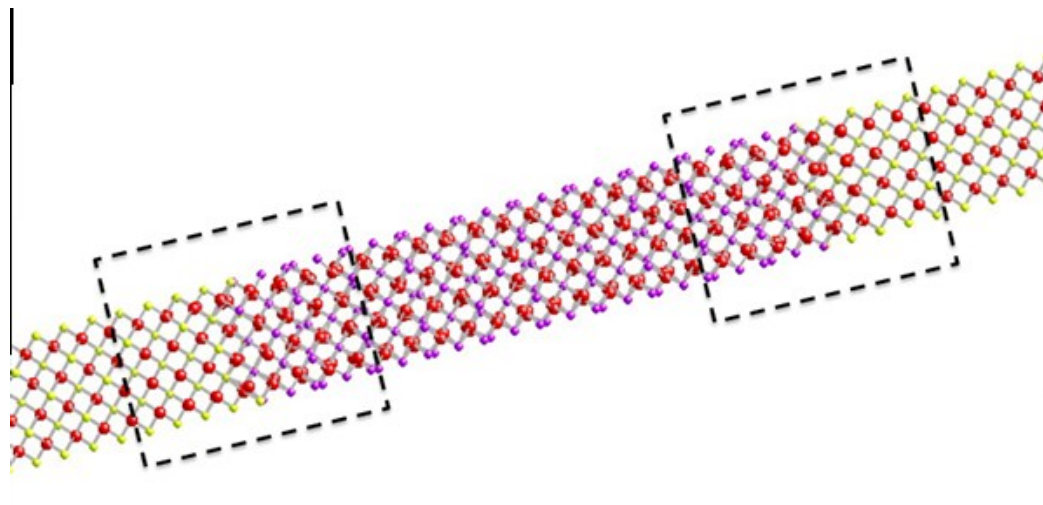


Figure 15. Illustration of the highly distorted regions in a relaxed defected supercell.

For C-type domains, the binding energy showed a very small decrease from 10% to 20% concentration. This decrease was, however, so small that it could not be represented by the scale required of Figure 14. The slight difference observed was caused by the elastic strain resulting from the mismatch between the lattice parameters of C-type structure and ceria. Pyrochlore-type domains also showed a small difference in binding energy between 10% and 20% concentration, at the higher domain sizes, which might also result from elastic strain. Because the dopant concentration in a pyrochlore-type domain was half of that of the C-type domain, the separation between pyrochlore domains was also half of that existing between C-type domains. Therefore, the separation between two domain layers was smaller, resulting in substantial lattice distortion and a significant decrease in binding energy for small size pyrochlore domains at a 20% concentration. Thus, for pyrochlore to be stable it would require smaller domain sizes. However, smaller domain sizes led to smaller inter-domain separation, particularly as the concentration increased and, from these results, such a condition would not be favorable owing to low binding energy. Therefore, the formation of C-type domains would be much more likely at higher concentration.

From the above analysis, it can be seen that the defect energy (the energetic difference between a defect structure and a perfect structure) of the nano-domain is mainly caused by two factors: structural incompatibility at the interfaces, and the elastic mismatch in the lattice parameters/volume. Both of these factors will increase the energy

of the defect lattice above the idealized phase separated system discussed in the last section (also shown in Figure 14 as a dashed line). However, for C-type domains, the defect energy contributed by these two factors can be very small. The lattice parameter mismatch between C-type and ceria is minimal. Additionally, the boundary distortion averaged by the number of defects becomes smaller when the domain size becomes larger. This can be confirmed in Figure 14 where the binding energies of C-type domains are shown to approach the energy required for a phase separation with increasing domain size. Considering the relationship between the nano-domain and phase separation discussed in Chapter 4C, C-type domains are expected to be commonly found in GDC with high doping concentrations in the absence of phase separation.

We have found that the elastic mismatch between the host lattice and the nano-domain has an effect upon the lattice parameter. From supercell simulations at a concentration of 20%, C-type nano-domains with the size of 5 unit cells decreased the ceria lattice parameter from 5.410 Å to 5.409 Å, while the pyrochlore nano-domain with the same size increased it to 5.425 Å. Actually, even the smallest sizes of defect structure considered within this work, whether pyrochlore-type (NNN) or C-type (NN), had a similar effect upon the lattice parameter.

We have shown that only small pyrochlore-type defect clusters might exist and that their binding energies are considerably lower than C-type nano-domains. Therefore the conductivity of GDC would then be benefited by the formation of pyrochlore-type clusters owing to the reduced binding energy. From the above results, it can be seen that the lattice parameter of GDC can be used to evaluate the general defect cluster structure that predominates within physical samples, which is otherwise difficult to determine experimentally owing to the small size of the defect clusters. If the lattice parameter is larger than that of pure ceria, dispersed small pyrochlore-type clusters are the most likely structure formed; however, if the lattice parameter is smaller than that of pure ceria, it is expected that C-type nano-domains have begun to form predominantly.

Note that the lattice parameter of GDC would also be affected by the nonstoichiometry. The nonstoichiometry is caused by the reduction of Ce^{4+} to Ce^{3+} , which can be viewed as doping Ce^{3+} into ceria. Ce^{3+} has a larger ion radius than Gd^{3+} , therefore oxygen vacancies created during reduction would prefer next nearest neighbor

sites of Ce^{3+} . This would be accompanied by a lattice expansion, which has been reported in the literature.^{15,16} However, the relationship between the level of nonstoichiometry and Gd^{3+} doping concentrations is rather obscure. Since the reduction of Ce requires creating oxygen vacancies, the enhancement of oxygen conductivity by doping Gd^{3+} would facilitate the bulk reducibility. Also, doping Gd^{3+} , if not forming domain structure, causes lattice expansion, which makes the lattice more accommodating to the large size of Ce^{3+} . Some previous studies have suggested that the reduction energy of Ce decreases with increasing doping concentration.¹⁵⁻¹⁷ However, there also have been experiments showing the opposite, that Gd^{3+} doping inhibits the Ce reduction.^{18,19} GDC with high doping concentration (≥ 20 at. %) were investigated in these studies, where nano-domain formations were very likely. Domain formation would cause lattice contraction which is no longer accommodating to Ce^{3+} . Decreasing oxygen conductivity caused by domain formations may also affect the reducibility, although further researches must be done before conclusions can be drawn. Additionally, there have been reports of segregation of Gd^{3+} dopants at surfaces and grain boundaries.^{19,20} This could be a result of defect association responding to the high oxygen vacancy concentration at surfaces and grain boundaries, and it would have the same effect on Ce reduction as nano-domains in bulk GDC. Under such considerations, the relationship between the lattice parameter and nano-domain formation in GDC is expected to hold even when the Ce reduction is taken into considerations. However, it can be seen that the Ce reduction in doped ceria is a kinetically driven phenomenon and would be closely related to defect associations discussed in this work. Indeed, experiments have shown that properties of GDC related to the Ce reduction and defect associations are tunable upon thermochemical conditioning.²¹ Ce reduction and related phenomena in GDC are certainly important issues that warrant more detailed investigations. Base on the simulation results in this thesis, it is suggested that defect associations should always be kept in mind in further studies.

From an energetic standpoint, defects in GDC always tend to form larger nano-domains, but the size of domains in real material can be greatly limited by the cation diffusion rate and the doping concentration. Let us consider a GDC sample with a homogeneous doping concentration of C in mole percent that goes through an equilibration process (for example, annealing) in which the mean diffusion distance for

cations is M . Let us also take account of the fact that 32 gadolinium cations exist within the C-type unit cell and that 4 cations exist in that of ceria. Assuming that all the cations in a cubic region of dimension M will form one C-type nano-domain, the size of the nano-domain, n (in number of C-type unit cells contained in the domain), can be estimated according to following equation:

$$4C \frac{M^3}{l^3} = 32n \quad (7)$$

where l is the lattice parameter of the GDC sample. It can be seen that the size of the nano-domain increases with both doping concentration and cation mobility (resulting in a larger value for M). In other words, doping concentration and cation diffusion limit the possible size of nano-domains. Earlier results from this chapter showed that the C-type domain size needed to be larger than 1 or 2 unit cells in order to be substantially more stable than small pyrochlore-type defect clusters. The defect associations in GDC can now be related to the doping concentration: under constant experimental conditions, small dispersed pyrochlore-type clusters will form at low concentration; the average cluster size increases with the concentration and nano-domains begin to form when concentration is high enough to permit the growth of large clusters with a fully developed C-type structure. This transition will result in the average coordination number of the dopants dropping from 8 to 6~7 with increasing doping concentration. Also the lattice parameter will be expected to first increase (with development of pyrochlore-type defect clusters) then begin to decrease once C-type nano-domains begin to form. However, the defect clustering and nano-domain formation can be highly affected by the sample synthesis conditions; therefore, there is expected to exist a wide range of material properties reported in the literature, such as the lattice parameter and conductivity, depending on the actual synthesis procedure used.

The formation of nano-domains at high dopant concentration is detrimental to the oxygen conductivity, because the high concentration of the oxygen vacancies would be offset by the fact that the most of the vacancies would be trapped in the nano-domains by the high binding energies. Therefore the formation of nano-domains should always be minimized for highly conductive GDC electrolytes. Besides lowering dopant

concentration, the formation of nano-domains can be limited by controlling the cation diffusion to keep the material from reaching equilibrium. Experimentally, the formation of nano-domains can be envisioned to occur and be controlled mainly by means of three processes:

1. The incomplete synthesis of GDC. The synthesis is usually considered complete when there is no trace of a secondary phase. However, nano-domains can be easily formed from gadolinia during synthesis. Therefore the synthesis and sintering temperature must be high enough to overcome the nano-domain binding energy and disperse the dopant. Nano-scale powders, and low temperature synthesis will also help to keep dopants from forming nano-domains.

2. Slow cooling rate. Even if the sintering temperature is high enough to fully disperse the dopants, a slow cooling rate will allow the system access to the lower energy states associated with nano-domains. The simulations have suggested that nano-domain formation is energetically favorable at high doping concentrations. Domains will form unless a non-equilibrium state can be maintained. Therefore a sufficiently rapid cooling rate is desirable for limiting the formation of nano-domains.

3. Cation diffusion during operation of the fuel cell. Nano-domains can form at a slow rate through sluggish cation diffusion during the operation, and a gradual decrease of the conductivity will be accompanied with the segregation process. GDC is aimed for the intermediate temperature range of operation below 750 °C.²² According to the tracer diffusion study studies, the Zr^{4+} diffusivity in scandia doped zirconia electrolyte at 750 °C would be below 10-20 cm^2/s^{-1} ,²³ and it is expected that the cation diffusion rate in GDC to be of a similar magnitude. Therefore, a low operation temperature could be very helpful to limit the rate of the run-time nano-domain formation.

The first two situations can be controlled relatively easily to minimize the nano-domain formation during the material process. The runtime degradation, however, is much more difficult to avoid. One possibility to control the runtime nano-domain formation may exist through “strain engineering”, utilizing the mismatch between the domain structure and host lattice. It is believed that similar problems exist in other rare earth doped fluorite structured electrolytes and the nano-domain forming mechanisms in GDC may also apply to these electrolytes. For instance, high-resolution ^{89}Y magic-angle-

spinning nuclear magnetic resonance has shown that in microcrystalline yttria doped ceria, Y sites with only Ce next-nearest neighbors began to decrease rapidly beyond 10% doping concentration, and the conductivity mimicked the same trend.²⁴ This observation can be explained by large-scale clustering of Y^{3+} dopants at high doping concentration. Experimental and simulation studies have all pointed to the conclusion that large scale defect clustering in highly doped electrolytes would be a major factor limiting the electrolyte conductivity. Therefore, when engineering the electrolytes, the defect association and nano-domain formation should be kept in mind to maximize the electrolyte performance.

E. Conclusions

In this chapter, nano-domain structures and their stability were studied with classic atomistic computer simulations. Defect clusters with possible secondary structures, including B-type, pyrochlore and C-type, were studied. Simulations of nano sized defect clusters that contained unit cells of a secondary phase indicated that C-type clusters had much higher binding energy (1.06 eV per vacancy) than that of pyrochlore-type clusters (0.85 eV per vacancy). This suggested that the nano-domain structure is more likely to be C-type rather than pyrochlore. Further simulations indicated that the formation energy of the pyrochlore structure was 0.97eV per formula unit at room temperature and standard pressure as shown in Equation (3). This suggested that pyrochlore was not a stable phase in the Gd-Ce phase system. Thus, it can be determined that only small pyrochlore-type defect clusters were energetically favorable with the help of the stabilizing effect of the ceria host lattice.

Simulations of defect supercells showed that the C-type nano-domains also had a tendency to grow larger. The binding energy increased with the size of the domain, but it was never high enough to be more stable than an idealized phase separation into perfect ceria and C-type gadolinia (in which no surface energy is considered). Nano-domains can therefore be viewed as a precursor for phase separation. Compared with an actual phase separated system, the coherent boundary of the nano-domains eliminates surface energy but results in extra elastic energy caused by the lattice parameter/volume mismatch and local lattice distortions at the boundary due to the structural incompatibility. Because of

the high compatibility between the C-type and ceria lattice, the difference in energy between the C-type nano-domain in GDC and the phase separated system remains small over a wide range of domain sizes. Therefore, C-type nano-domains can be easily formed in GDC.

The doping concentration is one of the two major factors that limit the size of nano-domains. Therefore, at low concentration, small pyrochlore-type defect clusters are expected while at high concentration C-type nano-domains are likely to be formed. Experimentally, the average coordination number of the dopants would drop from 8 to 6~7 with increasing dopant concentration. The lattice parameter is expected to show first an increase, then a decrease with doping concentration, and this can be used as an indication of the predominant defect cluster type present. Since C-type nano-domains have considerably larger binding energy than the small pyrochlore-type clusters, the conductivity of GDC is expected to follow the same trend as the lattice parameter. The other major factor limiting the nano-domain size is cation mobility. As a result, the experimental observations of these properties of GDC will be significantly dependent upon the actual material synthesis conditions.

Similar electrolyte systems could equally suffer from nano-domain formation. To enhance the electrolyte performance, nano-domain formation should be limited during synthesis and operation. Besides limiting doping concentration, using an appropriate method to keep the material from reaching an equilibrium state would help to minimize the nano-domain formation.

References

1. T. Mori and J. Drennan, "Influence of Microstructure on Oxide Ionic Conductivity in Doped CeO₂ Electrolytes," *J. Electroceram.*, **17** [2] 749-57 (2006).
2. F. Ye, T. Mori, D. R. Ou, J. Zou, G. Auchterlonie, and J. Drennan, "Compositional and Structural Characteristics of Nano-Sized Domains in Gadolinium-Doped Ceria," *Solid State Ionics*, **179** [21-26] 827-31 (2008).
3. W. Chen and A. Navrotsky, "Thermochemical Study of Trivalent-Doped Ceria Systems: CeO₂-MO_{1.5} (M = La, Gd, and Y)," *J. Mater. Res.*, **21** [12] 3242-51 (2006).

4. G.-y. Adachi and N. Imanaka, "The Binary Rare Earth Oxides," *Chem. Rev.*, **98** [4] 1479 (1998).
5. T. Mori, "Influence of Nano-Structural Feature on Electrolytic Properties of Gd Doped CeO₂ Solid Electrolytes," *J. Ceram. Soc. Jpn.*, **112** [1305] S642 (2004).
6. H. R. Hoekstra, "Phase Relationships in the Rare Earth Sesquioxides at High Pressure," *Inorg. Chem.*, **5** [5] 754-7 (1966).
7. V. Grover and A. K. Tyagi, "Phase Relations, Lattice Thermal Expansion in CeO₂-Gd₂O₃ System, and Stabilization of Cubic Gadolinia," *Mater. Res. Bull.*, **39** [6] 859-66 (2004).
8. M. Zinkevich, "Thermodynamics of Rare Earth Sesquioxides," *Prog. Mater. Sci.*, **52** [4] 597-647 (2007).
9. D. B. Basler and M. F. Berard, "Measurement of Oxygen Diffusion in Dy₂O₃ and Gd₂O₃ by Studying High-Temperature Oxidation of the Metals," *J. Am. Ceram. Soc.*, **57** [10] 447-9 (1974).
10. S. Stecurra, "Crystallographic Modifications and Kinetics of Phase Transformations of La₂O₃, Nd₂O₃, Sm₂O₃, Eu₂O₃ and Gd₂O₃"; Ph.D. Thesis. Georgetown University, Washington, D. C., 1965.
11. B. Wang, M. Hall, and A. N. Cormack, "Unpublished Results,"
12. F. Ye, T. Mori, D. R. Ou, J. Zou, and J. Drennan, "A Structure Model of Nano-Sized Domain in Gd-Doped Ceria," *Solid State Ionics*, **180** [26-27] 1414-20 (2009).
13. K. E. Sickafus, L. Minervini, R. W. Grimes, J. A. Valdez, M. Ishimaru, F. Li, K. J. McClellan, and T. Hartmann, "Radiation Tolerance of Complex Oxides," *Science*, **289** [5480] 748-51 (2000).
14. J. D. Gale, "Analytical Free Energy Minimization of Silica Polymorphs," *J. Phys. Chem. B*, **102** [28] 5423-31 (1998).
15. B. C. H. Steele, K. M. Hori, and S. Uchino, "Kinetic Parameters Influencing the Performance of IT-SOFC Composite Electrodes," *Solid State Ionics*, **135** [1-4] 445-50 (2000).
16. G. Balducci, M. S. Islam, J. Kašpar, P. Fornasiero, and M. Graziani, "Reduction Process in CeO₂-MO and CeO₂-M₂O₃ Mixed Oxides: A Computer Simulation Study," *Chem. Mater.*, **15** [20] 3781-5 (2003).

17. E. Ruiz-Trejo and J. Maier, "Electronic Transport in Single Crystals of Gd-Doped Ceria," *J. Electrochem. Soc.*, **154** [6] B583-B7 (2007).
18. S. Zhao and R. J. Gorte, "The Effect of Oxide Dopants in Ceria on N-Butane Oxidation," *Appl. Catal., A*, **248** [1-2] 9-18 (2003).
19. H. Borchert, Y. Borchert, V. V. Kaichev, I. P. Prosvirin, G. M. Alikina, A. I. Lukashevich, V. I. Zaikovskii, E. M. Moroz, E. A. Paukshtis, V. I. Bukhtiyarov, and V. A. Sadykov, "Nanostructured, Gd-Doped Ceria Promoted by Pt or Pd: Investigation of the Electronic and Surface Structures and Relations to Chemical Properties," *J. Phys. Chem. B*, **109** [43] 20077-86 (2005).
20. H. Hong, M. G. Turgut, S. Yuji, and P. Fritz, "High Ionic Conductivity in Ultrathin Nanocrystalline Gadolinia-Doped Ceria Films," *Appl. Phys. Lett.*, **89** [14] 143107 (2006).
21. A. Karthikeyan, M. Tsuchiya, C.-L. Chang, and S. Ramanathan, "Tunable Electrical Conductivity in Nanoscale Gd-Doped Ceria Thin Films," *Appl. Phys. Lett.*, **90** [26] 263108-3 (2007).
22. B. C. H. Steele and A. Heinzl, "Materials for Fuel-Cell Technologies," *Nature*, **414** [6861] 345-52 (2001).
23. M. A. Taylor, M. Kilo, G. Borchardt, S. Weber, and H. Scherrer, "⁹⁶Zr Diffusion in Polycrystalline Scandia Stabilized Zirconia," *J. Eur. Ceram. Soc.*, **25** [9] 1591-5 (2005).
24. P. Jain, H. J. Avila-Paredes, C. Gapuz, S. Sen, and S. Kim, "High-Resolution ⁸⁹Y and ⁴⁵Sc Nmr Spectroscopic Study of Short-Range Structural Order in Nanocrystalline Y- and Sc-Doped CeO₂ and ZrO₂," *J. Phys. Chem. C*, **113** [16] 6553-60 (2009).

CHAPTER 5. STRAIN MODULATION OF DEFECT STRUCTURE IN GDC

In previous chapters, it was shown that nano-domains in GDC were nano-sized defect clusters with structures related to C-type rare earth oxide, serving as precursors to phase separation. It was also suggested that defect segregation was energetically favorable at high-doping concentration and would cause performance deterioration in applications where GDC was used as fast ion conductor. These understandings now enable us to investigate possible methods to minimize the domain formation and enhance material properties.

Although nano-domain formation is energetically favorable in GDC, non-equilibrium processing methods can be used in material preparation, to limit the domain growth. Methods such as using finer particle sizes, low-temperature synthesis, rapid cooling after sintering and so on, might be utilized to disperse dopants and prevent domain formation in the first place (see Chapter 4D). However, as ion conductors typically operate at high temperatures (500~1000 °C),¹ defect segregation during operation is difficult to prevent and would cause performance degradation. Simulations in previous chapters suggested that small clusters and nano-domains preferred different structures. Small defect clusters were found to prefer next nearest neighbor (NNN) type configurations that can be viewed as pyrochlore structural fragments. On the other hand, for large defect clusters and nano-domains, structures based on NN type configurations and related to C-type rare earth oxide structures became more favorable. Therefore, limiting nano-domain formation could be enhanced if the defect structures could be engineered to NNN type configurations. It was found that these two types of associations were linked with the lattice volume. NNN configurations caused lattice expansion, while NN configurations led to lattice contraction. (see Chapter 4D) Conversely, appropriately straining the structure might be able to switch the preferred defect structure. This would potentially provide a way to control the nano or sub-nano level defect structure via macroscopic strain, and became the subject of this chapter.

An additional benefit of studying the effect of strain on the defect structure is that it may provide insight on some interesting properties that have been observed in GDC.

For instance, the so called “chemical stress/strain” phenomenon has received some attention in recent years as it may lead to novel applications.²⁻⁴ The phenomenon is characterized by non-linear, hysteresis type, stress-strain relationships. An example is the experiment reported by Kossoy et al.:³ A thick $\text{Ce}_{0.8}\text{Gd}_{0.2}\text{O}_{1.9}$ film was deposited onto a silicon substrate. A square window was created on the substrate by etching so that the edges of the window were tethered to the GDC film. Upon fast heating to 40~100 °C, the GDC film would buckle due to the mismatch in the thermal expansion coefficients between the film and the substrate; but after annealing for 3~30 minutes, the buckling would disappear. This indicates that GDC responded to compressive stress/strain with inelastic volume contraction. The contraction was estimated to be around 0.038%. Furthermore, slow cooling could return the film to the state before the experiment, and the whole process was repeatable. The flattening process was associated with a characteristic time which was dependent on temperature. Analyses of similar effects with self-supported GDC films gave an activation energy of 1.1eV. It was believed such phenomena are related to the association between dopants and vacancies.^{5,6} However, a fundamental understanding is still lacking. In this chapter, by simulating how the defect structures in GDC respond to mechanical strain, a possible mechanism to explain such behavior is³ proposed.

A. Strain effect on basic defect pairs

To understand the strain effect on defect structures in GDC, the basic building blocks, simple $\text{Gd}'_{\text{Ce}}\text{-V}_{\text{O}}''$ defect pairs, were simulated first. Three basic structures, nearest neighbor (NN), next nearest neighbor (NNN) and the third nearest neighbor (3NN) pairs, were incorporated into the CeO_2 structure, with lattice parameters scaled to match a range of applied strains (-0.05%, -0.04%, -0.03%, -0.02%, -0.01%, 0.00%, 0.01%, 0.02%, 0.03%). Calculated defect energies are shown in Figure 16. The sums of the defect energies of isolated Gd'_{Ce} and V_{O}'' under strains were also calculated and shown in the figure for comparison. The defect energy was calculated as the energy difference between structure with defects and the perfect (defect-free) lattice. Because the energies of both the perfect lattice and the structure with defects were parabolic functions of strain around 0% strain (Hooke’s law), the defect energy would be either a linear (if

the two systems have the same elastic constant), or a parabolic (different elastic constants) function of strain.

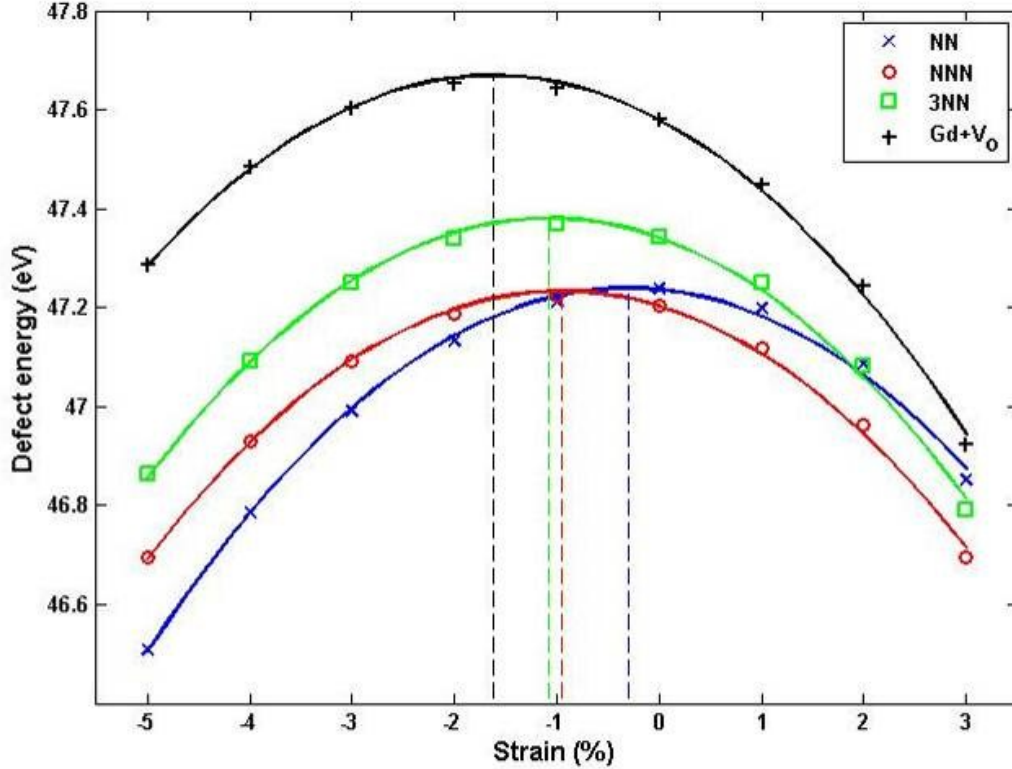


Figure 16. Defect energies of NN, NNN, and 3NN type $Gd'_{Ce}-V_{O}''$ pairs, as well as isolated defects, versus lattice strains. Parabolic fit to the data points are shown in solid lines. Dashed lines indicate maxima of the parabolic functions.

From Figure 16 it can be seen that the relationships between defect energy and strain for all the configurations could be well described by parabolic functions, which indicated that creating these defects pairs changes the elastic constant of the perfect lattice, as discussed above. The change in elastic constant was also not dependent on the association between Gd'_{Ce} and V_{O}'' , because all the curves had the same shape (same second order coefficient of -0.033 eV). However, all the maxima of the parabolic functions were shifted toward negative strain, indicating a change in the free volume caused by the defects, which did depend on the association between defects. The maximum of the function occurred at strains of -0.305% for NN, -0.959% for NNN, -1.077% for 3NN and -1.628% for isolated defects. The derivative of the function gave the

additional pressure required to create the strain because of the defects, compared to the perfect (defect-free) lattice. At 0% strain, derivatives of all the curves were negative, suggesting that compressive pressures were needed for all these structures with defects to maintain the defect-free lattice parameter. In other words, all of these defect pairs caused lattice expansion. The value of the derivative at 0% strain, which translated to the distance between the maximum and the zero strain for a parabolic function, corresponded to the degree of lattice expansion: isolated defects > 3NN > NNN > NN. As the dopant and vacancy moved apart and became less associated, the volume expansion became greater.

Because of the different volume expansions associated with the defect pairs, which was the most stable pair became a function of the strain. Under strain-free conditions, the NNN type configuration was found to be energetically favorable – the energy required to create a NNN defect association was smaller than that was needed to create a NN association. This agreed with previous studies.^{7,8} What is more interesting was that under compressive strain, this preference was reversed and the NN configuration became more stable. When the strain was -0.786%, the NN and NNN configuration were equally stable. The 3NN configuration and isolated defects were less stable than both NN and NNN over most of the strain range. In fact, the chance of a dopant with its nearest vacancy at the 3NN positions or beyond is fairly low in GDC. In 20% GDC, for instance, the probability of a given anion site being occupied by oxygen vacancy is 10% (equal to the concentration of oxygen vacancy). A cation site in GDC has 4 NN and 24 NNN oxygen positions. Therefore the chance of a given Gd^{3+} dopant having no vacancy as its NN or NNN is only $(90\%)^8 \times (90\%)^{24} = 3.4\%$. In view of the low occurrence and stability of 3NN configurations, NN and NNN configurations became the focus of this study.

The above results suggested that the strain condition in GDC material could alter the energetically favorable defect structure. This has several consequences. First, GDC materials prepared under different strain conditions would have different defect structures, and consequently different properties, especially in the activation energy of oxygen conduction. Second, compressive strain may promote nano-domain formations. The previous chapter suggested that large defect clusters and nano-domains in GDC had a C-type rare earth structure which was associated with NN type defect associations.

Clusters with NNN type configuration, on the other hand, were difficult to grow into nano-size because of the instability of the associated pyrochlore structure under normal conditions. Here the formation energy of the pyrochlore $\text{Gd}_2\text{Ce}_2\text{O}_7$ phase under tensile strain was further calculated with the same method. Even under 1.02% tensile strain, the formation energy was still positive (1.001 eV per formula unit), suggesting that pyrochlore remained unstable under tensile strain. Therefore, GDC prepared under tensile strain was expected to have fewer defect clusters and nano-domains. Finally, it is interesting to see that a change in strain can switch the preferred defect association type between NN and NNN. It might be possible to actively modulate the defect structure with strain, which in turn would potentially serve as a method to control the defect clustering during the operations of GDC ion conductors. Also, such a mechanism may also explain the abnormality in the stress-strain relationship that has been observed in GDC, as discussed at the beginning of Chapter 5. Of course, structural changes require oxygen or cation diffusion and an elevated temperature is necessary. In the following section, strain modulation of defect structure with the help of oxygen diffusion is simulated and discussed.

B. Strain modulation of the defect structure in GDC

To investigate how the defect structure in GDC responds to the strain condition, molecular dynamics simulations were carried out. The procedure was as following: First, a supercell of the perfect ceria structure, consisting of $6\times 6\times 6$ unit cells, was constructed. Then, 20% of the Ce^{4+} cations (174) in this supercell were randomly selected and replaced with Gd^{3+} dopants. A corresponding number of oxygen vacancies (87) were created at the same time by randomly removing oxygen ions from the supercell. For statistical purposes, this procedure was repeated three times so that three “samples” with different, randomly generated, defect structures were obtained. The GDC samples created this way were subsequently annealed for 500 ps at a temperature of 800K and pressure of 1 atm. A snapshot of the structure was taken every 2 ps. Each snapshot structure was relaxed by DL_POLY using the conjugate gradient structure optimization method,⁹ and the energy was then examined.

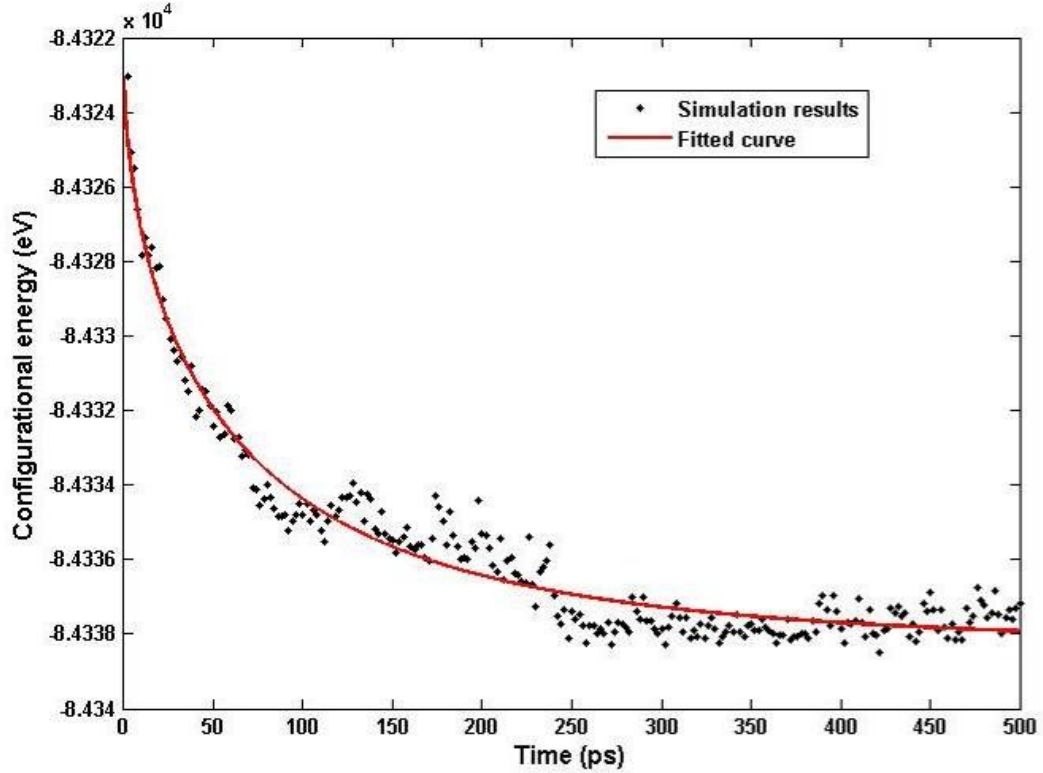


Figure 17. Configurational energies during the initial NPT equilibration of sample 1. Other samples behaved in the same way. Note that these energies were obtained from the relaxed snapshot structures, so the effect of thermal vibrations has been removed.

Figure 17 shows the decrease in configurational energy during the initial equilibration. A relaxation process could be clearly identified, and could be fit to the Kohlrausch-Williams-Watts stretched exponential equation:

$$E = E_0 \exp \left[\left(-\frac{t}{\tau} \right)^\beta \right] + E_{equal} \quad (8)$$

where E_{equal} is the equilibrium energy, E_0 is the energy difference between the initial state and the equilibrium, τ is the relaxation time constant, and β ($0 < \beta < 1$) is the stretching parameter characterizing the non-Debye nature of the relaxation. In this case, the fit gave β as 0.63, and τ as 61 ps. By examining the structural snapshots, it was found that the relaxation was achieved by rearrangement of oxygen ions through migration of the oxygen vacancies. No cation diffusion was observed, because of the relatively low

simulation temperature. The cation neighbors of each oxygen vacancy in the initial and final structures in this stage were examined. The percentage of vacancies without any Gd^{3+} neighbors was calculated and shown in Table III.

Table III. Percentage of $V_{O^{\cdot\cdot}}$ with No Gd^{3+} Neighbor and Lattice Parameters of the Samples at Different Stages of the Simulation

	Percentage of $V_{O^{\cdot\cdot}}$ with no Gd^{3+} neighbor			Lattice parameter (Å, at 0K and under strain-free condition)	
	Initially	After NPT equilibration	After straining	Before straining	After straining
Sample 1	48%	51%	39%	5.4309	5.4303
Sample 2	39%	48%	40%	5.4306	5.4297
Sample 3	41%	51%	37%	5.4306	5.4302

* Lattice parameters are obtained under strain-free condition. Each lattice parameter was obtained by averaging 50 structural snapshots.

It can be seen from Table III that, no matter what the initial value was in the randomly generated structure, the percentage of $V_{O^{\cdot\cdot}}$ without Gd^{3+} neighbors stabilized at about 50% after the NPT equilibration.

In a randomly generated 20% GDC structure, the percentage of oxygen lattice positions without any Gd^{3+} in their nearest neighbor positions should be around $(80\%)^4 \approx 41\%$. This is lower than the percentage found in each of the three structures after equilibration. The equilibrated structures had more vacancies without Gd^{3+} neighbors, which indicated that the nearest neighbor positions of dopants were less preferred by the vacancies. This agreed with the earlier results that the NN type association is less energetically favorable in GDC.

After the NPT ensembles were equilibrated, a 5% hydrostatic compressive strain was then applied onto the samples. This was done by decreasing the lattice parameter and scaling the atom coordinates correspondingly. The compressed structure was simulated with a NVT ensemble for 500 ps. Snapshot structures were also taken every 2 ps to monitor the evolution of the structure.

Following the straining, a relaxation process was observed, as shown in the insert in Figure 18. This was again seen to be achieved through rearrangement of oxygen vacancies. No cation diffusion was observed. As a result of the relaxation under compressive strain, the number of vacancies in NNN configurations decreased from around 50% to 37~40%, as indicated in Table III. This percentage remained stable after this relaxation stage, with fluctuations below 3.5% throughout the time range of the simulations.

An effect of the decrease in the number of NNN vacancies was the shrinking of the strain-free material volume. This contraction was inelastic and consequently decreased the elastic energy of the compressed structure. 50 snapshots of each sample were taken at the end of the relaxation under strain and relaxed them under strain-free conditions. Their lattice parameters, together with these obtained before straining, are listed in Table III. Comparing to the lattice parameters of the samples before straining, the average lattice parameter was shrunk by 0.012%. It is worth noting that the standard deviation of all the sampled lattice parameters was only 0.00042% at 800K. The contraction was considerably larger than the fluctuation in the lattice parameter.

From the above results, it can be seen that the defect structure of GDC could be effectively modulated by mechanical strain/stress. The material responded to a compressive strain by rearranging the defects to a defect structure with more NN-type configurations that were associated with smaller material volume. Such inelastic deformations, caused by changes in the defect structure under mechanical strain/stress, could be the source of the nonlinear mechanical behavior observed in GDC. In the example of the “chemical stress/strain” phenomenon observed by Kossoy et al.,³ a compressive strain was imposed onto the GDC film as a result of the thermal expansion mismatch with the substrate caused by rapid heating. Annealing the compressed film caused an inelastic contraction estimated to be around 0.038%. Apparent similarities exist between this phenomenon and the MD simulations, although the contractions obtained in the simulations were smaller. This could be due to further relaxations beyond the time range of the simulations. Also, some level of clustering might exist in the real GDC material so it might not be fully represented by structures with random dopant positions. Although further extending the simulation time was not practical due to constraints on

computational resources, the activation energy of the relaxation process could be calculated and compared with experiments. This was done by simulating the relaxation of sample 1 under strain at different temperatures (600K, 700K, 800K, 900K), and calculating the time constants by fitting to Equation (8). During each simulation, snapshots of the structure were taken every 2 ps and were subsequently relaxed under a 5% hydrostatic compressive strain. Since the structural relaxation removed thermal vibrations, which implied a temperature of 0K, this -5% strain was calculated with the lattice parameter of the GDC samples at 0K (5.4307 Å). The time constants obtained for different temperatures were then fitted to the following equation:

$$\tau = \tau_0 \exp\left(\frac{E_a}{k_B T}\right) \quad (9)$$

Where E_a is the activation energy, and k_B is the Boltzmann constant. The fitting result is the Arrhenius plot in Figure 18. The activation energy was calculated to be 0.82eV, which is similar to the value estimated from the chemical strain/stress experiments, 1.1eV.⁵

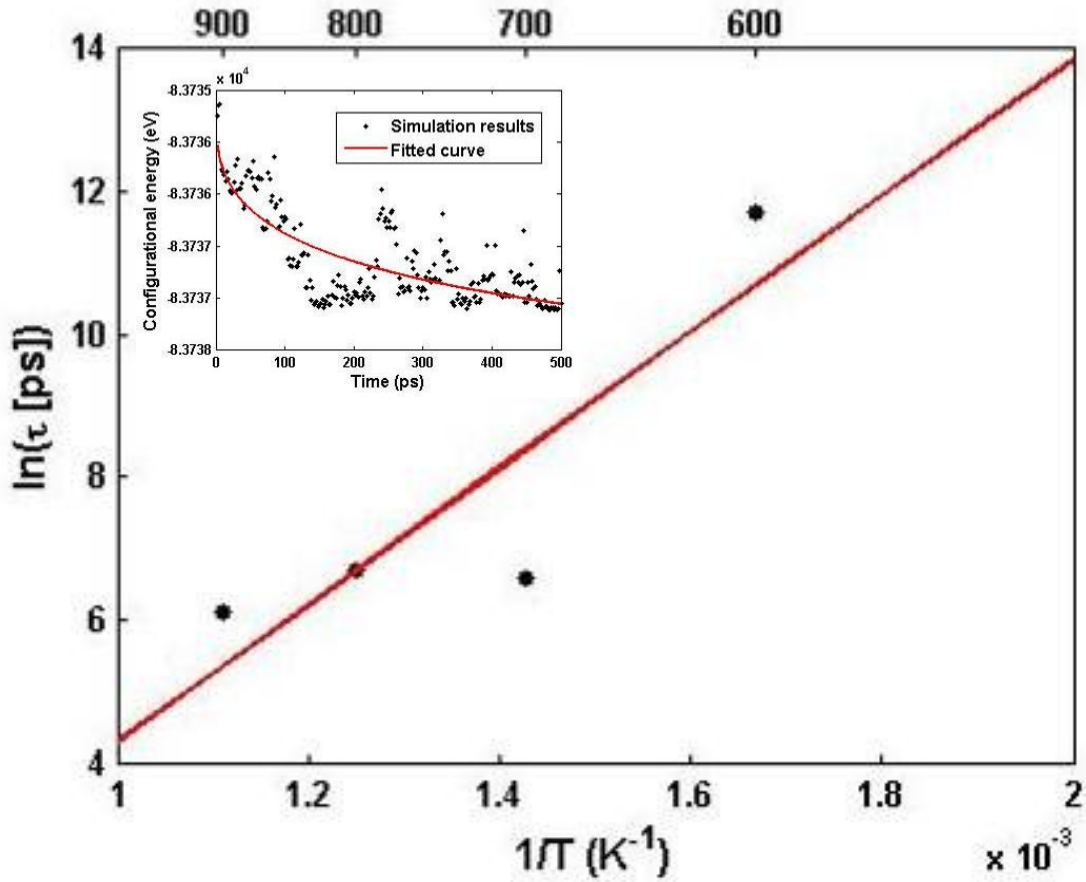


Figure 18. Arrhenius plot of the relaxation time constant versus inverse temperature.

The above results suggest that the short-range rearrangement of oxygen vacancies in GDC could be an explanation of the “chemical stress/strain” phenomenon. Other mechanisms that may warrant future investigations include the effect of strain on the reduction of Ce^{4+} to Ce^{3+} . Since the reduction is associated with a lattice expansion, strains may have an effect on the amount of Ce^{3+} in GDC at a given oxygen partial pressure. Compressive strain may cause some Ce^{3+} to be oxidized back to Ce^{4+} , or vice versa. Notwithstanding, the rearrangement of defect structure clearly plays an important role in the mechanical behavior of GDC.

Although it was shown that the strain/stress modulation of defect structure could be achieved solely through oxygen diffusion, dopant segregations under strain/stress in GDC through cation diffusion would be an interesting topic for future studies. It is expected that cation diffusion would further facilitate the modulation processes. Cation

diffusion permits defects to grow into large clusters and nano-domains. As noted earlier, nano-domains prefer a C-type rare earth structure. Viewed as a derivative of the fluorite structure, the C-type rare earth structure has a lattice parameter (10.804Å from the perfect lattice simulation) 0.15% smaller than ceria, or 0.53% smaller than strain-free GDC. Forming these large domains would further reduce the lattice volume, and therefore be preferential under compressive strains. As a result, in applications where the temperature is high and cation diffusion is effective, such as in solid oxide fuel cell electrolytes at the operating temperature, compressive strains would likely promote defect cluster growth and domain formation. This will in turn lead to conductivity degradation during the operation. On the other hand, under zero or moderate tensile strain, defects would prefer to associate in NNN configurations that are difficult to grow into nano-domains because of the instability of associated pyrochlore structure. Therefore, tensile strain/stress, whether caused by mechanical force (such as carefully selecting electrode materials) or chemical stress (such as introducing larger dopants), may be utilized to improve the performance and reliability of the GDC electrolyte.

C. Conclusions

The effect of strain/stress on the defect structures in GDC has been investigated with atomistic simulations in this chapter. It was found that all the basic defect association types led to volume expansion, and that the volume expansion was greater when the dopant and vacancy were further apart and less associated. Under strain free conditions, the NNN defect pair was the most stable. However, the NN pair became favorable when the compressive strain increased above 0.786%, due to the associated smaller volume expansion.

Molecular dynamics simulations showed that the defect structure could be effectively modulated by the strain condition. When a compressive strain was applied to the GDC structure, the defect structure underwent a relaxation process, during which oxygen vacancies moved into Gd^{3+} neighboring sites. This resulted in an inelastic volume contraction, which did not fully disappear even after the strain was removed.

Based on the simulation results, the “chemical strain/stress” phenomenon in GDC was explained in term of strain modulation of defect structure. The activation energy for

the modulation process calculated from the MD simulations was found to be similar to the experimental value. Furthermore, it was proposed that zero or moderate tensile strain would help prevent nano-domain formation at high temperature, and therefore would be beneficial to the performance and reliability of GDC as a SOFC electrolyte.

References

1. B. C. H. Steele and A. Heinzl, "Materials for Fuel-Cell Technologies," *Nature*, **414** [6861] 345-52 (2001).
2. I. Lubomirsky, "Mechanical Properties and Defect Chemistry," *Solid State Ionics*, **177** [19-25] 1639-42 (2006).
3. A. Kossoy, Y. Feldman, E. Wachtel, I. Lubomirsky, and J. Maier, "Elasticity of Solids with a Large Concentration of Point Defects II. The Chemical Strain Effect in $\text{Ce}_{0.8}\text{Gd}_{0.2}\text{O}_{1.9}$," *Adv. Funct. Mater.*, **17** [14] 2393-8 (2007).
4. I. Lubomirsky, "Practical Applications of the Chemical Strain Effect in Ionic and Mixed Conductors," *Monatshefte für Chemie / Chemical Monthly*, **140** [9] 1025-30 (2009).
5. A. Kossoy, Y. Feldman, R. Korobko, E. Wachtel, I. Lubomirsky, and J. Maier, "Influence of Point-Defect Reaction Kinetics on the Lattice Parameter of $\text{Ce}_{0.8}\text{Gd}_{0.2}\text{O}_{1.9}$," *Adv. Funct. Mater.*, **19** [4] 634-41 (2009).
6. A. Kossoy, A. I. Frenkel, Q. Wang, E. Wachtel, and I. Lubomirsky, "Local Structure and Strain-Induced Distortion in $\text{Ce}_{0.8}\text{Gd}_{0.2}\text{O}_{1.9}$," *Adv. Mater.*, **22** [14] 1659-62 (2010).
7. L. Minervini, M. O. Zacate, and R. W. Grimes, "Defect Cluster Formation in M_2O_3 -Doped CeO_2 ," *Solid State Ionics*, **116** [3-4] 339-49 (1999).
8. B. Wang, R. J. Lewis, and A. N. Cormack, "Computer Simulations of Large-Scale Defect Clustering and Nanodomain Structure in Gadolinia-Doped Ceria," *Acta Mater.*, **59** [5] 2035-45 (2011).
9. W. Smith, "Guest Editorial: DL_POLY—Applications to Molecular Simulation II," *Molecular Simulation*, **32** [12-13] 933- (2006).

CHAPTER 6. STRUCTURES IN SCANDIA-ZIRCONIA PHASE SYSTEM

Our studies of nano-domains in GDC indicated that they served as precursors of phase separation and that their structures were closely related to the structures in the phase equilibria system. Understanding the phase structures is therefore critical in predicting the defect and domain structures in similar materials, such as the material of interest in this chapter, scandia doped zirconia (SDZ).

The SDZ phase system shares similarities with GDC. The structures of zirconia are distorted fluorites, closely related to the fluorite structure of ceria. Scandia exists in C-type rare earth structure under normal conditions, similar to gadolinia. However, the scandia-zirconia system is more complex. As introduced in Chapter 1C2, three rhombohedral phases, δ ($\text{Sc}_4\text{Zr}_3\text{O}_{12}$), γ ($\text{Sc}_2\text{Zr}_5\text{O}_{13}$) and β ($\text{Sc}_{12}\text{Zr}_{50}\text{O}_{118}$), exist in the system, whose structures, especially their cation orderings, are not yet completely clear. But at the same time, domain formation with these structures has been suggested to be the cause of conductivity degradation of SDZ.¹ Further adding to the difficulties, classical empirical pair potentials in the literature have not been able to reproduce all the three structures (cubic, tetragonal, monoclinic phases) of zirconia in the scandia-zirconia system, leading to the question of whether they can adequately simulate different cation orderings in these rhombohedral phases and thus distinguish their subtle energetic differences.

To address these problems, ab-initio simulations with density functional theory (DFT) were conducted to simulate the structures in the scandia-zirconia phase system. Cation ordering in the three rhombohedral phases was modeled and the results are discussed in this chapter. Energetically preferred cation arrangements around vacancies in these structures would provide insight into the defect structures in SDZ and are analyzed in this chapter as well. The ability to predict the energy ordering of these phases using classic potential models in the literature was also examined to help selecting appropriate simulation methods in further studies on the subject.

A. Structures of zirconia and scandia

Details of the simulated structures of cubic, tetragonal, monoclinic zirconia and C-type scandia are listed in Table IV. The structural relaxations were performed with a single unit cell and periodical boundary conditions, using the SIESTA code. Details of the method and other simulation settings are reported in Chapter 2B.

Table IV. Simulated Structures, as well as the Cohesive Energies, of Zirconia and Scandia, Compared with the Experimental Data

		Simulated	Experiment
Cubic ZrO ₂	a (Å)	5.161	5.080 ²
	E_{coh} (eV)	-27.00	
Tetragonal ZrO ₂	a (Å)	3.646	3.605 ²
	c/a	1.445	1.437 ²
	E_{coh} (eV)	-27.05	
Monoclinic ZrO ₂	a (Å)	5.194	5.150 ²
	b/a	1.025	1.012 ²
	c/a	1.028	1.032 ²
	E_{coh} (eV)	-27.13	
C-type Sc ₂ O ₃	a (Å)	9.847	9.905 ³
	E_{coh} (eV)	-21.54	

Overall, the simulated lattice parameters of these structures agreed reasonably well with the experimental data. There was a universal overestimation in the lattice parameters, which was due to the underestimation of bonding by the GGA exchange-correlation functional as had been reported for zirconia and other oxide systems.^{4,5}

The cohesive energies (or bonding energies) were calculated by comparing the crystal energy with the isolated atoms. The energy ordering of zirconia phases found in the simulation was monoclinic>tetragonal>cubic. This agreed with the experimental observations and previous simulation studies,^{5,6} and allowed us to continue to simulate the more complex rhombohedral phases.

B. δ phase $\text{Sc}_4\text{Zr}_3\text{O}_{12}$

Diffraction studies have determined that the structure of δ phase $\text{Sc}_4\text{Zr}_3\text{O}_{12}$ belongs to space group $R\bar{3}$.⁷ It can be described in a hexagonal unit cell which contains three formula units and has lattice parameters $a = b = 9.37 \text{ \AA}$, $c = 8.71 \text{ \AA}$, $\alpha = \beta = 90^\circ$, $\gamma = 120^\circ$.⁷ The primitive cell has one formula unit and lattice parameters of $a = b = c = 6.14 \text{ \AA}$ and $\alpha = \beta = \gamma = 99.5^\circ$.⁷ The structure is closely related to fluorite. Figure 19 shows its primitive cell restored to the fluorite geometry. Oxygen vacancies are placed along the $[111]$ direction of the δ phase primitive cell, as shown with the beach balls. One cation position has coordination number of 6 and the rest are 7-coordinated. The arrangement of Sc^{3+} and Zr^{4+} on these cation sites, however, has not been experimentally determined.

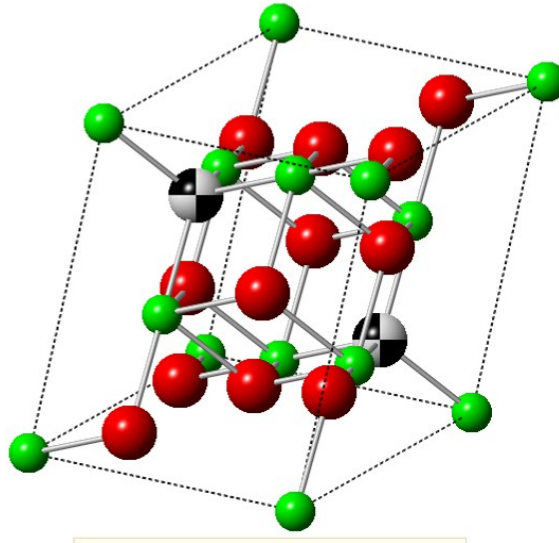


Figure 19. The primitive cell of the δ phase. Cations are shown in green, oxygen in red and vacancies as beach balls.

Since the ion radii of Zr^{4+} (0.84 \AA) and Sc^{3+} (0.87 \AA) are fairly close,⁸ different cation arrangements may have relatively close energies, which may be the cause of the lack of cation ordering information from experiments. However, symmetrically different cation arrangements would lead to different lattice distortion, especially around oxygen vacancies, thus different lattice energies. Theoretically, there has to be a ground state cation arrangement with the lowest lattice energy. Such cation arrangement, especially how Sc^{3+} dopants order relative to the vacancies, could provide insight into the defect structures in SDZ. This has been observed in the studies of nano-domains in GDC

discussed in previous chapters, which showed that large defect clusters and nano-domains were likely to assume the structures of those stable phases in the material system. When viewed as an ordered phase of scandia doped zirconia, the δ phase has a doping concentration of 42.9%. Defect clusters and nano-domains in SDZ with doping concentrations close to this value are most likely to have δ phase related structures. Therefore, the cation ordering in δ phase was studied with computer simulations.

The search for the preferred cation ordering was limited inside the primitive cell. Stable cation arrangements found for the primitive cell can be used as a basis for further studies of ordering in larger structural units. There were a total of 35 combinations to place four Sc^{3+} into the seven cation positions in the primitive cell, but only 7 were symmetrically distinct. In a previous similar study, two of the 7 cation configurations that possess rhombohedral cell vectors were examined.⁹ Since the structure of δ phase belonged to space group $R\bar{3}$ and cations only took two Wyckoff positions with multiplicities of 18 and 3, any cation ordering with Sc:Zr ratio of 4:3 would break the symmetry. Also, because the radii of Sc^{3+} and Zr^{4+} are close, even if the cell vectors were not equal as a result of the cation ordering, the departure from symmetry was expected to be small. As such, preserving rhombohedral cell vectors seemed somewhat arbitrary. Therefore, the simulation was expanded to include all the 7 configurations.

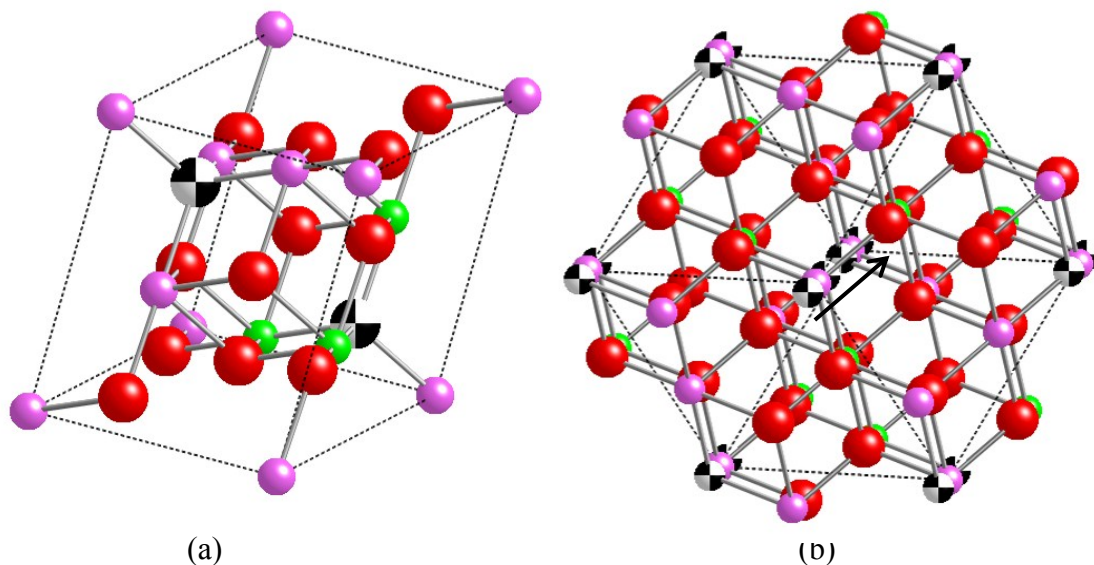


Figure 20. The most stable cation ordering in the δ phase primitive cell, calculated with the SIESTA code. The structure has been restored to fluorite geometry for a clearer view. Zr^{4+} are shown in green, Sc^{3+} in purple, oxygens in red and oxygen vacancies as beach balls. The alignment of cations and vacancies along $[111]$ is shown (b). The black arrow shows $[111]$ direction.

The most stable configuration of the primitive cell, restored to the fluorite geometry, is shown in Figure 20. One of the vacancies is coordinated with four Sc^{3+} , and the other with three Zr^{4+} and one Sc^{3+} . The only cation position with coordination number of 6 is occupied by Sc^{3+} . This configuration was shown to be the most stable in previous studies,^{9,10} and it indeed has rhombohedral cell vectors. The characteristics of this configuration can be viewed more clearly from the $[111]$ direction, as shown in Figure 20 (b). In the middle of Figure 20 (b), a line consisting of only oxygen vacancies and Sc^{3+} can be seen along $[111]$. Such lines are distributed in a hexagonal pattern through the lattice. It should be noted that the $[111]$ of δ phase primitive cell aligns with the $[111]$ of the corresponding fluorite structure. This arrangement also exists in C-type Sc_2O_3 , except that the separation between lines is larger. In the δ phase, the separation is 2.16 times the fluorite unit cell vector, and in C-type, it is 3.27. Based on the studies of nano-domains of GDC, large defect clusters and nano-domains in SDZ, where the local doping concentration exceeds 42.9% (the doping concentration in the δ phase when viewed as SDZ), would most likely to have δ phase or C-type related structures, as these two phases are the most stable phases at these Sc^{3+} concentrations. As a result, vacancies and Sc^{3+}

dopants connected along the [111] direction of fluorite are expected to be a characteristic of the defect structure in heavily doped regions of SDZ.

The formation energies of the most stable configuration calculated with respect to C-type scandia plus cubic, tetragonal and monoclinic zirconia were -0.36 eV, +0.16 eV and +0.80 eV, respectively. This suggested that the most stable δ phase configuration calculated with GGA DFT method was stable compared with the phase separation of C-type scandia and cubic zirconia, but becomes unstable when tetragonal or monoclinic zirconia was considered. This problem has been reported in previous DFT studies, and was believed to be caused by inadequate representations of the monoclinic and tetragonal phases by the method.^{9,11} It was suspected that an improvement of the DFT method, especially in the exchange-correlation functional, such as using hybrid exchange-correlation functionals, might be needed to fully depict the energy landscape of SDZ.

There have been several studies in the literature utilizing classical empirical potentials to simulate the defect association and transport phenomena in SDZ¹²⁻¹⁸ and to search for the possible δ phase configurations with combined energy minimization - Monte Carlo method.¹⁰ Two sets of potentials, developed in Ref. 19 (P1) and Ref. 18 (P2) and their references, respectively, were predominately used in these studies. Both potential sets used Buckingham pair potentials and shell models, details of which are listed in Table V and Table VI. Classical simulations with these potentials require significantly less computational effort, and therefore would be preferred if the potential models could adequately reproduce the properties and structures of interest. For the purpose of simulating large defect clusters and nano-domains in SDZ, it is required that the potential set to correctly calculate the energy ordering of the cation arrangements, especially with respect to the arrangement of oxygen vacancies, in the rhombohedral phases. Therefore, the 7 δ phase configurations were relaxed with the two potential sets and the calculated energy orderings were compared with that calculated from DFT simulations. Some studies in the literature also used the P1 potential set without the shell model.^{13,16} Strictly speaking, the short-range potentials developed with shell models are not intended to be used directly without the corresponding shells. However, they were still included in this test as potential set P1' for validation purposes.

Table V. Short-Range Potential Parameters for SDZ

	Interaction	A (eV)	ρ (Å)	C (eVÅ ⁶)	Reference
P1 (P1')	Zr ⁴⁺ -O ²⁻	985.869	0.376	0.0	[19]
	Sc ³⁺ -O ²⁻	1299.4	0.3312	0.0	[20]
	O ²⁻ -O ²⁻	22764.0	0.149	27.879	[20]
P2	Zr ⁴⁺ -O ²⁻	1502.11	0.3477	5.1	[12]
	Sc ³⁺ -O ²⁻	1575.85	0.3211	0.0	[21]
	O ²⁻ -O ²⁻	9547.96	0.2192	32.0	[22]

Table VI. Shell Model Parameters For SDZ

	Interaction	Shell charge (e)	K (eVÅ ⁻²)	Reference
P1	Zr ⁴⁺	1.35	169.617	[19]
	O ²⁻	-2.86902	74.92	[20]
P2	Zr ⁴⁺	-0.05	189.7	[12]
	O ²⁻	-2.04	6.3	[22]

In Figure 21, the energies of the 7 configurations calculated with the classical approach are plotted against the energies obtained from the ab-initio approach. Each data point represents one configuration. For each data point, its y coordinate is the energy calculated with the empirical potential set, subtracted by the energy of the most stable configuration calculated with the same potential set. Its x coordinate was calculated in the same way but with the DFT method. Ideally, the line connecting all the data points should be monotonic with positive derivatives, meaning that changing the simulation method does not change the energy ordering of these structures. At least, it would be expected that the most stable configuration determined with each method to be the same, as well as the most unstable one. However, as seen from Figure 21, none of this was true: different configurations were predicted to be the most stable and unstable structures by different methods or potential sets. The overall trend between classical methods and DFT

was reversed – stable configurations from classical simulations became unstable in DFT, and vice versa. The most stable configurations predicted by the classical methods were less symmetrical than the ones by DFT, and were not reported as possible δ phase configurations in previous studies. Additionally, P1' not surprisingly gave different configurations from P1 for both the ground state and the most unstable structure. Since there is no justification whatsoever to use the potential set without its shell models and it failed to produce the same result with the full potential set, P1' was excluded in the following simulations and discussions.

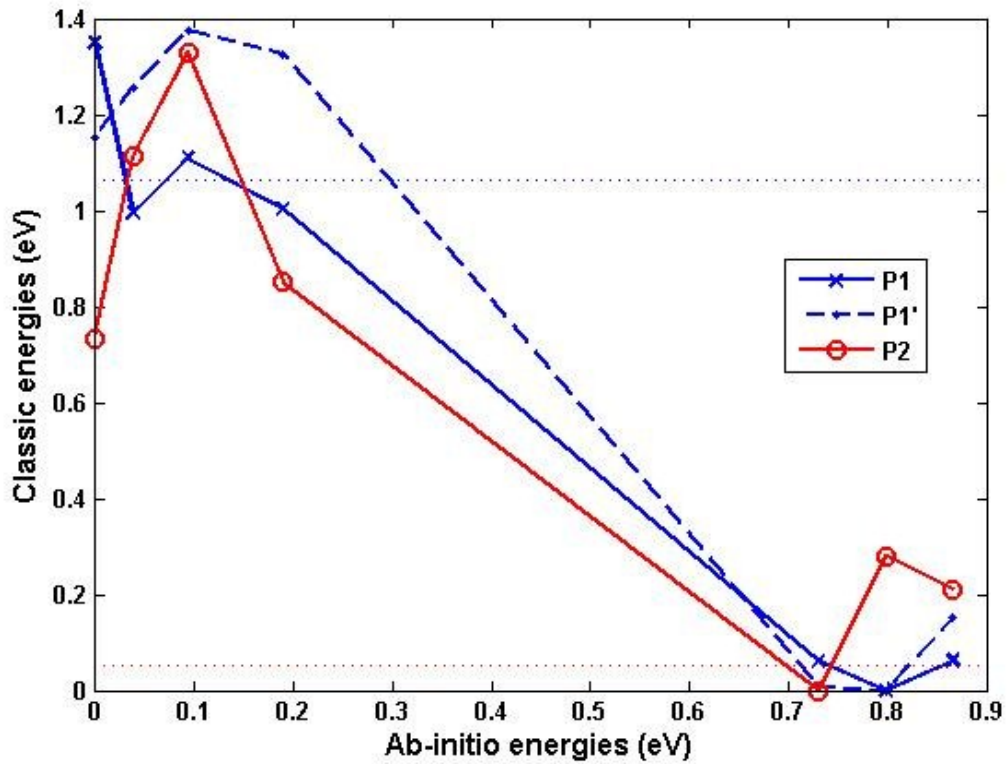


Figure 21. Energies of the 7 δ phase configurations calculated with the classical approach compared with the DFT approach.

The formation energies of the most stable δ phase configuration compared to the phase separation of cubic zirconia and C-type scandia were -1.06 eV for P1 and -0.05eV for P2, and they are plotted as the dashed lines in Figure 21. Only those configurations below the formation energy line, 4 configurations for P1 and only 1 for P2, were stable. DFT calculations also gave 4 stable configurations, the 4 configurations on the left of $x=0.36$ eV. In this regard, the P2 potential set seemed to underestimate the stability of δ

phase. The P2 potential set, unlike P1 and the DFT method, was unable to simulate tetragonal zirconia, and might be less versatile in simulating structures heavily distorted from the cubic fluorite structure. Nonetheless, based on the results of the P1 potential set and DFT calculations, it could be concluded that the lack of a clear cation ordering seen in experimental observations might be due to the coexistence of multiple cation orderings.

It is worth noting that, even though the P1 potential set was unable to simulate monoclinic zirconia, it did reproduce the tetragonal phase and predicted a -0.62 eV formation energy for the δ phase, compared with the tetragonal zirconia and C-type scandia, which the DFT method failed to identify. These facts suggested that, quality-wise, neither the classical models nor the DFT method were completely accurate (but nor were they completely worthless). Caution should be taken when simulating structures with subtle energy differences in the SDZ system. Furthermore, a detailed study of the methods with experimental validation is urgently needed to identify the pitfalls and promises of each method. In the meantime, both the classical method and DFT are used and compared in this chapter.

C. γ phase ($\text{Sc}_2\text{Zr}_5\text{O}_{13}$)

The structure of γ phase ($\text{Sc}_2\text{Zr}_5\text{O}_{13}$) also belongs to space group $R\bar{3}$.^{7,23} Its hexagonal unit cell contains six formula units, and has lattice parameters $a = b = 9.53 \text{ \AA}$, $c = 17.44 \text{ \AA}$, $\alpha = \beta = 90^\circ$, $\gamma = 120^\circ$.⁷ The rhombohedral primitive cell has two formula units and lattice parameters of $a = b = c = 8.00 \text{ \AA}$ and $\alpha = \beta = \gamma = 73.0^\circ$.⁷ The primitive cell, restored to the fluorite geometry, is shown in Figure 22. When viewed as SDZ, the γ phase has a doping concentration of 28.6%. Two of the four oxygen positions on the diagonal of the primitive cell are occupied by vacancies. Among the cations in the primitive cell, one cation has a coordination number (CN) of 6, six have a CN of 7 and seven have a CN of 8. The arrangement of Sc^{3+} and Zr^{4+} on these cation sites, like the δ phase, has not been experimentally determined.

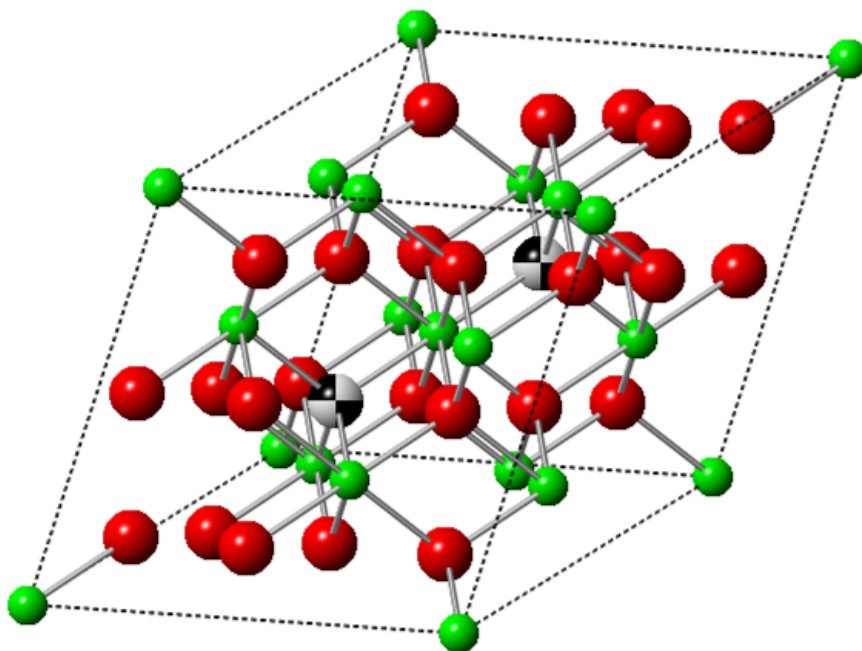


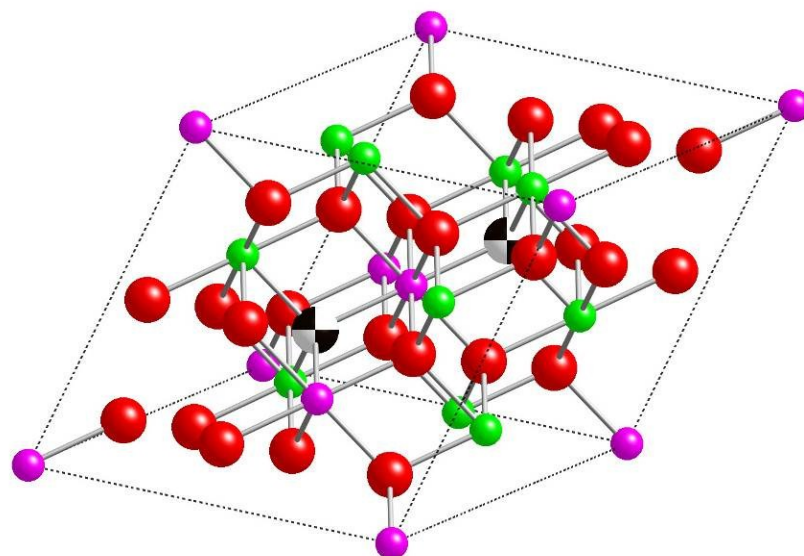
Figure 22. The primitive cell of the γ phase. Cations are shown in green, oxygen in red and vacancies as beach balls.

For the cation ordering in the γ phase, Sc^{3+} occupying four of the fourteen cation positions in the primitive cell gave a total number of 1001 configurations. More than a hundred of these configurations were symmetrically inequivalent. Since the DFT simulations were computationally demanding, a fast initial screening scheme utilizing the classical method was constructed. The scheme was based on the observation that the P2 potential set seemed able to adequately differentiate between configurations. In the previous section, discrepancies were shown between the classical and DFT simulation results. The correlation between the energies calculated with classical potentials and DFT was not straightforward, if not non-existent. However, in Figure 21, almost all of the absolute values of the derivatives were larger than one along the line of the P2 potential set, which means that the classical potentials resulted in larger energy differences between the configurations than the DFT results. In another word, if two configurations had similar energies in the classical simulation with the P2 potential set, their lattice energies calculated by the DFT method should be even closer. This property of the P2 potential set enabled the grouping of the configurations with similar energies, and in turn

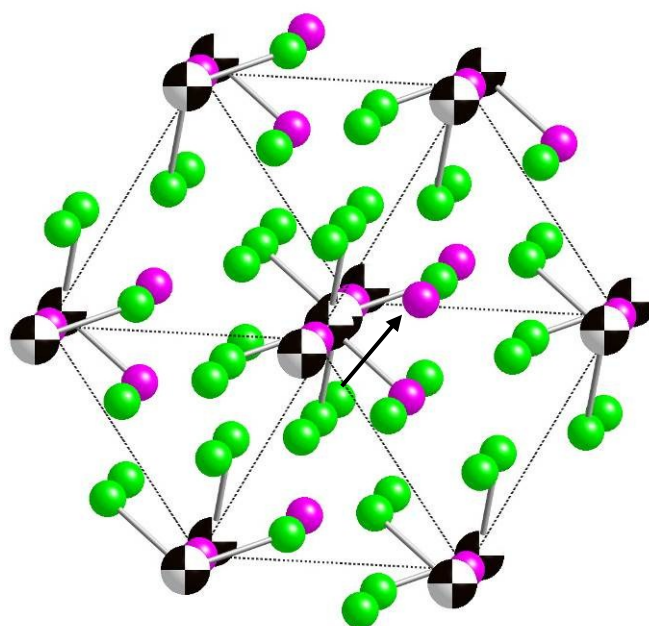
an adequate sampling all the configurations, based on classic simulation results. The details of the screening scheme are as follows.

Using the classical approach with the P2 potential set, all 1001 configurations for the initial screening were relaxed within hours. The screening then started with sorting the energies of the relaxed structures. Beginning with the lowest energy configuration, a configuration was selected if its energy was at least 0.01 eV different from the previously selected one. Because the energies of symmetrical equivalent structures were identical in the simulations (with numerical noises below 1×10^{-5} eV in classical simulations), this screening process effectively removed the structural degenerates from all the configurations. Additionally, a configuration was skipped if its energy did not differ from already selected configurations, which reduced the computational effort while adequately sampling the entire possible configurations. 41 configurations were selected by this way for DFT relaxations.

The most stable structure of the 41 configurations in the DFT simulations is shown in Figure 23. In the primitive cell, one oxygen vacancy is coordinated with two Sc^{3+} and two Zr^{4+} , the other with one Sc^{3+} and three Zr^{4+} . The only cation position with a CN of 6 coordination number is occupied by Sc^{3+} , similar to the δ phase. The rest of Sc^{3+} in the primitive cell occupy two cation positions with CN of 8 and one with CN of 7. Some structural similarities between the δ and γ phases can be seen from Figure 23 (b). The oxygen vacancies align in lines parallel to the [111] direction and the lines form a hexagonal pattern. In the δ phase, all the oxygen sites on the line were vacancies and all the cations are Sc^{3+} . In the γ phase, all the cations on the line are Sc^{3+} , but only half of the oxygen sites are vacant. The defect clusters in SDZ with medium doping concentrations (28.6% ~ 42.9%) are expected to prefer such structures, involving vacancy-dopant-vacancy associations aligning along the fluorite [111] direction.



(a)



(b)

Figure 23. The most stable cation ordering in the γ phase primitive cell, calculated with the SIESTA code. The structure has been restored to fluorite geometry for a clearer view. Zr^{4+} are shown in green, Sc^{3+} in purple, oxygens in red and oxygen vacancies as beach balls. The alignment of cations and vacancies along $[111]$ is shown (b) with the oxygens omitted. The black arrow shows $[111]$ direction.

In Figure 24, the energies of the 41 configurations are plotted in the same fashion of Figure 21. It can be seen that the correlation between the results of classical and DFT

methods became even more irregular. However, the range of the energies resulting from each method was much smaller than that of the δ phase. This might suggest a higher likelihood of disordering in the γ phase.

The formation energy of the most stable γ phase configuration with respect to cubic zirconia and C-type scandia was -1.62 eV for P1, +0.08 eV for P2 and -0.01 eV for DFT. All the 41 configurations were stable in the simulations of P1. None was stable in the simulations using P2 and only one was stable in DFT simulations. Considering the evidence of the γ phase and the lack of cation ordering in experimental observations,⁷ it is likely that both P2 and DFT underestimated the stability of the γ phase. The P1 potential set also predicted a formation energy of -0.15 eV with respect to tetragonal zirconia, which added to the credibility of the potential set. Based on the results with the P1 potential set, the γ phase might be more prone to heavy disordering, compared to the δ phase. A wide range of cation configurations might be presented in the γ phase which could appear to be almost a random distribution. But at the same time, both classical simulations with P1 and P2 and DFT calculations predicted that the cation site between the two vacancies in the primitive cell was occupied by Sc^{3+} . As discussed earlier, this could be a characteristic of the defect clusters in SDZ with medium doping concentrations.

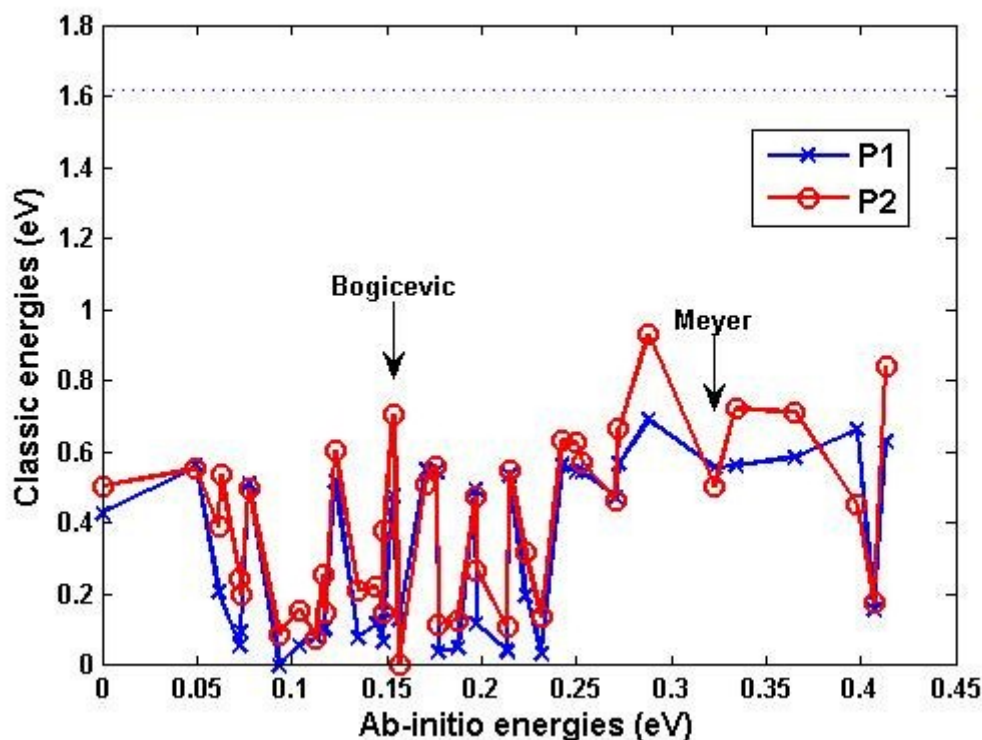


Figure 24. Energies of the 41 γ phase configurations calculated with the classical approach compared with the DFT approach.

Two previous studies have simulated the cation ordering in the γ phase but different ground states were reported. In the study by Bogicevic and Wolverton^{9, 4} symmetrically inequivalent cation orderings were considered. In their ground state configuration, both vacancies had three Zr^{4+} and one Sc^{3+} . The cation between the two vacancies was found to be Zr^{4+} . In the other study,²³ Meyer et al. performed unit cell relaxations with fixed angle and forced equality of cell vectors a and b . They found that one vacancy had three Sc^{3+} and one Zr^{4+} neighbor cations and the other had one Sc^{3+} and three Zr^{4+} . One of the Sc^{3+} was shared by the two vacancies, resulting in the only six coordinated cation in the primitive cell. In an effort to resolve this discrepancy, the two ground state configurations reported in these two studies were included along with the 41 configurations selected for the DFT relaxations, and they have been marked in Figure 24. The two structures were found to be among those with relatively high structural energies (less stable) in both the classical and DFT methods. However, the ordering reported by Meyer et al. had the cation site between the two vacancies in the primitive cell occupied

by Sc^{3+} ,²³ which occurred in the ground state configurations of P1, P2 and DFT simulations in this study.

D. β phase $\text{Sc}_{12}\text{Zr}_{50}\text{O}_{118}$

As with the δ and γ phases, the structure of β phase $\text{Sc}_{12}\text{Zr}_{50}\text{O}_{118}$ belongs to the space group $R\bar{3}$. It can be described in a hexagonal unit cell which contains three formula units and has lattice parameters $a = b = 19.74 \text{ \AA}$, $c = 17.92 \text{ \AA}$, $\alpha = \beta = 90^\circ$, $\gamma = 120^\circ$.⁷ The primitive cell parameters calculated based on the space group are $a = b = c = 12.87 \text{ \AA}$ and $\alpha = \beta = \gamma = 100.2^\circ$. Again, the structure is closely related to fluorite. When viewed as SDZ, the γ phase has a doping concentration of 19.4%. Figure 25(a) shows its primitive cell restored to the fluorite geometry. The oxygen vacancies are arranged in the way shown in Figure 25(b).

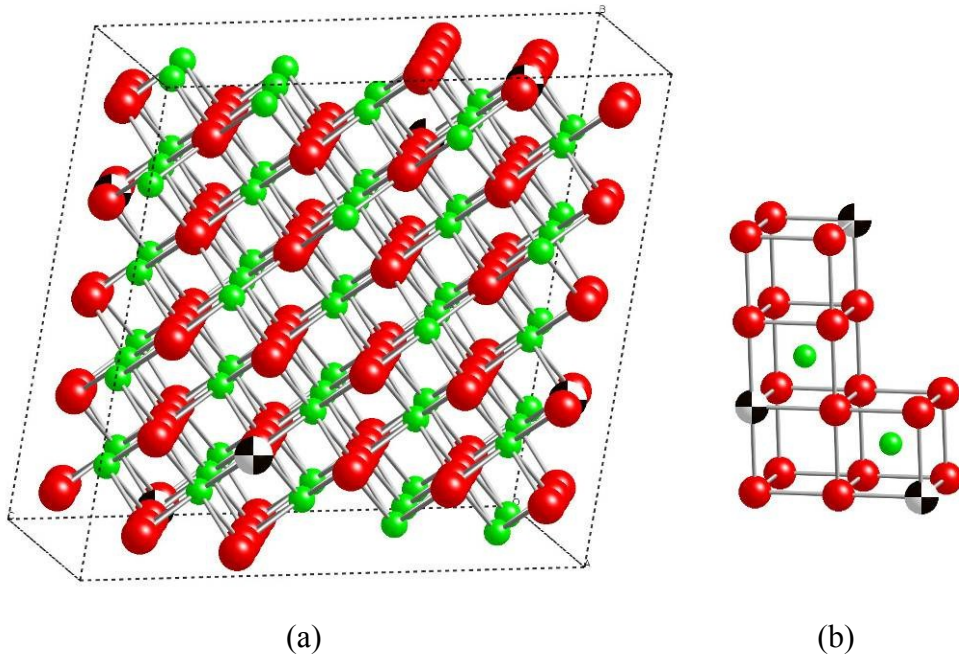


Figure 25. The primitive cell of the β phase is shown in (a), and the characteristic vacancy arrangement is shown in (b). Cations are shown in green, oxygen in red and vacancies as beach balls.

The arrangement of Sc^{3+} and Zr^{4+} on the cation sites of the β phase has not been studied previously. There were 62 cation sites in the primitive cell, which gave an astronomical number (of the order of 10^{11}) of the possible symmetrically inequivalent cation orderings. It became impossible to examine all these configurations, even with the

classical method. However, unlike the δ and γ phases, there were 45 cation configurations that could preserve all the symmetry elements of the $R\bar{3}$ space group. These configurations were constructed by placing Sc^{3+} on two of the ten 6f Wyckoff positions in the primitive cell. They had the highest symmetry among all the possible cation orderings, and, according to experiences of simulating similar material systems, such structures were more likely to yield low lattice energies. The stable structures with high symmetry also could serve as the basis for further investigations of structures with lower symmetry. Therefore, these 45 arrangements were selected for structural relaxations.

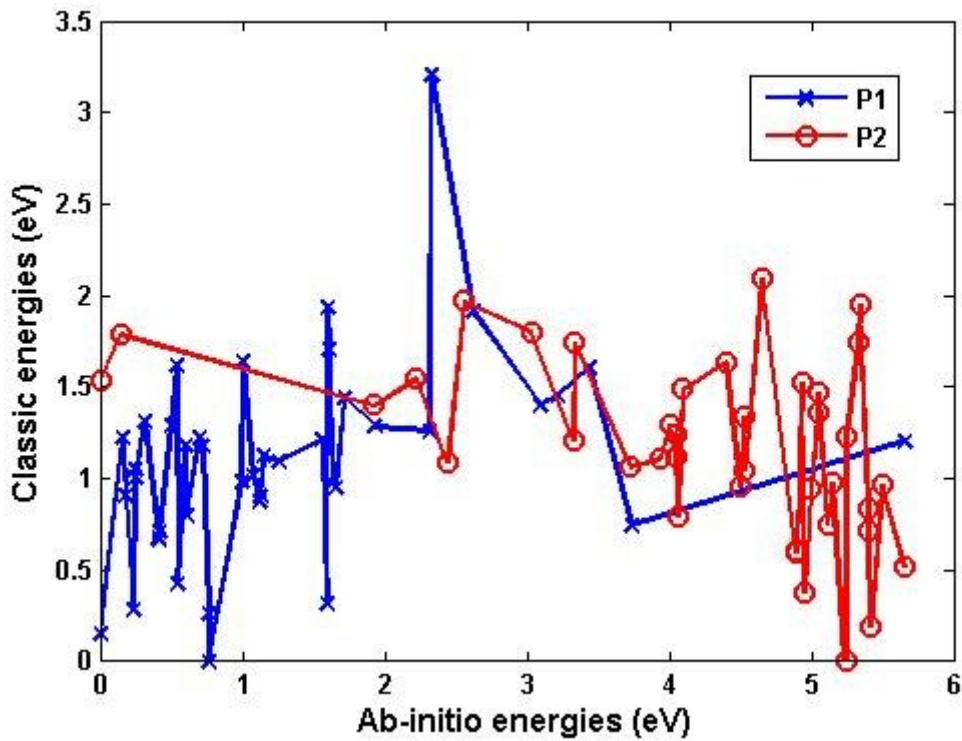


Figure 26. Energies of the 45 β phase configurations calculated with the classical approach compared with the DFT approach.

In Figure 26, the energies of the 45 configurations are plotted in the same fashion of Figure 24 in the last section. 28 of these configurations in the DFT calculations, represented by the data points on the left of $x=1.30$ eV in Figure 26, were found to be stable compared to the phase separation of cubic zirconia and C-type scandia. Some of these configurations were also among the most stable ones found with the P1 potential

set, suggesting an improvement in the correspondence between the two methods even though P1 potential set predicted all the 45 configurations to be stable compared with cubic zirconia and C-type scandia. The P2 potential set, on the other hand, predicted none of the configurations to be stable and showed an overall trend opposite to both P1 potential set and DFT calculations.

None of the methods tested here was able to predict a stable β phase structure with respect to the phase separation of monoclinic zirconia and C-type scandia. However, in term of predicting stability of the β phase and better agreement with DFT calculations, the P1 potential set seemed to be more robust compared with P2, and therefore might be a better choice for classical simulations of the SDZ system.

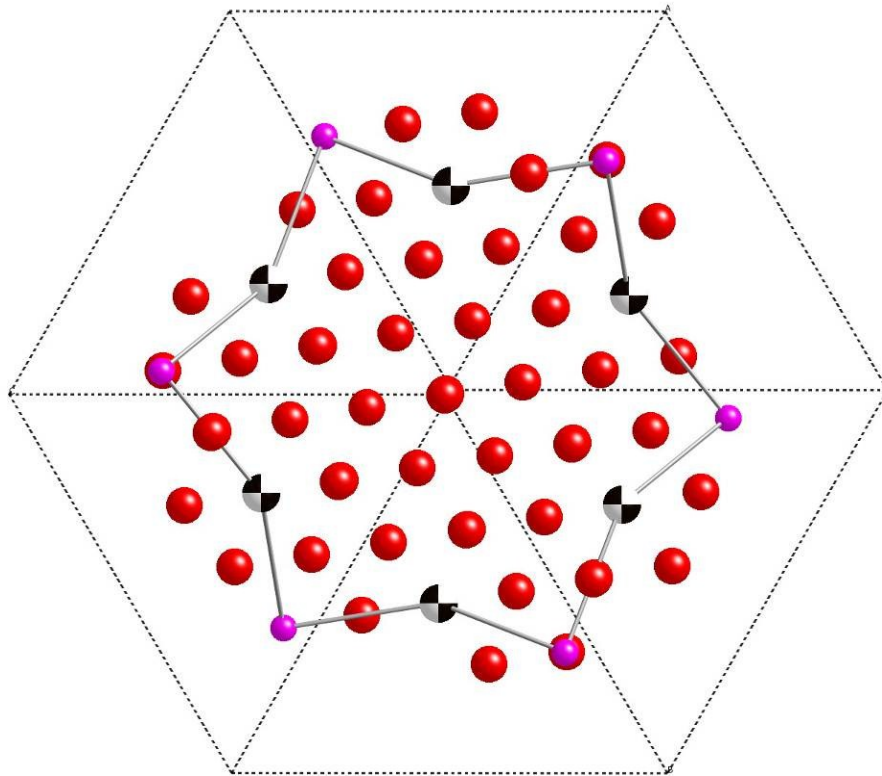


Figure 27. Characteristic dopant-vacancy pattern of the most stable configurations. Sc^{3+} are shown in purple, oxygens in red and oxygen vacancies as beach balls. Zr^{4+} have been omitted.

In the β phase, 4 positions, among the ten 6f Wyckoff positions for cations, had one nearest neighbor (NN) vacancy, 5 positions had no NN vacancy but had one or two vacancies as their next nearest neighbors, and 1 position did not have any NN or NNN vacancies. The configuration became relatively stable when Sc^{3+} were placed on at least one position that has NNN vacancies. A ring-like pattern formed by dopants and vacancies in NNN positions, shown in Figure 27, was found in the five most stable configurations predicted by the P1 potential set. Such patterns could be the preferred structures for defect clusters in SDZ with doping concentrations close to the scandium concentration in the β phase. On the other hand, when Sc^{3+} were placed on two of the four positions that have NN vacancies, the configuration became relatively unstable. The lattice energies of such configurations were 1.3~1.8 eV higher than the most stable configuration with the P1 potential set. However, because multiple stable configurations were identified in the simulations, the β phase would be likely to exhibit a significant level of disordering.

E. Conclusions

In this chapter, the cation ordering in the three rhombohedral phases of SDZ, the δ ($\text{Sc}_4\text{Zr}_3\text{O}_{12}$), γ ($\text{Sc}_2\text{Zr}_5\text{O}_{13}$) and β ($\text{Sc}_{12}\text{Zr}_{50}\text{O}_{118}$) structures were studied. The energetic ordering of the cation arrangements in the primitive cell of each phase was calculated with both DFT and classical simulations. The comparison between the results from the two methods and experimental observations showed that neither method was satisfactory in describing the entire phase system of SDZ. The DFT method was able to simulate the polymorphs of zirconia and give a ground-state cation ordering of the δ phase that has been reported in the literature. But the classic method with the P1 potential set produced the most reasonable results regarding the stabilities of the three phases.

By compiling the results obtained with different methods, the characteristics of the dopant arrangement around the vacancies in the three phases were identified. The δ phase shared similarity with the C-type rare earth structure, where lines of dopants and vacancies were formed along the $[111]$ direction. The γ phase structure had dopant-vacancy-dopant associations formed along the $[111]$ direction and the most stable β phase structures contained a hexagonal pattern formed by dopants and vacancies in NNN

positions. These characteristics were also expected to be the preferred defect arrangements and domain structures in SDZ when the doping concentrations were close to the scandium contents in these phases.

References

1. S. P. S. Badwal and J. Drennan, "Microstructure/Conductivity Relationship in the Scandia-Zirconia System," *Solid State Ionics*, **53-56, Part 2** [0] 769-76 (1992).
2. C. J. Howard, R. J. Hill, and B. E. Reichert, "Structures of ZrO₂ Polymorphs at Room Temperature by High-Resolution Neutron Powder Diffraction," *Acta Crystallogr., Sect. B: Struct. Sci.*, **44** [2] 116-20 (1988).
3. D. Liu, W. Lei, Y. Li, Y. Ma, J. Hao, X. Chen, Y. Jin, D. Liu, S. Yu, Q. Cui, and G. Zou, "High-Pressure Structural Transitions of Sc₂O₃ by X-Ray Diffraction, Raman Spectra, and Ab Initio Calculations," *Inorg. Chem.*, **48** [17] 8251-6 (2009).
4. J. Goniakowski, J. M. Holender, L. N. Kantorovich, M. J. Gillan, and J. A. White, "Influence of Gradient Corrections on the Bulk and Surface Properties of TiO₂ and SnO₂," *Phys. Rev. B*, **53** [3] 957-60 (1996).
5. G. Jomard, T. Petit, A. Pasturel, L. Magaud, G. Kresse, and J. Hafner, "First-Principles Calculations to Describe Zirconia Pseudopolymorphs," *Phys. Rev. B*, **59** [6] 4044 (1999).
6. F. M. Spiridonov, L. N. Popova, and R. Y. Popil'skii, "On the Phase Relations and the Electrical Conductivity in the System ZrO₂-Sc₂O₃," *J. Solid State Chem.*, **2** [3] 430-8 (1970).
7. M. R. Thornber, D. J. M. Bevan, and J. Graham, "Mixed Oxides of the Type MO₂(Fluorite)-M₂O₃. III. Crystal Structures of the Intermediate Phases Zr₅Sc₂O₁₃ and Zr₃Sc₄O₁₂," *Acta Crystallogr., Sect. B: Struct. Sci.*, **24** [9] 1183-90 (1968).
8. R. Shannon, "Revised Effective Ionic Radii and Systematic Studies of Interatomic Distances in Halides and Chalcogenides," *Acta Crystallogr., Sect. A: Found. Crystallogr.*, **32** [5] 751-67 (1976).
9. A. Bogicevic and C. Wolverton, "Nature and Strength of Defect Interactions in Cubic Stabilized Zirconia," *Phys. Rev. B*, **67** [2] 024106 (2003).
10. C. R. Stanek, C. Jiang, B. P. Uberuaga, K. E. Sickafus, A. R. Cleave, and R. W. Grimes, "Predicted Structure and Stability of A₄B₃O₁₂ Δ-Phase Compositions," *Phys. Rev. B*, **80** [17] 174101 (2009).

11. A. Bogicevic, C. Wolverton, G. M. Crosbie, and E. B. Stechel, "Defect Ordering in Aliovalently Doped Cubic Zirconia from First Principles," *Phys. Rev. B*, **64** [1] 014106 (2001).
12. G. Busker, A. Chreneos, R. W. Grimes, and I. W. Chen, "Solution Mechanisms for Dopant Oxides in Yttria," *J. Am. Ceram. Soc.*, **82** [6] 1553-9 (1999).
13. K.-S. Chang and K.-L. Tung, "Oxygen-Ion Transport in a Dual-Phase Scandia–Yttria-Stabilized Zirconia Solid Electrolyte: A Molecular Dynamics Simulation," *ChemPhysChem*, **10** [11] 1887-94 (2009).
14. R. Devanathan, W. J. Weber, and S. C. Singhal, "Atomistic Simulation of Ion Transport in Yttria- and Scandia-Stabilized Zirconia," *ECS Meeting Abstracts*, **502** [27] 1036- (2006).
15. M. Sakib Khan, M. Saiful Islam, and D. R. Bates, "Cation Doping and Oxygen Diffusion in Zirconia: A Combined Atomistic Simulation and Molecular Dynamics Study," *J. Mater. Chem.*, **8** [10] 2299-307 (1998).
16. K.-L. Tung, K.-S. Chang, C.-C. Hsiung, Y.-C. Chiang, and Y.-L. Li, "Molecular Dynamics Simulation of the Complex Dopant Effect on the Super-Ionic Conduction and Microstructure of Zirconia-Based Solid Electrolytes," *Sep. Purif. Technol.*, **73** [1] 13-9 (2010).
17. Z. Q. Yu, R. Devanathan, W. Jiang, P. Nachimuthu, V. Shutthanandan, L. Saraf, C. M. Wang, S. V. N. T. Kuchibhatla, and S. Thevuthasan, "Integrated Experimental and Modeling Study of Ionic Conductivity of Scandia-Stabilized Zirconia Thin Films," *Solid State Ionics*, **181** [8-10] 367-71 (2010).
18. M. O. Zacate, L. Minervini, D. J. Bradfield, R. W. Grimes, and K. E. Sickafus, "Defect Cluster Formation in M_2O_3 -Doped Cubic ZrO_2 ," *Solid State Ionics*, **128** [1-4] 243-54 (2000).
19. A. Dwivedi and A. N. Cormack, "A Computer Simulation Study of the Defect Structure of Calcia-Stabilized Zirconia," *Philos. Mag. A*, **61** [1] 1-22 (1990).
20. G. V. Lewis and C. R. A. Catlow, "Potential Models for Ionic Oxides," *J. Phys. C: Solid State Phys.*, **18** [6] 1149 (1985).
21. L. Minervini, M. O. Zacate, and R. W. Grimes, "Defect Cluster Formation in M_2O_3 -Doped CeO_2 ," *Solid State Ionics*, **116** [3-4] 339-49 (1999).
22. R. W. Grimes, D. J. Binks, and A. B. Lidiard, "The Extent of Zinc Oxide Solution in Zinc Chromate Spinel," *Philos. Mag. A*, **72** [3] 651 - 68 (1995).

23. S. Meyer, E. Schweda, N. J. Martinez Meta, H. Boysen, M. Hoelzel, and T. Bredow, "Neutron Powder Diffraction Study and DFT Calculations on the Structure of $Zr_{10}Sc_4O_{26}$," *Zeitschrift für Kristallographie*, **224** [11] 539-43 (2009).